Abstract

Many systems in nature and the synthetic world involve ordered arrangements of units on two-dimensional surfaces. In this thesis I discuss the fundamental role payed by both the topology of the underlying surface and its detailed curvature. Topology dictates certain broad features of the defect structure of the ground state but curvature-driven energetics controls the detailed structured of ordered phases. Among the surprises are the appearance in the ground state of structures that would normally be thermal excitations and thus prohibited at zero temperature. Examples include excess dislocations in the form of grain boundary scars for spherical crystals above a minimal system size, dislocation unbinding for toroidal hexatics, interstitial fractionalization in spherical crystals and the appearance of well-separated disclinations for toroidal crystals. Much of the analysis leads to universal predictions that do not depend on the details of the microscopic interactions that lead to order in the first place. These predictions are subject to test by the many experimental soft and hard matter systems that lead to curved ordered structures such as colloidal particles self-assembling on droplets of one liquid in a second liquid. The defects themselves may be functionalized to create ligands with directional bonding. Thus nano to meso scale superatoms may be designed with specific valency for use in building supermolecules and novel bulk materials. Parameters such as particle number, geometrical aspect ratios and anisotropy of elastic moduli permit the tuning of the precise architecture of the superatoms and associated supermolecules. Thus the field has tremendous potential from both a fundamental and materials science/supramolecular chemistry viewpoint.

Unordinary Order

A theoretical, computational and experimental investigation of crystalline order in curved space

by

Luca Giomi

Laurea in Fisica, Università degli Studi di Roma *La Sapienza*, 2004

DISSERTATION

Submitted in partial fulfillment of the requirements for the
degree of Doctor of Philosophy in Physics
in the Graduate School of Syracuse University

April 2009

Approved _____

Prof. Mark J. Bowick

Date _____

Committee Approval Page

Contents

To Angelo Giomi: granfather and carpenter.

Chapter 1

Order and geometry in condensed matter

1.1 Introduction

More than 200 years ago, on his treatise on the resistance of fluids d'Alembert wrote: "Geometry, which should only obey physics, when united with it sometimes commands it" [1]. Since then the physics community has explored the power of geometry not only to describe, but also the explain structures and their properties. In the past 20 years soft condensed matter physics has provided many examples of how the geometry of matter is not a quiescent background for some microscopic degrees of freedom, but instead plays a major role in determining structural and mechanical properties and designing the phase diagram of materials such as colloids, liquid crystals, membranes, glasses and carbon nanostructure.

Geometric models of condensed matter systems have been developed for a wide class of materials since the pioneering work of Bernal and Finney [2–6]. In a series of classic papers they suggested that several properties of liquids have their geometrical counterpart in randomly packed arrays of spheres. The difference in density between the solid and the liquid phase of a simple monoatomic substance, for in-

stance, is approximately the same between periodically and randomly packed hard spheres (roughly $15\% - 16\%$). Also the radial distribution function of randomly packed spheres corresponds well with that determined by X-ray and neutron diffraction for rare-gas liquids. After Bernal, a significant amount of work has been done on random close packing and, even though the legitimacy of the notion of random close packing itself has been frequently questioned in recent years [7], it is now established that many features of the liquid state have in fact a purely geometrical nature.

After the discovery of icosahedral order in metallic glasses [8, 9] the idea of *geometrical frustration* (the geometric impossibility of establishing a preferred local order everywhere in space, see Sec. 2), became a fundamental concept for the characterization of amorphous solids. Farges and coworkers [10–12] were the first to show, by electron diffraction experiments and computer simulations, that the first atoms of small aggregates of rare gasses condensed in ultra-high vacum form regular tetrahedra, which later organize in the form of small icosahedral clusters. Since icosahedra don't fill three-dimensional Euclidean space $\mathbb{R}^3$, the structure resulting from the aggregation of these icosahedral building blocks doesn't exhibit long range translational order. The lack of crystallization in covalent glasses is also rooted in the geometrical frustration associated with the constant coordination number of their constituents. Tetravalent monoatomic materials, for instance, cannot form a constant angle between bonds incident at the same atom and organize in a regular network at the same time. In multiatomic glass-forming material the situation is more involved and the route to the formation of amorphous structures is related to the fact that crystallization would require complex activated phenomena and too large a decrease in entropy.

A breakthrough in the geometrical description of amorphous solids came in 1979 when Sadoc and Kléman first observed that a number of continuous random lattices can be classified as specific mappings of ordered lattices in spaces of constant curvature onto $\mathbb{R}^3$ [13]. This idea was inspired by the remark that, whereas regular

tetrahedra don't fill the three-dimensional Euclidean space, they regularly tile the three-dimensional sphere $\mathbb{S}^3$ (the manifold described by the equation $\sum_{i=1}^{4} x_i^4 = R^2$ in $\mathbb{R}^4$) on which they build a regular polytope (Schäfli symbol $\{3, 3, 5\}$) with 120 vertices of coordination number 12. This idea, later developed by several others (see Sadoc and Mosseri [14], Steinhardt *et al.* [15], Nelson [16], Kléman [17]), paved the way for a new approach to spatial disorder based on the interplay between order and geometry on three-dimensional manifolds of constant Gaussian curvature.

In-plane order on two-dimensional manifolds has been subject of intensive research since the discovery of the ordered phases L_β and P_β of phospholipidic membranes and is now a rich and mature chapter of condensed matter physics [18]. After the seminal work of Nelson and Peliti [19] on shape fluctuations in membranes with crystalline and hexatic order, much work has been done in elucidating the intimate relation between in-plane order and the geometry of the underlying substrate with many striking results and even more open questions. The fundamental role of topological defects in two-dimensional systems, first elucidated in a series of pioneeristic papers by Berezinskii [20], Kosterlitz and Thouless [21–23], becomes even more crucial in presence of a non-zero Gaussian curvature in the underlying medium, causing the appearance in the ground state of structures that would normally by suppressed in flat systems. The goal of this article is to review the most recent developments in the study of the ground state properties of two-dimensional order on curved media; that is the structure and the mechanics of ordered phases on two-dimensional substrates equipped with a non-zero Gaussian curvature, in a regime where thermal fluctuations are negligible in comparison with other energy scales of the system. While focusing on ground states we must remind the reader that finite temperature physics on curved spaces is not at all a subject devoid of charm or open problems. On the contrary, the extension of the statistical mechanics of two-dimensional systems to spaces with intrinsic curvature remains a challenge for the future.

The thesis is organized as it follows. In §2, I discuss the concept of geometrical

frustration and we review some fundamentals of the elasticity of topological defects in flat and curved spaces. §3 is dedicated to crystalline order on surfaces with variable Gaussian curvature and boundary. The existence of defective ground states in toroidal monolayers, with intrinsic crystalline or hexatic order, represents one of the most recent achievements in the study of order on curved surfaces and will be review in §4. Conclusions as well as some current and potential applications of defective structures to material science and nano-engineering will be discissed in §5.

1.2 Ordered structures in two-dimensional matter

Before discussing more technical aspects of the physics of ordered structures on curved surfaces we want to recall some salient features of physical systems with in-pane order and spatial curvature.

1.2.1 Amphiphilic Membranes

Amphiphilic membranes are thin sheets ($50 - 100$ Å) of amphiphilic molecules immersed in a fluid and organized in the form of a *bilayer* (see Fig. 1.2). The most common constituents of biological membranes are phospholipids consisting of a polar head group and a hydrophobic tail made up of two fatty acyl chains (see Fig. 1.1). Tails have typical length $14 - 20$ carbon atoms and regulate the thickness and the stability of the bilaryer. The polar head group contains one or more phosphate groups -POOH-O-R. Most phospholipid head groups belong to the phosphoglycerides, which contain glycerol joining the head and the tail. Examples of phosphoglycerides include phosphatidylcholine (PC), phosphatidylethanolamine (PE), phosphatidylserine (PS). These are distinguished by the residue R carried by the phosphate group (i.e. choline R=-CH_2-CH_2-N^+-$(CH_3)_3$, ethanolamine R=-CH_2-CH_2-NH_2). The fatty acyl chain in biomembranes usually contains an even number of carbon atoms. They may be saturated (neighboring C atoms are all connected by single bonds) or unsaturated

(some neighboring C atoms are connected by double bonds).

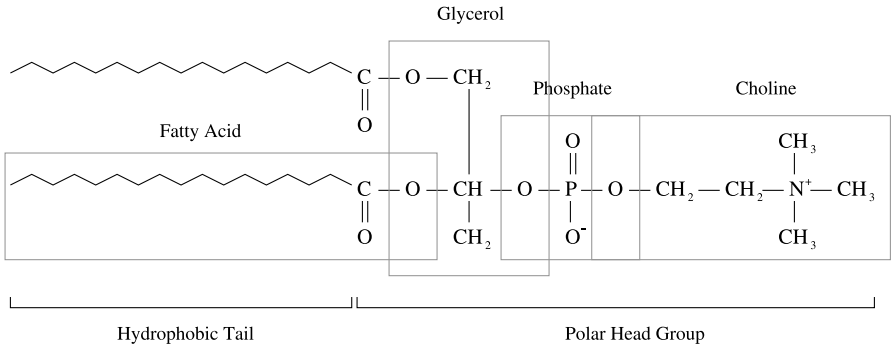

Figure 1.1: The structure of phosphatidylcholine.

At low temperature pure phospholipids crystallize and form a bilayer with all the tails in the *trans* configuration and the heads parallel to the bilayer surface and firmly linked into a lattice (mostly by hydrogen bonds). At higher temperature the order is disrupted first among the tails (*premelting* or *chain melting*) and later among the hydrophilic heads. The temperatures corresponding to these two transitions are known as *transition* (T_t) and *melting* (T_m) temperatures respectively. While T_m is relatively high for most phospholipids ($\sim$ 200 °C), the transition temperature T_t is closer to room temperature and increases with the length of the hydrocarbon tails. Most pure phospholipids are therefore in a phase where a fluid hydrocarbon layer is confined between two solid planes.

In solutions the bilayer can be found in a number of phases with differing degrees of order among the hydrocarbon chains. For phospholipids in the PC family these phases are usually called L_α, L_β and P_β. In the L_α phase, the tails are liquid and disordered. L_β is a solid-like phase in which hydrocarbon chains are ordered and the molecules don't diffuse freely. The order of the hydrocarbon chains also implies a larger thickness of the bilayer. The two lamellar phases can be separated by an intermediate "rippled" phase P_β in which the bilayer exhibits an undulated structure and almost solid-like diffusion properties. Hydrocarbon chains can also appear tilted with respect to the bilayer plane. Tilted phases are generally denoted as L'_β and P'_β.

There are in fact several L_β phases characterized by different amounts of tilt and in-plane orientational order [24].

Upon changing their concentration, amphiphiles in solutions aggregate in a large variety of structures other than bilayers. Above the *critical micelle concentration* (which is of the order of 10^{-3} mol/ℓ) spherical micelles appear (see Fig. 1.2). Their formation occurs more readily for single-chain amphiphiles (e.g. monoglycerids) and is favored by the presence of large head groups. At higher amphiphile concentrations spherical micelles are replaced by non-spherical ones and eventually by cylindrical rods. Spherical and cylindrical micelles can themselves organize in higher order structures such as cubic lattices or hexagonally packed rod piles. More exotic phases can be obtained by adding oil to the solution. Once the oil is dispersed in water, amphiphiles can form a monolayer across the water-oil interface and self-assemble in complex tubular structures known under the common name of *plumber's nightmare* [25].

1.2.2 Colloidosomes

The name *colloidosome* was coined by Dinsmore *et al.* to indicate microcapsules consisting of a shell of coagulated or partially fused colloidal particles surrounding a liquid core [26]. Because of their controllable size, elasticity and permeability, colloidosomes have been recognized to form a promising class of "soft devices" for the encapsulation and delivery of active ingredients with a variety of potential applications for development of novel drug and vaccine delivery vehicles and for the slow release of cosmetic and food supplements. Their major advantage relies on the fact that the permeability of the shell depends mainly on the size of the gaps between neighboring colloidal particles which can be tuned by controlling their size, interactions and degree of fusion. Velev *et al.* [27–29] were the first to report a method for the preparation of colloidosomes by templating octanol-in-water emulsions stabilized by latex particles and subsequently removing the octanol core by dissolution in

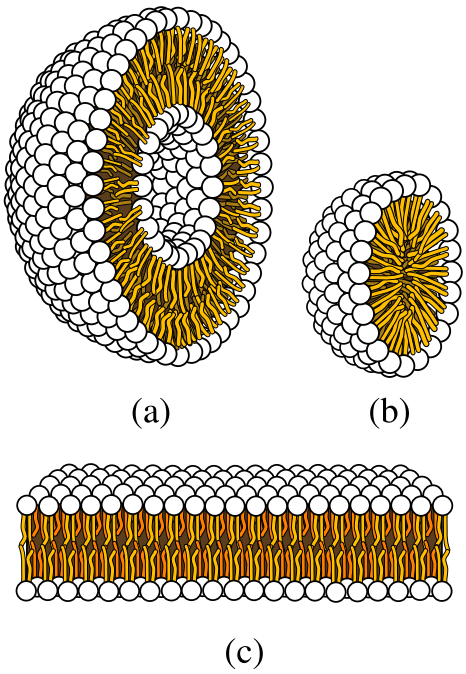

Figure 1.2: Example of structures formed form self-assembly of amphiphilic molecules. (a) a vesicle, (b) a micelle and (c) a bilayer. [Courtesy of Mariana Ruiz Villarreal].

ethanol. Structures of similar architecture have been obtained by templating water-in-oil emulsions [30, 31]. Multilayer shells consisting of alternating positive and negative polyelectrolytes and/or nanoparticles have also been prepared by using layer-by-layer assembly techniques, with the final hollow shells being obtained by removal of the central, sacrificial colloidal particles [32, 33]. Loxley and Vincent [34] developed a new way of preparing polymeric capsules with liquid cores based on a phase separation of the polymer within the templated emulsion. The colloidosomes produced by Dinsmore *et al.* [26] were obtained by the assembly of latex particles into shells around water-in-oil emulsion drops, followed by thermal fusion of the particles in the shell and centrifugal transfer into water through a planar oil-water interface.

The coverage of emulsified droplets by colloidal particles takes place by self-assembly. The particles dispersed in the fluid spontaneously adsorb on the interface provided the surface energy between the fluid on the inside and the outside of the

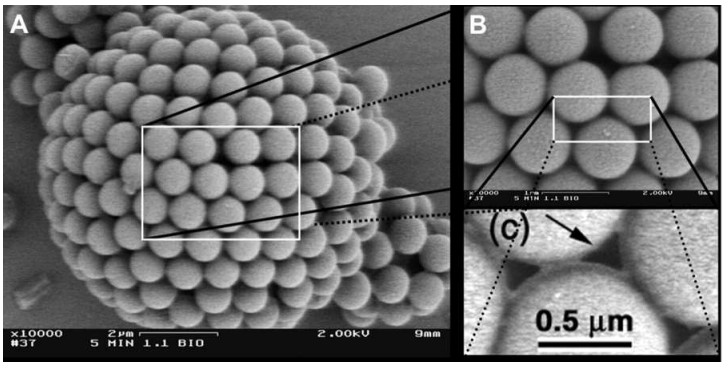

Figure 1.3: Scanning electron microscope image of a colloidosome from Dinsmore *et al.* [26]. The colloidosome is composed of 0.9 μm diameter polystyrene spheres sintered at 105 °C. The close-up on the left shows the effect of sintering at the contact points of neighboring spheres.

droplet ($\sigma_{i,o}$) is larger than the difference of those between the particles and the internal fluid ($\sigma_{p,i}$) and the particles and the external fluid ($\sigma_{p,o}$). Thus $\sigma_{i,o} > |\sigma_{p,i} - \sigma_{p,o}|$. A similar mechanism is used in Pickering emulsions, which are stabilized by surface adsorption of colloidal particles. Once adsorbed at the interface, interacting particles distribute evenly, assuring a full and uniform coverage of the droplet. The interactions depend on the type of colloidal particles used as well as the liquids. Coated polymethylmethacrylate (PMMA) or polystyrene spheres, for instance, acquire a permanent electric dipole moment at the interface between the two fluids, possibly because of the dissociation of charges on the hydrated surface similar to what happens at a water-air interface [35]. The resultant dipolar interaction stabilizes the particles and allows full coverage of the droplet.

The colloidal particles comprising the shell are then locked together to achieve the desired permeability and robustness of the colloidosome. Several techniques are available to achieve this. By sintering polystyrene particles at a temperature slightly above the glass transition ($T_g \approx 100$ °C), it is possible to achieve a partial fusion of neighboring particles at the contact points. This process also allows one to control precisely the size of the gaps between particles and therefore the permeability of the colloidosome. Another method consists of binding the particles with a polyelectrolyte

of opposite charge which can bridge neighboring particles and immobilize them at the interface. Particles locking clearly enhances the toughness of the colloidal shell and increases its rupture stress. For sintered polystyrene particles, the latter can be tuned in the range $1 - 100$ MPa. Colloidosomes locked with polyelectrolytes are even more deformable and can withstand strains of order 50 % before rupturing.

The crystalline arrangement of charged colloids on a hemispherical droplet has been recently studied by Irvine and Chaikin who fabricated colloidal suspensions of PMMA spheres at the interface between water and cyclohexyl bromide (CHB) [36]. Because of the large difference in dielectric constants, ions from the oil strongly partition into the water phase [37]. When nearly 100% PMMA particles are dispersed into the oil phase they form a Wigner crystal and a monolayer near the interface separated by a zone depleted of particles. These last two features are due the ion partitioning that provides the water phase with mobile charges. The net charge of water can be controlled through the pH, shifting the hydrolysis and ion partitioning equilibria. An electrically neutral water droplets acts as a conductor and attracts PMMA particles at the interface through an image charge mechanism. As a result, particles are almost non-wet by the water phase and organize in a perfect monolayer at (and not across) the interface.

1.2.3 Viral capsids

Viral capsids are protein shells that enclose the genetic material of a virus and protect it from enzymatic digestion. Capsid proteins are expressed from the DNA or RNA genome of the virus and in physiological conditions self-assemble in a very efficient structure which can withstand high forces (their Young modulus is ~ 2 MPa) and at the same time effectively disassemble to allow the viral genome to be released in the host cell. Most viral capsids have spherical or rod-like shape, but less standard shapes, such as conical or toroidal, also occur.

The crystallographic structure of spherical viruses has been object of intense in-

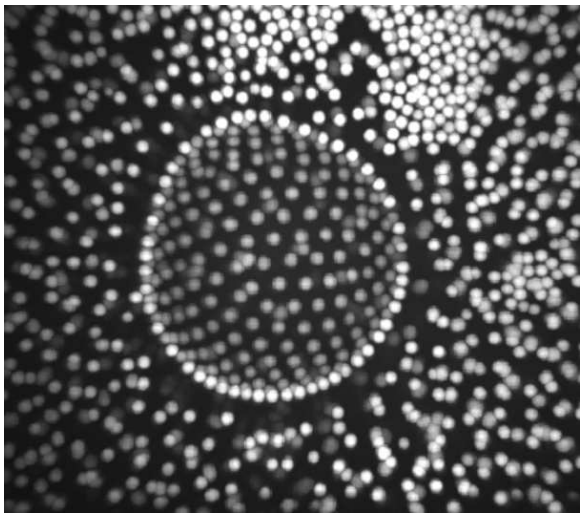

Figure 1.4: PMMA colloids sitting at the hemispherical interface between water and cyclohexyl bromide. The particles are positively charged and interact via a screened Coulomb interaction with Debye screening length proportional to the concentration of ions in the solvent. [Courtesy of W. Irvine and P. M. Chaikin, New York University, New York, NY].

vestigation and, thanks to the modern techniques of X-ray spectroscopy and cryo-transmission electron microscopy, is now part of the core knowledge of modern virology. In most of cases the capsid proteins are grouped in subunits called *capsomers*, oligomers made of either five (pentamer) or six (hexamer) proteins. Spherical viruses typically posses icosahedral symmetry with twelve pentamers located as the vertices of a regular icosahedron. The number of hexamers that complete the capsids is given by $10(T-1)$, where T, the triangulation number, takes values from a sequence of "magic numbers" (i.e. $T = 1, 3, 4, 7 \ldots$) associated with the lattice structure of the capsid, as brilliantly explained by Caspar and Klug (CK) in a seminal paper of 1962 [38] (the CK construction of icosahedral lattices will be reviewed in §3). The diameters of spherical viruses span the range 10 to 100 nm. While small capsids are almost perfectly spherical, large viruses, such as the bacteriophage HK97 or the phycodnavirus, typical exhibit a faceted geometry with nearly flat portions separated by ridges and sharp corners corresponding to the twelve pentamers. This morphological

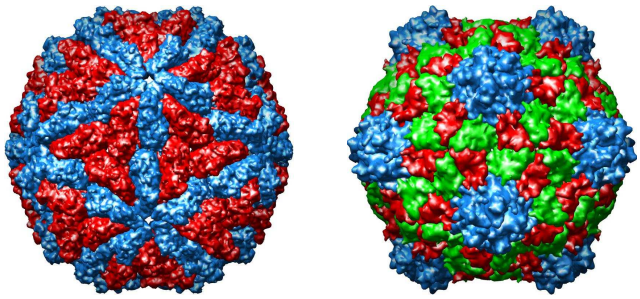

Figure 1.5: Two examples of viral capsids. The L-A virus (on the left) and the cowpea mosaic virus (CPMV) (on the right). Both have 60 capsomer, but the latter as a marked faceted geometry. From *VIPERdb* [45].

difference was explained by Lindmar *et al* [39] as a *buckling transition* resulting from the balance between the stretching energy associated with the pentamers in capsomer lattice and the bending elasticity of the viral capsid.

Nonicosahedral capsids of spherocylindrical shape are common among bacteriophages such as some T-even phages as well as the ϕCBK and the ϕ29. In this case the capsid appears as a cylindrical tube composed of a ring of hexamers closed at the ends by two half-icosahedral caps. This structure is also found in a variant of the $T = 7$ papovavirus and can be induced in other icosahedral viruses by point mutation in the capsid proteins [40, 41]. Of special interest are polymorphic viruses, which can appear in either spherical or spherocylindrical conformation. Polymorphism has been observed in the polyoma/SV40 animal virus [42] and the cowpea chlorotic mottle virus (CCMV) [43] and, for the latter case, appears to be related to the pH and salt concentration of the environment. The human immunodeficency virus (HIV) also shows broad polymorphism in its capsid shape, including cone-like structures in addition to tubular and spherical ones and has been subject of intense investigation in recent years [44].

1.2.4 Carbon nanotubes and related materials

The science of carbon nano-materials has experienced a period of phenomenal growth since carbon nanotubes (CNT) were found by Iijima in 1991 [46] and, since then, a large number of similar structures, including helix-shaped graphitic nanotubes [47], nanotori [48], carphitic nanocones [49] and nanoflowers [50] have been reported in the literature. The great enthusiasm surrounding this field has its origin in the exceptional properties that make CNT potentially useful in many applications in nanotechnology, electronics, optics and other fields of materials science. They exhibit extraordinary strength, unique electrical properties and are efficient conductors of heat. To date, several methods including laser pyrolysis, arc discharge, and electron irradiation, for preparation of graphitic nanomaterials, have been developed. Recently, metal-catalyzed methods have been used to synthesize carbon nanomaterials.

Most single wall nanotubes (SWNT) have diameter of about 1 nm, while the length is often of the order of microns. The lattice structure of a SWNT can be obtained from that of a graphene plane by assigning a pair of indices (n, m) which specify how the graphene lattice is rolled up into a seamless cylinder (see Sec. 4). $n = 0$ nanotubes are referred to as "zigzag", while $n = m$ tubules are called "armchair". The generic name "chiral" is used otherwise [51]. In terms of tensile deformations, SWNT are the stiffest materials known with a Young modulus in the range 1-5 TPa and a tensile strength of 13-53 GPa. This strength results from the covalent sp^2 bonds formed between the individual carbon atoms.

Because of the interplay between the unique electronic structure of graphene and tubular geometry, the lattice structure of a nanotube strongly affects its electrical properties. For a given (n, m) nanotube, a nanotube can be a conductor (if $n = m$), a small-gap semiconductors (if $n - m$ is a multiple of 3) or a standard semiconductor (otherwise). Thus all armchair $(n = m)$ nanotubes are metallic, and nanotubes with (n, m) equal (5,0), (6,4), (9,1), etc. are semiconducting.

Topological defects may occur on the side-wall of carbon nanotubes and related

materials in the form of atomic vacancies, $5-7$ dislocations and Stone-Wales defects [52] (i.e. quadrupoles consisting in two pairs of 5-membered and 7-membered rings) and are believed to deeply change the mechanical and transport properties of carbon nanotubes. The latter, in particular, were suggested to serve as possible nucleation centers for the formation of dislocations in the original ideal graphene network and constitute the onset of possible plastic deformations [53]. Electronic transport is affected by the presence of defects by lowering in the conductivity through the defective region of the tube. Some defect formation in armchair-type tubes (which can conduct electricity) can cause the region surrounding that defect to become semiconducting. Furthermore single monoatomic vacancies induce magnetic properties. Phonons scattering by defective regions heavily affects the thermal properties of carbon nanotube and leads to an overall reduction of the thermal conductivity. Phonon transport simulations indicate that substitutional defects such as nitrogen or boron will primarily lead to scattering of high frequency optical phonons. However, larger scale defects such as Stone Wales defects cause phonon scattering over a wide range of frequencies, leading to a greater reduction in thermal conductivity [54]. On the other hand, defective regions appear to be natural places for chemical functionalization. Numerical simulations have shown how the presence of Stone-Wales defects considerably enhances the adsorption of carboxyl groups (COOH) which can then bind to molecules with amide and ester bonds [55].

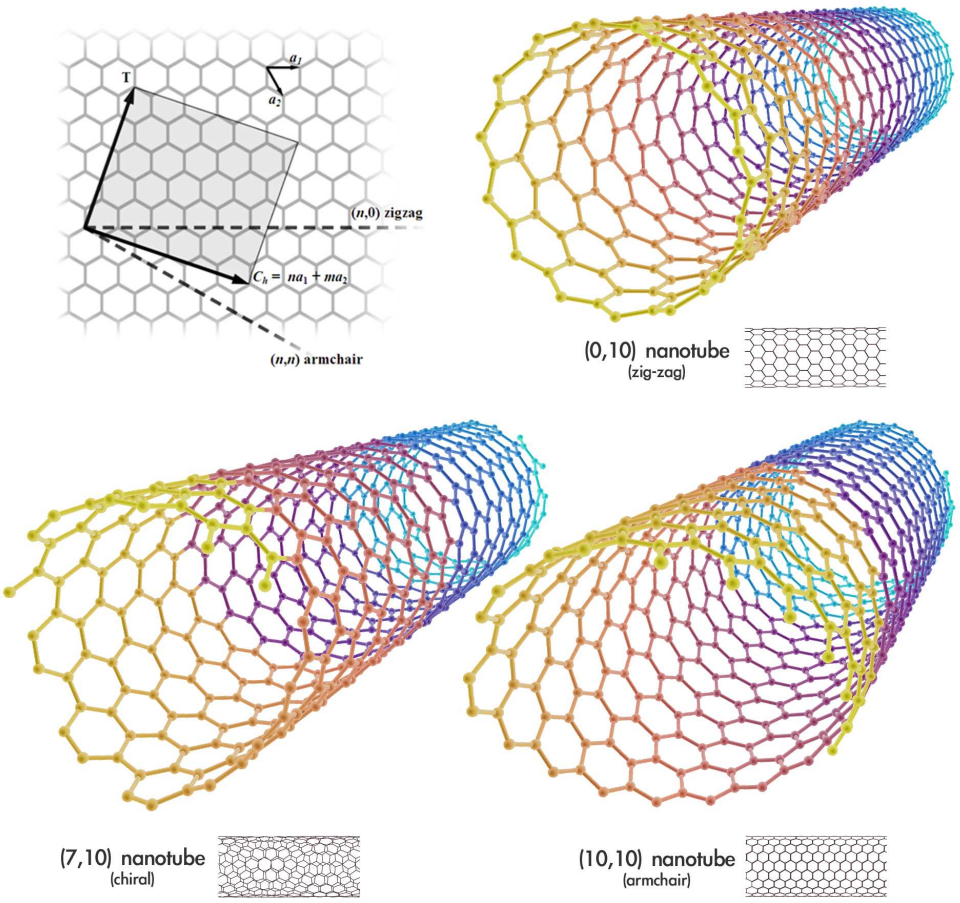

Figure 1.6: Examples of single wall carbon nanotubes. The chirality of the cylindrical lattice is determined by a pair of integer indices (n, m) which specify how a graphene plane is rolled up. From Wikipedia (http://en.wikipedia.org/wiki/Carbon_nanotube.)

Chapter 2

Interacting topological defects in curved media

2.1 Geometrical frustration

The notion of *geometrical frustration* was introduced to describe situations where certain types of local order, favoured by physical interactions, cannot propagate throughout a system [56]. The expression was used for the first time by Toulouse in 1977 [57] to describe certain particular magnetic systems with nearest-neighbours interactions which cannot be all satisfied simultaneously. A textbook example of frustration in magnetic models is represented by a system of Ising spins on a triangular lattice with antiferromagnetic bonds: while a perfect antiferromagnetic alignment would minimize all terms in the Ising Hamiltonian, such an alignment is not allowed by the topology of the underlying lattice so that for any triangular plaquette there is always at least one unsatisfied bond (see Fig. 2.1). This concept can be extended naturally to any system where interactions impose a local order, but the most favoured local configuration is geometrically incompatible with the structure of the embedding space.

Two-dimensional manifolds equipped with some microscopic field for which a notion of local order can be defined unambiguously provide a paradigm for systems

exhibiting geometrical frustration. Consider for instance an assembly of identical particles interacting with a spherically symmetric pair potential $V_{ij} = V(|\boldsymbol{x}_i - \boldsymbol{x}_j|)$, with $\boldsymbol{x}_i$ the position vector of the ith particle in a suitable coordinate system. In flat two-dimensional space, particles almost always pack in triangular lattices, unless the interaction potential is carefully tuned to select some some other lattice topology. Endowing the medium with a non-planar topology introduces frustration in the sense that the energetically favoured 6−fold orientational order can no longer be established everywhere in the system. Such geometrical frustration arises at the microscopic level from the celebrated Euler theorem of topology which relates the number of vertices V, edges E and faces F of any tessellation of a 2−manifold M:

$$V - E + F = \chi\,, \tag{2.1}$$

where χ is the Euler characteristic of M. If M is an orientable closed surface, one can show that χ is determined uniquely by an integer $g \geq 0$, called the *genus* of M, which represents the number of "handles" of M; namely $\chi = 2(1-g)$. Two orientable closed surfaces with the same genus (thus the same Euler characteristic) are homeomorphic: they can be mapped into one another without changing their topological properties. In a surface with boundary, the Euler characteristic is given by $\chi = 2(1-g) - h$, where h is the number of boundaries or "holes" of M. Thus a sphere, which has no handles nor boundary ($g = h = 0$) has $\chi = 2$, while the embedded torus ($g = 1$ and $h = 0$) has $\chi = 0$. A disk, on the other hand, has $\chi = 1$ ($g = 0$ and $h = 1$) and is topologically equivalent to a sphere with one hole. In §2-4 we we discuss ordered structures on three important topologies: the sphere, the disk and the torus.

In the case of two-dimensional crystals with 6−fold local order Eq. (2.1) can be rephrased in a form that is particularly useful in describing the presence of defects in the lowest energy state by defining a *topological charge* as the departure from the ideal coordination number of a planar triangular lattice: $q_i = 6 - c_i$ with c_i the coordination number of the ith vertex. Now, consider a tessellation in which each face is an n−sided polygon and let k faces meet at each vertex. Since each edge is

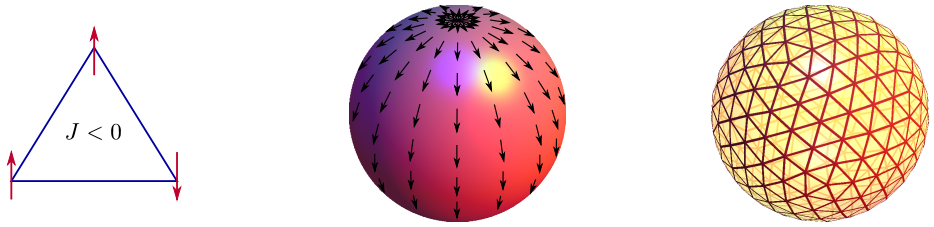

Figure 2.1: Examples of geometrical frustration. (Left) Ising antiferromagnet on a triangular lattice. Because of the topology of the underlying lattice, no arrangement of the three spins can minimize the Hamiltonian $H = -J \sum_{\langle ij \rangle} S_i S_j$. (Center) Vector field of a sphere. As a consequence of the Poincaré-Hopf theorem, a vector field must vanish at leat in two points, corresponding to the north and south pole of the sphere in this example. (Right) Triangulation of the sphere. As prescribed by the Euler theorem, any triangulation of the sphere must features a number of vertices of coordination number different than six (i.e. twelve 5−fold vertices in this case).

shared between two faces and links two vertices it follows that:

$$nF = 2E = \sum_k kV_k \,,$$

where V_k is the number of vertices of degree k. For a triangulation $n = 3$. From Eq. (2.1) it follows then:

$$Q = \sum_{i=1}^{V} q_i = 6\chi \,. \tag{2.2}$$

In the case of a sphere, with $\chi = 2$, Eq. (2.2) implies any triangulation contains a number of defective sites such that the total topological charge of the lattice is $Q = 12$. This can be achieved, for example, by incorporating twelve 5−fold disclinations (with $q = 1$) in a network of 6−fold coordinated sites like in a common soccer ball. These twelve disclinations, whose existence would be suppressed in the lowest energy state of a planar crystal, are the consequence of the geometrical frustration associated with the topology of the sphere.

Eq. (2.2) is a special case of geometrical frustration on 2-manifolds where local orientations are defined modulo $\pi/3$. More generally one can consider a p−atic director field for which local orientations are defined modulo $2\pi/p$. The topological charge of a disclination is in this case as $q = \Delta\theta/\frac{2\pi}{p}$, where $\Delta\theta$ is the angle the director

rotates in one counter-clockwise circuit of any closed contour enclosing the defect. Eq. (2.2) becomes then:

$$Q = \sum_{i=1}^{N} q_i = p\chi \tag{2.3}$$

where N is the total number of defects. The ratio $k = q/p$ is commonly referred to as the *winding number* of the disclination. In the case of a simple vector field, for instance, $p = 1$ and Eq. (2.3) corresponds to the well known Poincaré-Hopf theorem according to which the sum of the indices of all the isolated zeros of a vector field on a oriented differentiable manifold M is equal to the Euler characteristic χ of M. Thus for a sphere a vector field must have at least one sink and one source, each having topological charge one, while on a torus ($\chi = 0$) a vector field can be defect free. A nematic director $\boldsymbol{n}$, on the other hand, has $p = 2$ (i.e. physical configurations are invariant under inversions $\boldsymbol{n} \to -\boldsymbol{n}$). Thus disclinations with ± 1 topological charge correspond to configurations where the director rotates $\pm\pi$ in one circuit enclosing the defect. These elementary disclinations have semi-integer winding number $k = \pm 1/2$. As a consequence of Eq. (2.3) the total topological charge of a nematic texture on the sphere is $Q = 4$, corresponding for instance to the typical baseball texture consisting of four $q = 1$ ($k = 1/2$) disclinations located at the vertices of a regular tetrahedron [58, 59].

2.2 Mathematical preliminaries and notation

The equilibrium structure of two-dimensional locally ordered systems on curved substrates depends crucially on the existence and arrangement of the defects. Since the seminal works of Kosterlitz, Thouless, Halperin, Nelson and Young (KTHNY) on defect mediated melting in two dimensions it has become conventional to adopt a theoretical framework where the fundamental objects in the system are the defects themselves and treat the microscopic constituents within a continuum elastic theory. This approach has the advantage of far fewer degrees of freedom than a direct

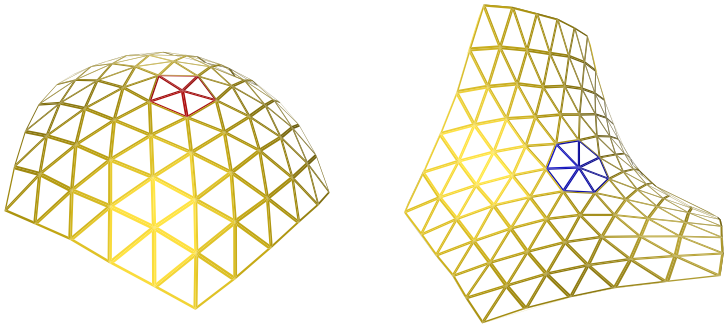

Figure 2.2: Example of 5−fold (right) and 7−fold (left) disclinations on a triangular lattice on a region of positive and negative Gaussian curvature rispectively.

treatment of the microscopic interactions and allows one the explore the origin of the emergent symmetry observed in non-Euclidean ordered structures as the result of the interplay between defects and geometry. The latter is one of the fundamental hallmarks of order on two-dimensional manifolds and leads to the universal features observed in systems as different as viral capsids and carbon macromolecules. In this section we will briefly review some concepts of differential geometry, mostly to establish notation. In the next section we will review some fundamentals of the elasticity of defects in two dimensions. The coupling mechanism between curvature and defects will be introduced in §2.4.

Points on a two-dimensional surface S embedded in $\mathbb{R}^3$ are specified by a three-dimensional vector $\boldsymbol{R}(\boldsymbol{x})$ as a function of a two-dimensional parameter $\boldsymbol{x} = (x^1, x^2)$. For each point of S we define three vectors:

$$\boldsymbol{g}_i = \partial_i \boldsymbol{R} \qquad i = 1,\, 2 \tag{2.4}$$

$$\text{and} \qquad \boldsymbol{n} = \frac{\boldsymbol{g}_1 \times \boldsymbol{g}_2}{|\boldsymbol{g}_1 \times \boldsymbol{g}_2|}\,, \tag{2.5}$$

where $\partial_i = \partial/\partial x^i$. The vectors $\boldsymbol{g}_i$ belongs to $T_{\boldsymbol{R}}S$, the tangent space of S at $\boldsymbol{R}$ while $\boldsymbol{n}$ is a normal vector. Note that while $\boldsymbol{n}$ is a unit vector, $\boldsymbol{g}_i$ are generally not of unit length. The metric, or *first fundamental form*, of S is defined as:

$$ds^2 = g_{ij} dx^i dx^j \tag{2.6}$$

where g_{ij} is the metric tensor:

$$g_{ij} = \boldsymbol{g}_i \cdot \boldsymbol{g}_j \tag{2.7}$$

The dual tensor is denoted as g^{ij} and is such that:

$$g_{ik} g^{jk} = \delta_i^j \,,$$

with δ_i^j the Kronecker symbol. This allows us to introduce contravariant tangent-plane vectors $\boldsymbol{g}^i = g^{ij}\boldsymbol{g}_j$, satisfying $\boldsymbol{g}_i \cdot \boldsymbol{g}^j = \delta_i^j$. Any vector $\boldsymbol{v}$ on the tangent plane can be expressed as a linear combination of basis vectors $\boldsymbol{g}_i$ and $\boldsymbol{g}^i$: $\boldsymbol{v} = v^i \boldsymbol{g}_i = v_i \boldsymbol{g}^i$, where $v_i = g_{ij} v^j$. The extrinsic curvature of the surface S is encoded in the tensor of the *second fundamental form* b_{ij} (also known as the extrinsic curvature tensor):

$$b_{ij} = -\boldsymbol{g}_i \cdot \partial_j \boldsymbol{n} = \boldsymbol{n} \cdot \partial_j \boldsymbol{g}_i \,. \tag{2.8}$$

The eigendirections of b_{ij} at a given point correspond to the principal curvature directions of S at that point and the associated eigenvalues κ_1 and κ_2 are the extremal (or principal) curvatures. The mean curvature H and the Gaussian curvature K are defined as the sum and the product of the principal curvatures:

$$2H = \kappa_1 + \kappa_2 = g_{ij} b^{ij} \tag{2.9}$$

$$K = \kappa_1 \kappa_2 = \tfrac{1}{2} \epsilon^{ik} \epsilon^{jl} b_{ij} b_{kl} \tag{2.10}$$

where ϵ^{ij} is the dual of the Levi-Civita tensor, whose components are given by:

$$\epsilon_{11} = \epsilon_{22} = 0$$

$$\epsilon_{12} = -\epsilon_{21} = \sqrt{g}$$

where $g = \det g_{ij}$. The contravariant form is $\epsilon^{ij} = \epsilon_{ij}/g$ and satisfies $\epsilon_{ik}\epsilon^{jk} = \delta_i^j$. Since $\epsilon_{ij} v^i v^j = 0$, where v^i is any contravariant vector, it follows that the vector $\epsilon_{ij} v^i$ is perpendicular to v^j. Thus inner multiplication by ϵ_{ij} rotates a vector by $\pi/2$. The covariant derivative of a vector field $\boldsymbol{v}$ in the ith coordinate direction is defined as

usual by:

$$\nabla_i v^k = \partial_i v^k + \Gamma^k_{ij} v^j \tag{2.11a}$$

$$\nabla_i v_k = \partial_i v_k - \Gamma^j_{ik} v_j \tag{2.11b}$$

where Γ^k_{ij} is the Christoffel symbol:

$$\Gamma^k_{ij} = \tfrac{1}{2} g^{kl} (\partial_j g_{il} + \partial_i g_{lj} - \partial_l g_{ij}) \,. \tag{2.12}$$

Both the metric and the Levi-Civita tensor are invariant under parallel transport. This translates into:

$$\nabla_k g_{ij} = \nabla_k g^{ij} = 0 \qquad \nabla_k \epsilon_{ij} = \nabla_k \epsilon^{ij} = 0 \,.$$

Much of the elastic theory of defects, either in flat or curved systems, relies on the calculation of the Green function of the Laplace operator. On a generic 2−manifold the latter obeys:

$$\Delta G_L(\boldsymbol{x}, \boldsymbol{y}) = \delta(\boldsymbol{x}, \boldsymbol{y}) \,, \tag{2.13}$$

where Δ is the Laplace-Beltrami operator:

$$\Delta = \frac{1}{\sqrt{g}} \partial_i \sqrt{g}\, g^{ij} \partial_j \tag{2.14}$$

and δ the delta-function:

$$\delta(\boldsymbol{x}, \boldsymbol{y}) = \frac{\delta(x^1 - y^1)\delta(x^2 - y^2)}{\sqrt{g}} \,. \tag{2.15}$$

The Stokes theorem is frequently invoked when calculating elastic energies of defects. In covariant form it can be stated as follows: given a vector field $\boldsymbol{v}$ on a 2−manifold M with boundary ∂M, the following identity holds:

$$\oint_{\partial M} dx^k \, v_k = \int_M d^2x \, \epsilon^{ij} \nabla_i v_j \,. \tag{2.16}$$

For sake of consistency we will adopt covariant notation throughout this paper. When discussing planar systems, in particular, we have: $b_{ij} = H = K = 0$ and the elements

of the metric tensor are given in Cartesian coordinates by $g_{xx} = g_{yy} = 1$, $g_{xy} = g_{yx} = 0$ and in polar coordinates by $g_{rr} = 1$, $g_{\phi\phi} = r^2$, $g_{r\phi} = g_{\phi r} = 0$.

The definition of orientational order on a surface clearly requires a non-ambiguous notion of angular distance between vectors on the same tangent plane. This is traditionally achieved by introducing a pair of orthonormal vectors $\boldsymbol{e}_\alpha$ ($\alpha = 1, 2$) called *vielbin* (note that the canonical coordinate vectors $\boldsymbol{g}_i$ are generally neither orthonormal nor orthogonal) so that:

$$\boldsymbol{e}_\alpha \cdot \boldsymbol{e}_\beta = (e_\alpha)_i (e_\beta)^i = \delta_{\alpha\beta} \,, \qquad\qquad (e_\alpha)_i (e_\alpha)_j = g_{ij} \,, \tag{2.17}$$

where $\delta_{\alpha\beta}$ is the usual Kronecker symbol in the indices α and β. A vector field $\boldsymbol{v} = v^i \boldsymbol{g}_i$ can be expressed alternatively in the basis $\boldsymbol{e}_\alpha$:

$$\boldsymbol{v} = v^\alpha \boldsymbol{e}_\alpha \qquad\qquad v^\alpha = v^i (e_\alpha)_i \,.$$

Clearly, since the coordinates v^α are locally Cartesian, $\delta_{\alpha\beta} = \delta^{\alpha\beta}$ and there is no distinction between upper and lower Greek indices: $v_\alpha = v^\alpha$. Vielbin are constructed to be invariant under parallel transport, thus $\nabla_i (e_\alpha)_j = 0$ and:

$$\nabla_i v_\alpha = (e_\alpha)_j \nabla_i v^j = \partial_i v_\alpha + \Omega_{i\alpha\beta} v_\beta \,,$$

where $\Omega_{i\alpha\beta}$ is the so called *spin connection*, and is given by:

$$\Omega_{i\alpha\beta} = \boldsymbol{e}_\alpha \cdot \partial_i \boldsymbol{e}_\beta = \Gamma^k_{ij} (e_\alpha)^j (e_\beta)_k - (e_\beta)_k \partial_i (e_\alpha)^k \,.$$

Taking the derivative of the left equation in (2.17) one immediately sees:

$$(e_\alpha)^k \partial_i (e_\beta)_k = -(e_\beta)^k \partial_i (e_\alpha)_k \,,$$

from which it follows $\Omega_{i\alpha\beta} = -\Omega_{i\beta\alpha}$. In two-dimensions this makes possible the parametrization of the spin-connection $\Omega_{i\alpha\beta}$ by a single covariant vector $\boldsymbol{\Omega}$ (i.e. because of the antisymmetry under exchange of the Greek indices one has only $d^2(d-1)/2 = 2$ independent components in $d = 2$ dimensions). Namely:

$$\Omega_{i\alpha\beta} = \epsilon_{\alpha\beta} \Omega_i \,, \tag{2.18}$$

with $\epsilon_{\alpha\beta} = \delta^1_\alpha\delta^2_\beta - \delta^1_\beta\delta^2_\alpha$ the antisymmetric symbol.

It is well known how the curvature of a manifold manifests itself when a vector is parallel transported around a closed path. Taking an infinitesimal square loop of sides dx and dy, the parallel transported vector $\boldsymbol{v}'$ differs from the original vector $\boldsymbol{v}$ by an amount:

$$v'^k - v^k = R^k_{lij} v^l dx^i dy^j \,, \tag{2.19}$$

where R^k_{lij} is the Riemann tensor given in two-dimensions by:

$$R^l_{ijk} = K\epsilon^l_i\epsilon_{jk} \,. \tag{2.20}$$

In the orthonormal basis $\boldsymbol{e}_\alpha$, Eq. (2.19) reads:

$$v'_\alpha - v_\alpha = R_{ij\alpha\beta} v_\beta dx^i dy^j \,,$$

where $R_{ij\alpha\beta}$ is the curvature tensor associated with the spin-connection $\Omega_{i\alpha\beta}$:

$$R_{ij\alpha\beta} = \partial_i\Omega_{j\alpha\beta} - \partial_j\Omega_{i\alpha\beta} + \Omega_{i\alpha\gamma}\Omega_{j\gamma\beta} - \Omega_{j\alpha\gamma}\Omega_{i\gamma\beta} \,. \tag{2.21}$$

In two dimensions, using Eq. (2.20), one can write:

$$R_{ij\alpha\beta} = (e_\alpha)^k (e_\beta)^l R_{ijkl} = (e_\alpha)^k (e_\beta)^l \epsilon_{ij}\epsilon_{kl} K = \epsilon_{\alpha\beta}\epsilon_{ij} K \,,$$

which combined with Eqs. (2.21) and (2.18), can be used to obtain:

$$R_{ij\alpha\beta} = \epsilon_{\alpha\beta}(\partial_i\Omega_j - \partial_j\Omega_i) = \epsilon_{\alpha\beta}\epsilon_{ij} K \,, \tag{2.22}$$

which also implies:

$$\nabla \times \boldsymbol{\Omega} = \epsilon^{ij}\nabla_i\Omega_j = K \,. \tag{2.23}$$

2.3 Elasticity of defects on the plane

The $XY-$model is the simplest setting where particle-like objects emerges form a purely continuum theory [21–23]. The order parameter is the angular field $\theta \in [0, 2\pi]$

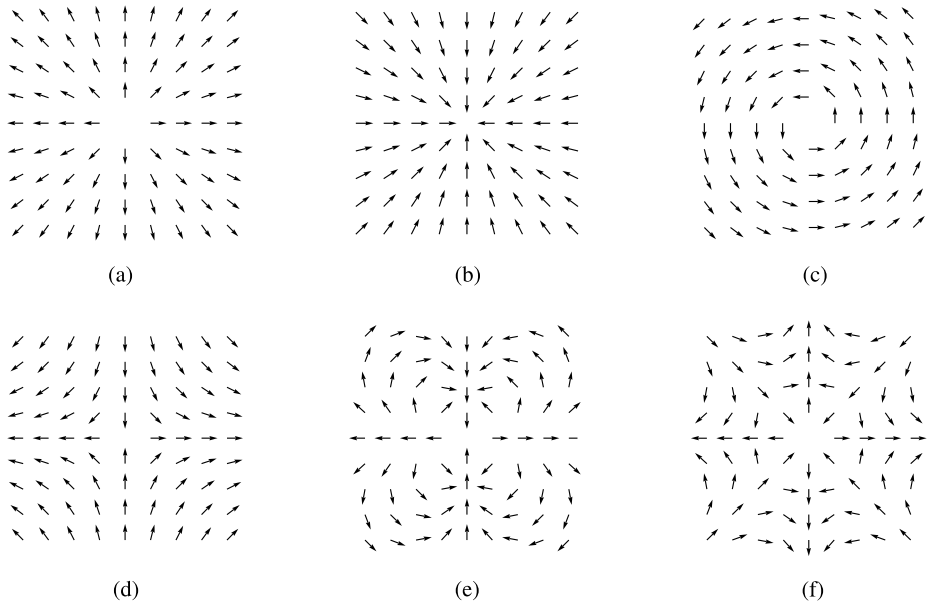

Figure 2.3: Example of topological defects in a vector field. (a), (b) and (c) have topological charge $q = 1$, (d) $q = -1$ and (e) and (f) have charge $q = 3$ and $q = -3$ rispectively.

which may represent the orientation of two-dimensional vectors $\boldsymbol{S} = S(\cos\theta, \sin\theta)$ or the phase of a complex field $\psi = |\psi|e^{i\theta}$. The interaction that tends to minimize the spatial variations of the order parameter results from the continuum free energy:

$$F_{el} = \frac{1}{2} K_A \int d^2x \, |\nabla\theta(\boldsymbol{x})|^2 \,. \tag{2.24}$$

Despite its simplicity this model successfully describes several aspects of the physics of vortices in superfluid ^{4}He or thin superconducting films, where the angle θ is identified with the phase of the collective wave function. Eq. (2.24) also describes nematic liquid crystals under the assumption of equal spay and bending stiffness. This approximation, however, favors $q = \pm 2$ ($k = \pm 1$) disclinations rather than the more natural $q = \pm 1$ ($k = \pm 1/2$) disclinations of nematics and is not particularly suitable to describe the ground state. At $T > 0$, thermal fluctuations drive the two elastic constants to the same value at long wavelengths, so that there is a unique Kosterlitz-Thouless transition temperature [60]. As discussed by Deem [61], the essential effect of unequal elastic constants is to create a distinct long-range contribution to the core

energy of each defect. More generally Eq. (2.24) can be considered as the simplest phenomenological free energy describing $p-$atic order (assuming θ defined modulo $2\pi/p$). Calling $\boldsymbol{v} = \nabla\theta$, the minimization of the free energy (2.24) leads to the equilibrium condition:

$$\Delta\theta = \nabla_i v^i = 0\,. \tag{2.25}$$

In the presence of a number of disclinations of topological charge q_α, θ changes of an amount $(2\pi/p)\sum_\alpha q_\alpha$ in one circuit along any contour enclosing a total topological charge $\sum_\alpha q_\alpha$:

$$\oint d\theta = \oint dx^i\, v_i = \frac{2\pi}{p}\sum_\alpha q_\alpha\,. \tag{2.26}$$

Using the Stokes theorem, Eq. (2.26) can be translated into the requirement:

$$\epsilon^{ij}\nabla_i v_j = \epsilon^{ij}\nabla_i\nabla_j\theta = \eta(\boldsymbol{x})\,, \tag{2.27}$$

where:

$$\eta(\boldsymbol{x}) = \frac{2\pi}{p}\sum_\alpha q_\alpha\delta(\boldsymbol{x},\boldsymbol{x}_\alpha)$$

is the topological charge density. Using standard manipulations (see for example [62]) a vector field $\boldsymbol{v}$ satisfying Eq. (2.25) with the constraint (2.26) can be found in the form:

$$v_i(\boldsymbol{x}) = -\epsilon_i^j\nabla_j\int d^2y\, G_L(\boldsymbol{x},\boldsymbol{y})\eta(\boldsymbol{y}) \tag{2.28}$$

where $G_L(\boldsymbol{x},\boldsymbol{y})$ is the Laplacian Green function. Using Eq. (2.28) in Eq. (2.24) leads to the well known expression:

$$F_{el} = -\frac{1}{2}K_A\int d^2x\, d^2y\, G_L(\boldsymbol{x},\boldsymbol{y})\eta(\boldsymbol{x})\eta(\boldsymbol{y})\,. \tag{2.29}$$

Like charged particles, disclinations interact via a Coulomb potential, which in two dimensions is proportional to the logarithm of the distance in the plane. As we noted, this framework is valid for both nematic liquid crystals in the one elastic constant approximation and superfluids. An important difference between these two systems lies in the choice of the boundary condition for the field θ. Nematogens are typically

forced to be normal to boundary of the substrate and this implies a constraint for θ, while such a constraint doesn't exist in the case of ^{4}He films, since the wave function is defined in a different space from that to which superfuild is confined. This difference is crucial on a curved substrate (see Ref. [63] for a detailed review of the topic).

Eq. (2.29) represents the elastic energy associated with the distortion introduced by defects in the *far field*, where the elastic variables change slowly in space. This expression breaks down in the neighborhood (or *core*) of a defect, where the order parameter is destroyed and the actual energetic contribution depends on microscopic details. In order to describe a defective system at any length scale, Eq. (2.29) must be corrected by adding a core energy F_c representing the energetic contribution within the core of a defect, where standard elasticity breaks down. A detailed calculation of the core energy requires some microscopic model and is usually quite complicated. Nonetheless its order of magnitude can be estimated by writing:

$$F_c = \pi a^2 f_c \,, \tag{2.30}$$

where a is the core radius, corresponding to the short distance cut-off of the elastic theory, and f_c is some unknown energy density independent on a. f_c can then be estimated by minimizing the total energy of the system with respect to a. For a planar system with a single disclination of winding numer k, the total energy can be easily calculated form Eqs. (2.29) and (2.30) in the form:

$$F = \pi K_A k^2 \log\left(\frac{R}{a}\right) + \pi a^2 f_c \,. \tag{2.31}$$

Minimizing Eq. (2.31) with respect to a, one finds $f_c = K_A k^2/(2a^2)$ from which:

$$F_c = \frac{1}{2}\pi K_A k^2 = \epsilon_c k^2 \,. \tag{2.32}$$

The quantity ϵ_c is the energy needed to increase the number of defects of one unit, independently on its position.

The elasticity of dislocations and disclinations in solids resembles in many aspects that of vortex lines in the $XY-$model. In two dimensional elasticity a pure in-plane

deformation is encoded in a displacement field u^i, $i = 1, 2$, which maps any point in the system $\boldsymbol{x}$ to:

$$\boldsymbol{x}' = \boldsymbol{x} + u^i \boldsymbol{g}_i \tag{2.33}$$

where $\boldsymbol{g}_i$ is a suitable basis in the coordinates of the undeformed system. If there are no defects, the displacement field is a single-valued mapping of the plane into itself. Topological defects introduce an incompatibility in the displacement field, in the sense that u^i is not a single-valued mapping anymore. The elastic stress in the region surrounding a defect appears at the macroscopic level from the Hooke's law of elasticity:

$$u_{ij} = \frac{1+\nu}{Y}\,\sigma_{ij} - \frac{\nu}{Y}\,g_{ij}\sigma^k_k \tag{2.34}$$

where Y and ν are the two-dimensional Young modulus and Poisson ratio respectively and σ_{ij} is the stress tensor. Eq. (2.34) can obtained, for example, by minimizing the elastic energy:

$$F = \int d^2x\, \left(\tfrac{1}{2}\lambda u_i^{i\,2} + \mu u_{ij}u^{ij}\right) \tag{2.35}$$

where λ and μ are the Lamé coefficients in two dimensions:

$$\lambda = \frac{Y\nu}{1-\nu}\,, \qquad\qquad \mu = \frac{Y}{2(1+\nu)}\,.$$

In absence of body forces, the force balance equation requires σ_{ij} to be divergence free:

$$\nabla_j \sigma^{ij} = 0\,. \tag{2.36}$$

The strain tensor u_{ij} represents the variation in the first fundamental form of the surface due to the deformation field (2.33), namely:

$$2u_{ij} = g_{ij}(\boldsymbol{x}+\boldsymbol{u}) - g_{ij}(\boldsymbol{x}) = \nabla_i u_j + \nabla_j u_i + O(u^2)\,. \tag{2.37}$$

In the presence of a dislocation line L the function $\boldsymbol{u}$ becomes multivalued so that, while traversing any closed counterclockwise loop C containing L:

$$\oint_C d\boldsymbol{u} = \boldsymbol{b}\,, \tag{2.38}$$

where $\boldsymbol{b}$ is the Burgers vector representing the amount by which the image of a closed loop under the mapping (2.33) fails to close in presence of a dislocation line [64, 65]. If L is an isolated straight dislocation with origin at the point $\boldsymbol{x}_0$, Eq. (2.38) implies:

$$\epsilon^{ij}\nabla_i\nabla_j u_k = b_k \delta(\boldsymbol{x}, \boldsymbol{x}_0)\,. \tag{2.39}$$

Generally speaking, maps such as that of Eq. (2.33), induce variations in both the length and the orientation of an infinitesimal distance vector $d\boldsymbol{x}$ in the deformed medium. This statement can be clarified by writing:

$$dx_i' - dx_i = (\nabla_j u_i)\, dx^j = (u_{ij} - \omega_{ij})\, dx^j$$

where:

$$\omega_{ij} = \tfrac{1}{2}\left(\nabla_i u_j - \nabla_j u_i\right) \tag{2.40}$$

is the infinitesimal rotation tensor induced by the deformation Eq. (2.33). In two dimensions the latter can be conveniently written in the form:

$$\omega_{ij} = \epsilon_{ij}\,\Theta \tag{2.41}$$

with:

$$\Theta = \tfrac{1}{2}\,\epsilon^{ik}\nabla_i u_k\,. \tag{2.42}$$

Since the application of ϵ_{ij} to a vector rotates the vector by $\pi/2$ clockwise, the coefficient Θ in Eq. (2.42) can be interpreted as the *average rotation* of an infinitesimal line element under a distortion of the form Eq. (2.33). In presence of an isolated disclination the field Θ becomes multi-valued. If s is the angular deficit associated with the disclination, integrating along a circuit enclosing the disclination core yields:

$$\oint_C d\Theta = s \tag{2.43}$$

which again can be rephrased as a statement about commutativity of partial derivatives:

$$\epsilon^{ij}\nabla_i\nabla_j\Theta = s\,\delta(\boldsymbol{x}, \boldsymbol{x}_0)\,, \tag{2.44}$$

where $\boldsymbol{x}_0$ the position of the disclination core. In a lattice with $n-$fold rotational symmetry, $s = (2\pi/n)q$, where q is the topological charge introduced above. A comparison between Eq. (2.27) and Eq. (2.44) clarifies the common identification of Θ with the *bond angle field* of a crystal [66].

Eqs. (2.39) and (2.44) provide a set of relations between the fundamental features of topological defects in crystals (i.e. the Burgers vector $\boldsymbol{b}$ and the topological charge q) and the partial derivatives of the displacement field $\boldsymbol{u}$. Those relations can be now used to derive an equation for the elastic stress arising in a system as a consequence of the defects. A simple and elegant way to achieve this task in the context of planar elasticity relies on the parametrization of the stress tensor via a single scalar field χ known as the Airy stress function (see for example [67]). Taking advantage of the commutativity of partial derivatives in Euclidean space, one can write

$$\sigma^{ij} = \epsilon^{ik}\epsilon^{jl}\nabla_k\nabla_l\chi \tag{2.45}$$

so that the force balance condition (2.36) is automatically satisfied. Then, applying the operator $\epsilon^{ik}\epsilon^{jl}\nabla_k\nabla_l$ to both sides of Eq. (2.34) and using Eq. (2.45) one finds the following fourth order Poisson-like problem:

$$\Delta^2\chi(\boldsymbol{x}) = Y\eta(\boldsymbol{x})\,, \tag{2.46}$$

where Δ^2 is the biharmonic operator and η is the defect charge density:

$$\eta(\boldsymbol{x}) = \frac{2\pi}{n}\sum_\alpha q_\alpha\delta(\boldsymbol{x}-\boldsymbol{x}_\alpha) + \sum_\beta \epsilon^{ij}b_i^\beta\,\nabla_j\delta(\boldsymbol{x}-\boldsymbol{x}_\beta)\,,$$

where s_α denotes the topological charge of a disclination at $\boldsymbol{x}_\alpha$ and $\boldsymbol{b}^\beta$ the Burgers vector of a dislocation at $\boldsymbol{x}_\beta$.

Let's now turn our attention to the case of a planar crystal with local $6-$fold orientational symmetry populated with N disclinations of density:

$$\eta(\boldsymbol{x}) = \frac{\pi}{3}\sum_{\alpha=1}^{N} q_\alpha\delta(\boldsymbol{x},\boldsymbol{x}_\alpha)\,. \tag{2.47}$$

Assuming a free boundary (i.e. all the components of the stress tensor are zero along the boundary and thus $\chi = \nabla\chi = 0$), the stress function χ can be expressed in the Green form:

$$\frac{\chi(\boldsymbol{x})}{Y} = \int d^2y\, G_{2L}(\boldsymbol{x},\boldsymbol{y})\eta(\boldsymbol{y})\,, \tag{2.48}$$

where $G_{2L}(\boldsymbol{x},\boldsymbol{y})$ is the biharmonic Green function. The elastic energy of the system is given by Eq. (2.35) and (2.48) in the form:

$$F_{el} = \frac{1}{2}Y \int d^2x\, d^2y\, G_{2L}(\boldsymbol{x},\boldsymbol{y})\eta(\boldsymbol{x})\eta(\boldsymbol{y})\,, \tag{2.49}$$

Eq. (2.24) and (2.49) are the fundamental equations in the elastic theory of defects in two-dimensional planar $p-$atics and crystals. In the next section we will see how a non-zero Gaussian curvature in the underlying medium affects these energies by effectively screening the topological charge of the defects.

2.4 Coupling mechanisms between curvature and defects

The elasticity of topological defects on curved substrates equipped with local orientational order was first considered by Nelson and Peliti in the context of hexatic membranes [19]. It is now part of the core knowledge in the statistical mechanics of membranes that long range forces appearing as the consequence of a local orientational order crucially affect the behavior of membranes at finite temperature. The stiffness associated with orientational correlations leads to an enhancement of the bending rigidity that counteracts the thermal softening that occurs in fluid membranes. Furthermore, for planar membranes, the stabilizing effect induced by the orientational stiffness opposes the entropy-driven tendency to *crumple*, causing a transition between a flat and crumpled phase at $T > 0$. In this article we focus on the ground state properties of ordered structures on curved surfaces and we remind the reader the specialized literature for a discussion on finite temperature physics [18].

In this section we will show how an underlying non-zero Gaussian curvature couples with the defects by *screening* their topological charge. As a result, topological defects, whose existence would be energetically suppressed if the same system was lying on a flat substrate, instead proliferate. The universality of such a curvature screening mechanism is remarkable in the sense that it occurs in a conceptually identical fashion in both $p-$atics and solids, although the kernel of the elastic interactions between defects differs. As a consequence of curvature screening topological defects organize themselves on a rigid surface so as to match the Gaussian curvature of the substrate. On the other hand, if the geometry of the substrate is allowed to change (for instance by lowering the bending rigidity) the system eventually enters a regime where the substrate itself changes shape in order to accommodate some preferential in-plane order. The latter is the fundamental mechanisms behind the *buckling* of crystalline membranes [68] and is believed to be the origin of the polyhedral geometry of large spherical viruses such as bacteriophages [69].

In the case of manifolds equipped with a pure rotational degree of freedom like $p-$atics, the curvature affects the elastic energy through the connection which determine how vectors change when parallel transported. This statement can be clarified by rewriting the elastic energy (2.24) in the form:

$$F_{el} = \frac{1}{2} K_A \int d^2x \, \nabla_i m^j \nabla^i m_j \tag{2.50}$$

where $\boldsymbol{m}$ is a $p-$atic director field which can be conveniently expressed in a local orthonormal frame $\boldsymbol{e}_\alpha$ ($\alpha = 1\,2$):

$$\boldsymbol{m} = \cos\theta \, \boldsymbol{e}_1 + \sin\theta \, \boldsymbol{e}_2 \,,$$

where θ is defined modulo $2\pi/p$. Since $\partial_i m_\alpha = -\epsilon_{\alpha\beta} m_\beta \partial_i \theta$, using the properties of vielbin outlined in §2.2, we have:

$$\nabla_i m_j = (e_\alpha)_j (\partial_i m_\alpha + \Omega_{i\alpha\beta} m_\beta) = -\epsilon_{\alpha\beta} m_\beta (e_\alpha)_j (\partial_i \theta - \Omega_i) \tag{2.51}$$

The elastic energy (2.50) becomes thus:

$$F_{el} = \frac{1}{2} K_A \int d^2x \, g^{ij} (\partial_i \theta - \Omega_i)(\partial_j \theta - \Omega_j) \tag{2.52}$$

Using Eq. (2.23), the vector field $\mathbf{\Omega}$ can be expressed as:

$$\Omega_i = -\epsilon_i^j \nabla_j \int d^2x \, G_L(\boldsymbol{x}, \boldsymbol{y}) K(\boldsymbol{y}) \,, \tag{2.53}$$

where $G_L(\boldsymbol{x}, \boldsymbol{y})$ is again the Green function of the Laplace-Beltrami operator (2.14). Replacing Eq. (2.53) and (2.28) in the expression for the elastic energy (2.52) we obtain:

$$F_{el} = -\frac{1}{2} K_A \int d^2x \, d^2y \, G_L(\boldsymbol{x}, \boldsymbol{y}) [\eta(\boldsymbol{x}) - K(\boldsymbol{x})][\eta(\boldsymbol{y}) - K(\boldsymbol{y})] \,. \tag{2.54}$$

As anticipated, the Gaussian curvature of the underlying substrate couples with the defects by screening their topological charge. Eq (2.54) is identical to the Coulomb energy of a multi-component plasma of charge density η in a background of charge density $-K$. Like particles in a plasma, we can expect defects to screen each other's charge, thus forming clusters of zero net charge, and matching the charge distribution of the surrounding background. This implies that disclinations will be attracted by regions of like-sign Gaussian curvature.

Crystalline surfaces (i.e. non-Euclidean crystals) differs from manifolds equipped with a $p-$atic director field because bonds, whose local orientation is encoded in the field θ in $p-$atics, can now be compressed and sheared to relieve part of the elastic stress due to the geometrical frustration provided by the embedding manifold. A first attempt at describing the elasticity of defects on a two-dimensional curved crystal was made by Dodgson [70], who studied the ground state of the Abrikosov fulx lattice in a model thin-film superconductor on a sphere (subject to a field radiating from a magnetic monopole at the center) and found evidence for twelve $5-$fold disclinations at the vertices of an icosahedron in a otherwise $6-$fold coordinated environment (see §2.5 for a review of spherical crystals). Later, Dodgson and Moore [71] proposed adding dislocations to the ground state of a sufficiently large spherical vortex crystal

to screen out the strain introduced by the twelve, topologically required, disclinations. A general framework to describe the elasticity of defects in non-Euclidean crystals was proposed by Bowick, Nelson and Travesset (BNT) in 2000 [72]. The BNT model, obtained from the covariantization of the elastic energy (2.49), relies on the following expression for the elastic energy of a collection of disclinations in a triangular lattice of underlying Gaussian curvature K:

$$F_{el} = \frac{1}{2} Y \int d^2x\, d^2y\, G_{2L}(\boldsymbol{x}, \boldsymbol{y})[\eta(\boldsymbol{x}) - K(\boldsymbol{x})][\eta(\boldsymbol{y}) - K(\boldsymbol{y})]\,, \tag{2.55}$$

where $\eta(\boldsymbol{x})$ is the topological charge density (2.47) and $G_{2L}(\boldsymbol{x}, \boldsymbol{y})$ the Green function of the covariant biharmonic operator on the manifold. The origin of the coupling between topological charge and curvature, in this case, is rooted in a profound result of discrete geometry originally due to Descartes which can be considered the oldest ancestor of the Gauss-Bonnet theorem of differential geometry. Let P be a convex polyhedron and define the *angular deficit* of a vertex v of P as:

$$k(v) = 2\pi - \sum_{i=1}^{c(v)} \alpha_i(v)\,, \tag{2.56}$$

where $\alpha_i(v)$ with $i \in [1, c(v)]$ are the angles formed by all the faces meeting at v. Descartes' theorem states that the sum of the angular deficits of a convex polyhedron is equal to 4π. More generally:

$$\sum_{v \in P} k(v) = 2\pi\chi \tag{2.57}$$

which is exactly the Gauss-Bonnet theorem for the case in which the Gaussian curvature is concentrated in a finite number of points (vertices) rather than smoothly distributed across the whole surface. The deficit angle $k(v)$ is thus the discrete analog of the Gaussian curvature. This analogy is not limited exclusively to Eq. (2.56). Consider, for example, the corner of a cube and imagine to parallel transporting a vector $\boldsymbol{v}$ along a close loop surrounding the corner (see Fig. 2.4). After parallel transport, the vector has rotated by $k(v) = \pi/2$ with respect to its original orientation.

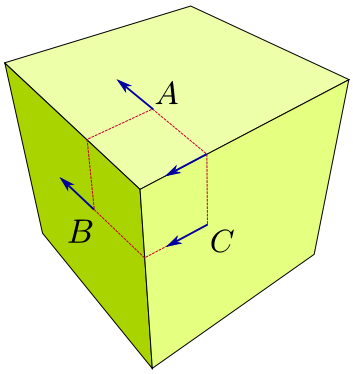

Figure 2.4: Parallel transport of a vector around a corner of a cube. As a consequence of the discrete Gaussian curvature, the vector rotate by $\pi/2$ after parallel transport.

Analogously, a parallel transported vector along a closed loop on a surface rotates by an angle

$$\delta = \int d^2x\, K(x)$$

where the integral is extended to the portion of surface enclosed by the loop. Now, on a triangulated surface $\alpha(v) \approx \pi/3$ and:

$$k(v) = 2\pi - \frac{\pi}{3}\, c(v) = \frac{\pi}{3}[6 - c(v)]\,.$$

Thus the source term $\eta - K$ figuring in Eq. (2.55) corresponds to the difference between the pre-existing Gaussian curvature of the manifold with local 6−fold orientational order and the additional Gaussian curvature induced by a disclination of topological charge q. A more formal discussion can be found in Ref. [73]. As in the case of a purely rotational degree of freedom, disclinations in non-Euclidean crystal arrange in the lattice in such a way to match the Gaussian curvature of the underlying medium while maximizing their reciprocal distance as a consequence of the repulsive interaction between like-sign defects. In the next three sections we will see how the formalism outlined here applies to three physically relevant examples of manifolds: the sphere, the topological disk and the torus.

2.5 Order on the sphere

The two-dimensional sphere $\mathbb{S}^2$ is the simplest example of curved surface. A sphere of radius R centered at the origin of a three-dimensional Cartesian frame can be parametrized in the standard form:

$$\begin{cases} x = R\sin\theta\cos\phi \\ y = R\sin\theta\sin\phi \\ z = R\cos\theta \end{cases}, \tag{2.58}$$

where $\theta \in [0, \pi]$ and $\phi \in [0, \phi)$. The coefficient of the metric tensor are given by:

$$g_{\theta\theta} = R^2\,, \qquad g_{\theta\phi} = 0\,, \qquad g_{\phi\phi} = R^2\sin^2\theta\,.$$

Both mean and Gaussian curvature are constant and equal to $K = H^2 = R^{-2}$. Because its exceptional simplicity and, at the same time, its ubiquitous presence in natural systems, the 2-sphere has played a special role in the study of geometrical frustration and represented historically the natural play-ground for the development of most of our knowledge of order in curved space. With no intention of being exhaustive, we review in this section some of the most fundamental concepts of crystalline and orientational order on the sphere, mostly to give a practical example of the ideas and mathematical tools previously described in this chapter.

Orientational order on the sphere was initially investigated by MacKintosh, Lubensky [74] and Prost [58] in the context of smectic vesicles. As we mention in §1.2.1, the L_β phase of phospholipidic membranes is characterized by the fact that the director $\boldsymbol{N}$, specifying the average direction of the hydrocarbon tails, is parallel to the unit normal $\boldsymbol{n}$ to the membrane. At lower temperatures, membranes can undergo a transition into the L'_β phase, in which molecules tilt relative to the surface normal, or the hexatic phase, in which the directions between neighboring molecules form a six-fold rotationally invariant director field with quasi long-range correlation. Both these liquid crystalline phases can be suitably described by a $p-$atic free energy of

the form (2.50) in which the director $\boldsymbol{m}$ plays the role of the normalized projection of the molecular axis $\boldsymbol{N}$ on the tangent plane of the vesicle:

$$\boldsymbol{m} = \frac{\boldsymbol{N} - (\boldsymbol{n}\cdot\boldsymbol{N})\boldsymbol{n}}{|\boldsymbol{N} - (\boldsymbol{n}\cdot\boldsymbol{N})\boldsymbol{n}|}\,, \tag{2.59}$$

in the case of L'_β vesicles, or a hexatic director field. Thus L'_β and hexatic vesicles can be described as $p-$atic phases with $p = 1$ and $p = 6$ respectively. Nematic shells (i.e. $p = 2$) have also drawn considerable attention recently [59, 75, 76]. Nematic spheres might be made by coating a droplet with gemini lipids, ABA triblock copolymers or nanorods. Microfluidic techniques for creating a thin spherical shell of liquid crystal in a double emulsion have been explored in [77].

As prescribed by Eq. (2.3) the total topological charge of a $p-$atic director field on the sphere is given by $Q = 2p$. Furthermore the energy of an isolated disclination, both on flat and curved surfaces, is proportional to the square of its topological charge. It is, therefore, always favorable to form disclinations with the lowest possible topological charge: $q = \pm 1$. In addition, like-sign disclinations repel each other. These considerations imply that the ground state of a $p-$atic phase on a sphere will likely have $2p$ maximally separated disclinations of topological charge $q = 1$ or winding number $k = q/p$. For $p = 1$, there will be a source and a sink at the north and south pole (see Fig. 2.1 center). For $p = 2$ one expects four $k = 1/2$ disclinations at the vertices of a tetrahedron. In the case of hexatics ($p = 6$) the most suitable candidate configuration for the ground state will feature twelve $k = 1/6$ disclinations at the vertices of a icosahedron.

The elastic energy (2.50) corresponding to these symmetric configurations of a spherical veiscle with $p-$atic order, was calculated by Lubensky and Prost with the result:

$$F_{el} = 2\pi K_A \left[\frac{1}{p}\log\left(\frac{2R}{r_c}\right) - f_p\right]\,, \tag{2.60}$$

with r_c the core radius and f_p a number given by:

$$f_p = 1 + \frac{1}{2p^2}\sum_{i\neq j}\log(\sin\beta_{ij})\,, \tag{2.61}$$

where β_{ij} is the distance between the ith and jth disclination and the sum is carried over all the defects.

Experimental realizations of spherical crystals, on the other hand, are found in colloidosomes (see §1.2.2), viral capsids (see §1.2.3) or the C_{60} Buckmister fullerene. Historically, the first attempt of understanding the structure of a spherical crystal consisting of V point-like particles interacting with a Coulomb potential on the surface of a unit sphere, was performed in 1904 by J. J. Thomson as part of the development of the plum pudding model of the atom [78] and is now considered a classic and still unsolved problem of mathematical physics [79, 80]. An almost literal realization of the Thomson problem is provided by multi-electron bubbles [81, 82]. Electrons trapped on the surface of liquid helium have long been used to investigate two dimensional melting [83, 84]. Multi-electron bubbles result when a large number of electrons (10^5-10^7) at the helium interface subduct in response to an increase in the anode potential and coat the inside wall of a helium vapor sphere of radius $10-100\mu$m. Typical electron spacings, both at the interface and on the sphere, are of order 2000 Å, so the physics is entirely classical, in contrast to the quantum problem of electron shells which originally motivated Thomson. Information about electron configurations on these bubbles can, in principle, be inferred from studying capillary wave excitations [85, 86]. Similar electron configurations should arise on the surface of liquid metal drops confined in Paul traps [87].

As already mentioned, at least twelve 5−fold coordinated vertices are topologically required in any triangulation of the sphere. Using the same argument outlined for $p-$atics, one might expect these twelve $+1$ disclinations to be arranged approximately at the vertices of a regular icosahedron. Spherical lattices with icosahedral symmetry (i.e. icosadeltahedral lattices) have been originally investigated and classified by Caspar and Klug in a classic paper of 1962 [38] (see Fig. 2.1 right). According to the Caspar-Klug (CK) construction, triangular lattices on the sphere with an icosahedral defect pattern are classified by a pair of integers (n, m) which specify the distance

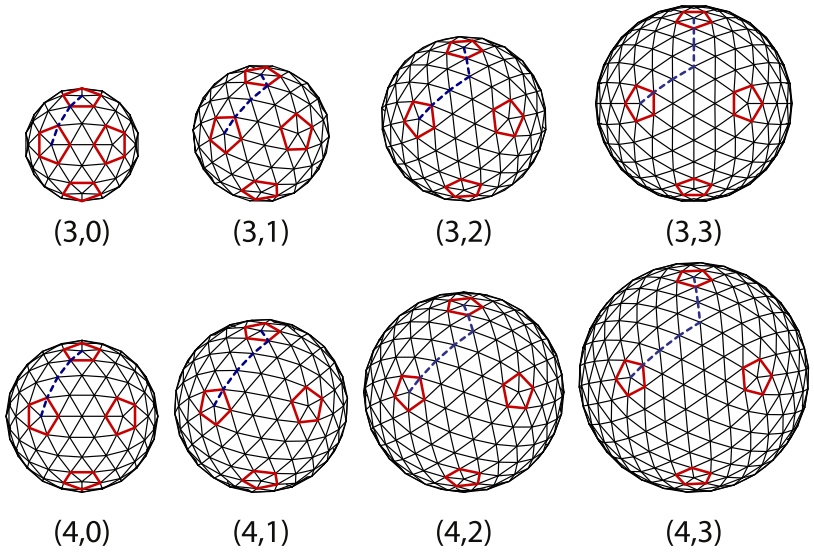

Figure 2.5: Example of (n, m) icosadeltahedra triangulations of the sphere. 5−fold coordinated vertices are circled in red and the path between neighboring disclinations is marked by a blue dashed line. From [93].

between neighboring disclinations in units of the lattice spacing a. The path from one disclination to a neighboring disclination for an (n, m) icosadeltahedral lattice consists of n straight steps, a subsequent 60° turn, and m final straight steps. The geodesic distance between nearest neighbor disclinations on a sphere of radius R is $d = R\cos^{-1}(1/\sqrt{5})$. The total number of vertices V on the sphere described by this (n, m)-lattice is given by:

$$V = 10(n^2 + m^2 + nm) + 2 \ . \tag{2.62}$$

In the case of the Thomson problem, such (n, m) configurations are believed to be ground states for relatively small numbers ($V \leq 300$, say) of particles interacting through a Coulomb potential [88–92].

The ground state structure of a spherical crystal was studied by Bowick, Nelson and Travesset by mean of the elastic free energy (2.55). For the case of the sphere,

Eq. (2.55) can be recasted in the form:

$$F = \frac{\pi}{36} Y R^2 \sum_{i,j}^{1,N} q_i q_j \chi(\beta_{ij}) + \epsilon_c \sum_{i=1}^{N} q_i^2 \,, \tag{2.63}$$

where N is the number of disclinations and

$$\chi(\beta_{ij}) = 1 + \int_0^{(1-\cos\beta_{ij})/2} dz \, \frac{\log z}{1-z} \,, \tag{2.64}$$

with β_{ij} the angular distance between two disclinations at the points (θ_i, ϕ_i) and (θ_j, ϕ_j) and is such that:

$$\cos\beta_{ij} = \cos\theta_i \cos\theta_j + \sin\theta_i \sin\theta_j \cos(\phi_i - \phi_j) \,. \tag{2.65}$$

A plot of the function χ is shown in Fig. For large core energies (i.e. small particle number) defects proliferation is generally expensive and one can assume the crystal to contain only the smallest number of defects compatible with the topology of the sphere, namely twelve. In this case the energy in Eq. (2.63) is minimized when the twelve $+1$ disclinations are located at the vertices of a regular icosahedron. The elastic energy of such icosahedral configuration is given by:

$$F = 0.604 \left(\frac{\pi}{36} R^2 Y \right) + 12\epsilon_c \,. \tag{2.66}$$

When the density of the system is increased icosahedral lattice becomes unstable and additional defects develop from the initially isolated $5-$fold disclinations to lower the elastic energy. Since the total topological charge must be constant, new defects generally appear in the form of one or more $5-7$ dislocation (of zero total topological charge) bound to the original $5-$fold dislocations, which therefore serve as a "seed" for the proliferation and growth of more complex defective structures. The number of excess dislocations radiating from a single seed disclination increases with the number of vertices V (see later). At the onset of such a structural transition each seed disclination is bound to a single dislocation, or in other words each isolated $5-$fold disclination is replace by a $5-7-5$ disclination array. These one-dimensional

defect clusters have been named "scars" by Bowick *et al.* [72, 94–96] and represent now a hallmark of spherical crystallography.

Scars in spherical non-Euclidean crystals are closely related to grain boundaries in traditional planar systems. Unlike grain boundaries, however, scars generally terminate terminate within the system. This property is due to the fact that local crystallographic directions rotate when parallel transported on a curved surface. In planar systems, on the other hand, crystallographic directions are fixed within a grain. Thus, if somewhere in the system two adjacent regions (grains) have non-parallel crystallographic directions, such a mismatch will necessarily propagate throughout the system causing a grain boundary line that spans the entire length of the crystal. On a curved surface, on the other hand, crystallographic directions rotate when parallel transported along a line and the mismatch is eventually adjusted.

The proliferation of scars in dense non-Euclidean crystals can be understood in the following way. In §2.4 we explained how the strain field generated by an isolated disclination is compensated by a non-zero Gaussian curvature in the underlying substrate and viceversa. In dense lattices, however, the region of space surrounding a defect becomes nearly flat at the length scale of a lattice spacing and the mutual screening between the strain introduced by a defect and that associated with the curvature decreases with a consequent growth in the elastic energy. A mechanism to restore an optimal screening is then to delocalize the topological charge of a disclination on a larger portion of space, thus replacing an isolated disclination with a one-dimensional defect cluster having the same net topological charge: a scar. On a surface with constant positive Gaussian curvature, the appearance of scars obviously occurs simultaneously at the location of each seed disclination once a critical density is reached. Such a critical density can be estimated by comparing the elastic energy (2.66) with that of a configuration obtained by replacing every seed disclination with a $5-7-5$ scar. Such a comparison yields to $(a/R)_{\text{critical}} \sim 0.2$ corresponding to $V = 305$ vertices on a unit sphere [72].

As we mentioned, the number of excess dislocation N_d within a same scar increases with the number of vertices V in the lattice. The relation between n_d and V can be determined using the following simple argument [97, 98]. Consider the region surrounding one of the twelve disclinations, with deficit angle $s = 2\pi/6$, centered on the north pole. As discussed in Ref. [72], we expect the stresses and strains at a fixed geodesic distance r from the pole on a sphere of radius R to be controlled by an *effective* disclination charge

$$\begin{aligned} s_{\mathit{eff}}(r) &= s - \int_0^{2\pi} d\phi \int_0^r dr' \sqrt{g}\, K \\ &= \frac{\pi}{3} - 4\pi \sin^2\left(\frac{r}{2R}\right) . \end{aligned} \tag{2.67}$$

Here the Gaussian curvature is $K = 1/R^2$ and the metric tensor associated with spherical polar coordinates (r, ϕ), with distance element $ds^2 = d^2r + R^2 \sin^2(r/R) d^2\phi$, gives $\sqrt{g} = R \sin(r/R)$. Suppose m grain boundaries radiate from the disclination at the north pole. Then, in an approximation which neglects interactions between the individual arms, the spacing between the dislocations in these grains is [72]

$$l(r) = \frac{am}{s_{\mathit{eff}}(r)} , \tag{2.68}$$

which implies an effective dislocation density

$$n_d(r) = \frac{1}{l(r)} = \frac{1}{ma}\left[\frac{\pi}{3} - 4\pi \sin^2\left(\frac{r}{2R}\right)\right] = \frac{2\pi}{ma}\left[\cos\left(\frac{r}{R}\right) - \frac{5}{6}\right] . \tag{2.69}$$

This density vanishes when $r \to r_c$, where

$$r_c = R \arccos\left(\frac{5}{6}\right) \approx 33.56^\circ R , \tag{2.70}$$

which is the distance at which the m grain boundaries terminate. The total number

of dislocations residing within this radius is thus

$$\begin{aligned} N_d &= m \int_0^{r_c} dr\, n_d(r) \\ &= \frac{\pi}{3a} r_c - \frac{4\pi}{a} \int_0^{r_c} dr\, \sin^2\left(\frac{r}{2R}\right) \\ &= \frac{\pi}{3}\left[\sqrt{11} - 5\arccos\left(\frac{5}{6}\right)\right]\left(\frac{R}{a}\right) \\ &\approx 0.408\left(\frac{R}{a}\right) . \end{aligned} \tag{2.71}$$

The simple geometrical argument outlined above predicts a linear dependence between the number of excess dislocations per scar and the ratio R/a between the radius of the sphere and the lattice spacing a, with angular coefficient approximately equal to 0.41. Such a prediction has been brilliantly confirmed by Bausch *et al.* in a beautiful experiment of 2003 [95]. In this experiment spherical crystals were obtained from the self-assembly of 1-μm-diameter cross-linked polystyrene beads adsorbed on the surface of spherical water droplets, themselves suspended in a density-matched toluene-chlorobenzene mixture (20). By changing the radius of the water droplet as well as the number of polystyrene beads on the surface, the authors of Ref. [95] imaged the formation of scars and counted the number of excess dislocations per scar (see Fig.) finding $N_d \sim 0.41\, R/a$.

Chapter 3

Crystalline order on surfaces with variable Gaussian curvature and boundary

3.1 Introduction

Under specific experimental conditions amphiphilic molecules in solution, such as lipids or amphiphilic block copolymers self-assemble in a spectacular variety of shapes including spherical and cylindrical micelles, vesicles and lamellae, together with more complex geometries such as uni- and multilamellar vesicles, onion vesicles, toroidal and cage-shaped micelles. The exact shape and size of these structures has been observed to depend on both molecular (i.e. molecular size, hydrophilic/hydrophobic ratio, molecular stiffness) and collective parameters such as the concentration or the ability of the molecules to diffuse through the solvent.

As noted previously, amphiphilic membranes can exist in different thermodynamic states according to the amount of orientational and positional order or their molecular constituents. The L'_β and P_β phases, which occur in lipid membranes featuring the phosphatidylcholine (PC) group, have been found, in particular, to exhibit in-plane

orientational correlations extending over 200 Å, one order of magnitude larger than the typical spacing between PC groups [24, 99]. Because of thermal fluctuations, such membranes generally appear in a corrugated conformation with non-constant Gaussian and mean curvature. Furthermore it is likely for lipid membranes to have pores providing a passage from the exterior to the interior of a vesicle. It is therefore natural to ask how variable Gaussian curvature and the presence of one or more boundaries affects the phenomenology reviewed in the previous section in the case of the sphere.

In this chapter we discuss crystalline order in two important cases of surfaces with variable Gaussian curvature and (possibly) boundary, namely the bumpy surface that is obtained by revolving the graph of a Gaussian function around its symmetry axis (i.e. a *Gaussian bump*) and the paraboloid of revolution. The former can be thought as a gentle deformation of a plane and thus can serve as a playground to analyze the onset of behavior not occurring in planar systems; the latter is possibly the simplest two-dimensional Riemannian surface having variable Gaussian curvature and boundary and provides a setting that is simple enough to carry out a full analytical treatment and analyze also large curvature regimes. Furthermore, since paraboloidal shapes naturally occur across the air/liquid interface of a fluid placed in a rotating cylindrical vessel, a direct physical realization of paraboloidal crystals can be constructed by assembling monodisperse objects on the surface of a rotating liquid. In §3.5 we review a simple experiment done in cooperation with H. Shin and C. Thomas [100] in which such a macroscopic model for a paraboloidal crystal is constructed by assembling a two-dimensional soap bubble "raft" on the air/liquid interface of a water-soap solution, thus extending the classic work of Bragg and Nye on planar bubble rafts. Purely orientational order on the Gaussian bump has been recently reviewed by Turner *et al* [63] and won't be discussed here.

3.2 Surfaces of revolution and conformal mapping

Before analyzing the ground state structure of a crystalline paraboloid and Gaussian bump, it is useful to refresh some general concepts in the geometry of surfaces of revolution. The notion of conformal mapping of Riemannian surfaces will be also frequently employed in the following and will be briefly reviewed in this section with special attention on its application to the calculation of Green functions on simply connected 2−manifolds.

A surface of revolution M is a surface obtained by revolving a two-dimensional curve around an axis. The resulting surface therefore always has azimuthal symmetry. The standard parametrization of a surface of revolution is:

$$\begin{cases} x = \xi(r)\cos\phi \\ y = \xi(r)\sin\phi \\ z = \eta(r) \end{cases} \tag{3.1}$$

where $r \in [0, R]$ (with R possibly infinite) and $\phi = [0, 2\pi)$. The metric of the surface (3.1) is given by:

$$ds^2 = [(\xi')^2 + (\eta')^2]dr^2 + \xi^2 d\phi^2\,, \tag{3.2}$$

where the prime indicate a partial derivative with respect to r. The Gaussian curvature is a function of r only and is given by:

$$K = \frac{\eta'(\xi'\eta'' - \xi''\eta')}{\xi(\xi'^2 + \eta'^2)^2} \tag{3.3}$$

In the presence of a boundary ∂M the condition (2.2) for the total topological charge of any triangulation on M reads:

$$Q = \sum_{i=1}^{V_{\partial M}}(4 - c_i) + \sum_{i=1}^{V_M}(6 - c_i) = 6\chi \tag{3.4}$$

where $V_{\partial M}$ and V_M are the number of vertices on the boundary and the interior of the manifold respectively (with $V = V_{\partial M} + V_M$ the total number of vertices). $q_{i,\partial M} = 4 - c_i$

is the topological charge of a vertex of coordination number c_i located on the boundary, where the coordination number of a perfect triangular lattice is four rather than six. A surface of revolution with boundary $\partial M = \{r = R\} \times [0, 2\pi]$ is homeomorphic to a disk ($g = 0$ and $h = 1$) and has therefore $\chi = 1$ and total topological charge $Q = 6$. Such a topological requirement can be fulfilled for instance by placing six isolated 3−fold disclinations along the boundary and keeping the interior of the surface defect-free or, on the other hand, by placing a 5−fold disclination in the interior and the remaining five 3−fold disclinations along the boundary.

Let us consider now a generic Riemannian surface M and two curves on S intersecting at some point $\boldsymbol{x}_0$. The angle between the two intersecting curves is, by definition, the angle between the tangents to these curves at $\boldsymbol{x}_0$. A mapping of a portion S of a surface onto a portion S^* is called *conformal* (or angle-preserving) if the angle of intersection of every arbitrary pair of intersecting arcs on S^* is the same as that of the corresponding inverse images on S at the corresponding point (see for example [101]). It is not difficult to prove that a mapping from a portion S of a surface onto a portion S^* is conformal if and only if, when on S and S^* the same coordinate systems have been introduced, the coefficients g^*_{ij} and g_{ij} of the metric tensor of S^* and S are related by:

$$g^*_{ij} = w(\boldsymbol{x}) g_{ij} \,, \tag{3.5}$$

with w a positive function of the coordinates $\boldsymbol{x} = (x^1, x^2)$. Eq. (3.5) implies indeed that the angle between any pair of intersecting curves is the same in S^* and S. *Isometries* are a special case of conformal mappings where $w = 1$ and the mapping is both distance and angle-preserving.

A special type of conformal mapping is that of a portion S of a surface into a plane. This may be accomplished by introducing a set of coordinates $\boldsymbol{u} = (u^1, u^2)$ such that:

$$ds^2 = w(\boldsymbol{u})[(du^1)^2 + (du^2)^2] \,. \tag{3.6}$$

Coordinates (u^1, u^2) satisfying Eq. (3.6) are called *isothermal* (or conformal). In general, any simply connected Riemannian manifold with a $C^\infty-$smooth metric ds^2 can be equipped with a set of local isothermal coordinates. This important result can be stated by saying that any simply connected Riemannian manifold is locally conformally equivalent to a planar domain in two-dimensions. In conformal coordinates, the Gaussian curvature reads:

$$K = -\frac{2\Delta[\log w(\boldsymbol{u})]}{w(\boldsymbol{u})} \tag{3.7}$$

Conformal mapping is the fundamental tool behind the celebrated uniformization theorem according to which, *every simply connected Riemannian surface is conformally equivalent to the unit disk, the complex plane or the Riemann sphere*. This theorem, first proved by Koebe and Poincaré independently in 1907, extends the Riemann mapping theorem for simply connected domains in the complex plane to all simply connected Riemannian surfaces and provides an insightful classification scheme. Its formidable power lies in the fact that the mapping that allows one to transform a generic surface into a simpler "irreducible" one is not an arbitrary homeomorphism but is conformal, and thus preserves part of the geometrical structure of the original manifold. In the following we will see how this feature has important consequences in the elastic theory of defects on curved surfaces. The uniformization of Riemannian surfaces is historically the first example of geometrization. In the case of manifolds of higher Hausdorff dimension, and 3-manifolds in particular, the latter program has become, following Thurston, one of the most challenging and fascinating chapters of modern geometry.

A bounded Gaussian bump and a paraboloid of revolution are both conformally equivalent to the unit disk $\mathbb{D}$ of the complex plane. Calling $z = \varrho e^{i\phi}$, the new metric will be:

$$ds^2 = w(z)(d\varrho^2 + \varrho^2 d\phi^2) \tag{3.8}$$

The conformal factor w can be found by equating the metrics (3.2) and (3.8). This

yields:

$$w(\rho) = \left[\frac{\xi(r)}{\varrho}\right]^2 \tag{3.9}$$

with ϱ and r related by the differential equation:

$$\frac{d\varrho}{dr} \pm \sqrt{\frac{(\xi')^2 + (\eta')^2}{\xi^2}}\, \varrho = 0 \tag{3.10}$$

whose solution is given by:

$$\varrho = \exp\left\{ \pm \int dr \sqrt{\frac{(\xi')^2 + (\eta')^2}{\xi^2}} \right\} \tag{3.11}$$

The sign of the exponent and the integration constant in Eq. (3.11) can be tuned to obtain the desired scale and direction of the conformal map.

The calculation of the Green function of the Laplace and biharmonic operator is considerably simplified once a surface of revolution has been endowed with a local system of isothermal coordinates. In this case it is easy to show the Laplace-Beltrami operator Δ_g takes the form:

$$\Delta_g = w^{-1}\Delta \tag{3.12}$$

where Δ is now the Laplacian in the Euclidean metric tensor:

$$\gamma_{\varrho\varrho} = 1, \qquad \gamma_{\varrho\phi} = 0, \qquad \gamma_{\phi\phi} = \varrho^2, \tag{3.13}$$

with determinant γ. Since the determinant of the metric tensor undergoes the transformation $\sqrt{g} \to w\sqrt{\gamma}$ under conformal mapping, the Laplace and biharmonic equation for the Green function become:

$$\Delta G_L(z,\zeta) = \delta(z,\zeta) \tag{3.14a}$$

$$\Delta w^{-1} \Delta G_{2L}(z,\zeta) = \delta(z,\zeta) \tag{3.14b}$$

where $\delta(z,\zeta)$ is the standard delta function at the point $z = \zeta$ of the unit disk. Eq. (3.14a) is now the standard Laplace-Green equation. Its associated Dirichlet problem has the familiar solution:

$$G_L(z,\zeta) = \frac{1}{2\pi} \log \left| \frac{z-\zeta}{1 - z\bar{\zeta}} \right| \tag{3.15}$$

Eq. (3.14b) is known as the *weighted* biharmonic Green equation. The uniqueness of its solution requires imposing both Dirichlet and Neumann boundary conditions:

$$\begin{cases} G_{2L}(z,\zeta) = 0 & z \in \partial\mathbb{D} \\ \partial_{n(z)} G_{2L}(z,\zeta) = 0 & z \in \partial\mathbb{D} \end{cases} \tag{3.16}$$

where $\partial_{n(z)}$ denotes the derivative with respect to the variable z along the normal direction at $\partial\mathbb{D}$. Its solution can be expressed in integral form as:

$$G_{2L}(z,\zeta) = \int d\sigma^2\, G_L(z,\sigma)[G_L(\sigma,\zeta) - H(\sigma,\zeta)] \tag{3.17}$$

where $H(\sigma,\zeta)$ is a harmonic kernel that enforces the Neumann condition. Such a function depends on the form of the conformal weight w. For radial weights $w = w_0(|z|^2)$, such as those obtained by conformally mapping a surface of revolution, $H(\sigma,\zeta)$ has been calculated explicitly by Shimorin [102]:

$$H(\sigma,\zeta) = -2\int_{|\zeta|}^1 \frac{dt}{t}\int_0^{t^2} ds\, w_0(s) k\left(\frac{s}{t^2}\,\zeta\,\overline{\sigma}\right) \tag{3.18}$$

where:

$$k(z\,\overline{\zeta}) = \sum_{n\geq 0} \frac{(z\,\overline{\zeta})^n}{c_n} + \sum_{n<0} \frac{(\overline{z}\,\zeta)^{|n|}}{c_{|n|}} \tag{3.19}$$

and the coefficients c_n are given by:

$$c_n = 2\int_0^1 dt\, t^n w_0(t)\,. \tag{3.20}$$

3.3 Crystalline order on the Gaussian bump

The most natural way of introducing a non-vanishing Gaussian curvature on an initially flat medium is to gently deform the medium at one point in such a way that the curvature introduced by this deformation dies off at infinity. If the initial planar domain is the entire Euclidean plane $\mathbb{R}^2$, the Euler characteristic is zero and, independently of the value of the Gaussian curvature, an ordered phase embedded on it is not topologically required to contain defects. Such a construction is clearly

ideal to detect the onset of structural behavior not occurring in the ground state of a planar system such as the appearance of dislocations and disclinations. Vitelli *et al* [103, 104] analyzed crystalline and $p-$atic order on the bumpy surface obtained by revolving the graph of a Gaussian function about its symmetry axis. The resulting *Gaussian bump* has parametrization:

$$\begin{cases} x = r\cos\phi \\ y = r\sin\phi \\ z = h\exp\left(-\frac{r^2}{2r_0^2}\right) \end{cases} \tag{3.21}$$

with $r \in [0, R]$ and $\phi \in [0, 2\pi)$. In this parametrization the metric tensor g_{ij} (with determinant g) and the Gaussian curvature are given by:

$$g_{rr} = \ell(r), \qquad g_{r\phi} = 0, \qquad g_{\phi\phi} = r^2, \tag{3.22a}$$

$$K = \frac{\alpha^2 e^{-\frac{r^2}{r_0^2}}}{r_0^2\,\ell^2(r)}\left(1 - \frac{r^2}{r_0^2}\right), \tag{3.22b}$$

where $\alpha = h/r_0$ is the aspect ratio of the bump and $\ell(r)$ is given by:

$$\ell(r) = 1 + \frac{\alpha^2 r^2}{r_0^2}\, e^{-\frac{r^2}{r_0^2}} \tag{3.23}$$

It is an instructive exercise to verify that the Euler characteristic χ vanishes when the boundary radius R is set to infinity. Employing the Gauss-Bonnet theorem one has:

$$\chi = \int_0^R dr\,\sqrt{g}\,K + \frac{1}{2\pi}\oint_{C_R} ds\,\kappa_g \tag{3.24}$$

where κ_g, the geodesics curvature of the circular boundary C_R of radius R, is given by:

$$\kappa_g = \frac{1}{R\sqrt{\ell(R)}} \tag{3.25}$$

If the bump is unbounded the second term in Eq. (3.24) disappears and, on taking $R \to \infty$, one has:

$$\int_0^\infty dr\,\sqrt{g}\,K = 0$$

which implies $\chi = 0$. For finite values of R, on the other hand, the first integral in Eq. (3.24) gives:

$$\int_0^R dr\,\sqrt{g}\,K = 1 - \frac{1}{\sqrt{\ell(R)}}$$

so that the terms proportional to $1/\sqrt{\ell(R)}$ cancel each other, yielding $\chi = 1$. Because the infinite bump has $\chi = 0$ disclinations must appear in pairs and dislocations must have total Burgers vector zero:

$$\sum_i q_i = \sum_i \boldsymbol{b}_i = 0$$

Vitelli *et al* showed that topological defects appear in the ground state when the aspect ratio α exceeds a critical value α_c. Because of the topological constraint, defects appears initially in the form of a pair of unbound dislocations, roughly located in the region where $K = 0$. Upon increasing the aspect ratio, more dislocations appear. This mechanism clearly resembles the defect proliferation that occurs in two-dimensional melting and suggests an interpretation of the curvature as a local effective temperature.

At the onset of defect proliferation, inter-defect interactions are negligible with respect to the interactions with the "smeared out" topological charge associated with the curvature of the underlying medium. The dislocation unbinding mechanism is then described by a non-local function of the Gaussian curvature representing the defect-curvature interaction part of the elastic energy of Eq. (2.54):

$$F_{int} = Y \int d^2x\,\eta(\boldsymbol{x}) \int d^2y\,G_{2L}(\boldsymbol{x},\boldsymbol{y})K(\boldsymbol{y}) = Y \int d^2x\,\eta(\boldsymbol{x})\varphi(\boldsymbol{x})\,, \tag{3.26}$$

where F_{int} is the curvature-defect interaction part of the elastic energy and $\varphi(\boldsymbol{x})$ can be interpreted as a *geometric potential* associated with the Gaussian curvature of the embedding manifold:

$$\Delta^2\varphi(\boldsymbol{x}) = K(\boldsymbol{x})\,. \tag{3.27}$$

Thus

$$\varphi(\boldsymbol{x}) = \int d^2z\,d^2y\,G_L(\boldsymbol{x},\boldsymbol{y})[G_L(\boldsymbol{y},\boldsymbol{z})K(\boldsymbol{z}) + U(\boldsymbol{y})]\,, \tag{3.28}$$

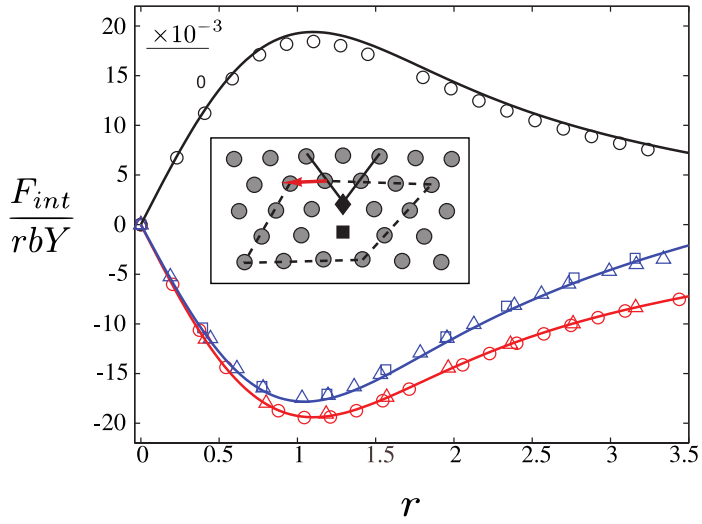

Figure 3.1: (Color online) Curvature-defect interaction energy of an isolated disclination for a Gaussian bump of aspect ratio $\alpha = 0.5$. Open symbols represent the data from a numerical minimization of a fixed connectivity harmonic model. The lower and upper branch are obtained from Eq. (3.30) by setting $\theta = \pm\pi/2$ and letting Λ equal 4 (blue curve) and 8 (red curve). [Courtesy of V. Vitelli, University of Pennsylvania, Philadelphia, PA].

where $U(\boldsymbol{y})$ is a harmonic function which enforces the boundary conditions. The Laplacian Green function has the form (3.15) with the conformal distance $\rho = |z|$ given here by:

$$\varrho = \frac{r}{R} \exp\left\{ -\int_r^R dr' \, \frac{\sqrt{\ell(r')} - 1}{r'} \right\} \tag{3.29}$$

For a single dislocation of Burgers vector $\boldsymbol{b}$, F_{int} has the form [103]:

$$F_{int} = \frac{1}{8} hb\alpha^2 Y \sin\phi \left(\frac{e^{-\lambda^2} - 1}{\lambda} + \frac{\lambda}{\Lambda^2} \right) , \tag{3.30}$$

where $\lambda = r/r_0$ and $\Lambda = R/r_0$. The first term in Eq. (3.30) corresponds to the $R \to \infty$ geometric potential, while the second is a finite size correction arising from a circular boundary of radius R. A plot of the function (3.30) is shown in Fig. 3.1. The profile of the function F_{int} can be elucidated by regarding a dislocation as bound pair of disclinations of opposite topological charge. Each one of the disclinations interacts with a potential of the form (3.27). For small r, positive (negative) disclinations

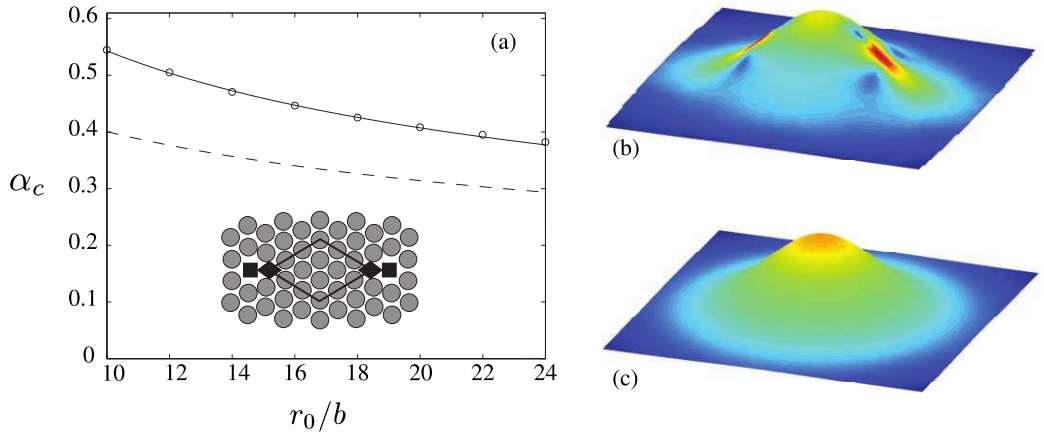

Figure 3.2: (Color online) Dislocation unbinding. (a) Critical aspect ratio α_c as a function of r_0/b. The theoretical estimate (3.31) is plotted versus r_0/b for core energies $E_d = 0$ (dashed line) and $E_c = 0.1B^2Y$ (solid line). Circles are obtained from a numerical minimization of a fixed connectivity harmonic model. On right the logarithm of the numerically calculated strain energy for a (c) defect-free configuration on a bump of $r_0 = 10b$ and $\alpha = 0.7 > \alpha_c$ and (d) the defective configuration shown in the inset. [Courtesy of V. Vitelli, University of Pennsylvania, Philadelphia, PA].

are attracted (repelled) by the center of the bump. As a consequence disclinations experience a force which increases linearly with r. Thus if the positive disclination in the dipole is closer to the top, it will experience a force that is opposite and slightly less than that acting on the negative disclination that is further away from the top. As a result an effective "tidal" force will push the dislocation downhill. For large r, however, the geometric potential saturates and the attractive force exerted on the positive disclination takes over and drags the dislocation toward the center of the bump. The minimum of the elastic energy corresponding to the equilibrium between these two competing forces is obtained for $\lambda \approx 1.1$. The origin of these forces is the Peach-Koehler force $f_k = \epsilon_{kj} b_i \sigma_{ij}$ acting on a dislocation of Burgers vector b_i in an external stress field σ_{ij}. In the case of a two-dimensional crystal on a substrate with preexisting Gaussian curvature, dislocations couple with the internal stress due to the curvature of the medium producing a similar effect.

Unbound dislocations occur in the ground state of a crystalline Gaussian bump

when the aspect ratio α exceeds a critical value. For nearly flat landscapes, indeed, the energetic cost of a pair of unbound dislocations is larger than that due to the distortion of the medium and the system is favoured to be defect free. Upon increasing the aspect ratio, however, the resulting elastic strain can be partially relieved by introducing a pair of dislocations with equal and opposite Burgers vector. The transition occurs when the energy gain from placing each dislocation in the minimum of the potential energy F_{int} outweights the total work needed to tear them apart plus the core energies $2E_d$. The resulting critical aspect ratio is given by:

$$\alpha_c^2 \approx \frac{b}{2r_0} \log\left(\frac{r_0}{b'}\right) , \tag{3.31}$$

where $b' = (b/2)e^{-8\pi E_c/(Yb^2)}$. Upon increasing the aspect ratio, the number of unbound dislocations increases and elementary $5-7$ dislocations start clustering in more complicated structures of zero net Burgers vector. Fig. 3.2 shows a plot of the critical aspect ratio α_c as the function of the dimensionless parameter r_0/b from Ref. [103], as well as density plots of the strain energy corresponding to a defect-free bump (c) and a configuration featuring two unbound dislocations (b).

The interaction between defects and curvature also has some remarkable stabilizing effects on defect dynamics. Dislocation dynamics consists of two distinct processes: glide and climb. The former is motion along the direction of the Burgers vector and it implies only local rearrangement of atoms and thus requires a very low activation energy which makes it dominant at low temperatures. The latter consists of motion in the direction perpendicular to the Burgers vector, it requires diffusion of vacancies and interstitials and is usually suppressed relative to glide. As a consequence of the underlying curvature, however, a gliding dislocation experiences a "recalling" force $f_{recall} \approx k_d|y|$, where y is the transverse displacement and k_d is a position-dependent effective spring constant. At leading order in y and α, the latter is given by:

$$k_d(r) = \frac{b\alpha^2 Y}{4r_0}\left[\frac{1-(1+\lambda^2)e^{-\lambda^2}}{\lambda^3}\right] . \tag{3.32}$$

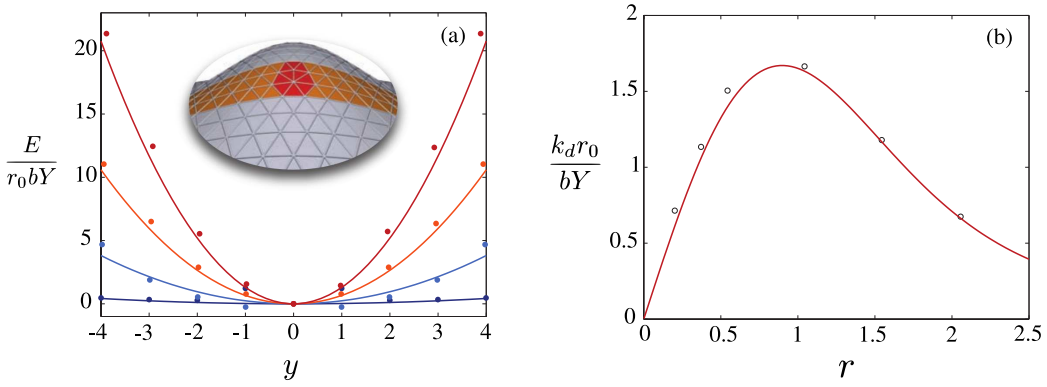

Figure 3.3: (Color online) Dislocation glide. (a) Recalling potential $\frac{1}{2}k_d y^2$ acting on dislocations gliding in the direction y (expressed in units of the lattice spacing a) for $r_0/a = 10$, $\lambda = 0.5$ (at $y = 0$), $\Lambda = 8$ and $\alpha = 0.1$ (dark blue), 0.3 (blue), 0.5 (orange) and 0.7 (red). The energy is scaled by 10^{-4}. Effective spring constant for $r_0 = 10a$ and $\alpha = 0.5$. The ordinate axis is scaled by 10^{-2}. Filled and empty circles represent numerical data obtained from a fixed connectivity harmonic model. [Courtesy of V. Vitelli, University of Pennsylvania, Philadelphia, PA].

This effective recaling force is not due to any external field nor to the interaction of dislocations with other defects, but exclusively to the coupling of the gliding dislocation with the curvature of the substrate. As expected the effective spring constant (3.32) vanishes for planar crystals (i.e. $\alpha \to 0$). Since Yb^2 can be hundreds of $k_B T$, at finite temperature the harmonic potential $\frac{1}{2}k_d y^2$ associated with the recalling force raises the activation energy of thermally induced dislocation glide. The harmonic recalling potential and the effective spring constant (3.32) are ploted in Fig. 3.3, together with numerical data obtained from a fixed connectivity harmonic model [103].

Spatial curvature also provides an effective potential in the thermal diffusion of interstitials and vacancies. These can be constructed by grouping three dislocation dipoles. The elastic energy associated with a single interstitial/vacancy can be derived from Eq. (3.26) in the form

$$F_{int}(\boldsymbol{x}) \approx \frac{1}{2} Y \Omega V(\boldsymbol{x}) \,, \tag{3.33}$$

where $V = \Delta\varphi$ and Ω is the area excess or deficit associated with the defects. As a

result, interstitials tend to climb to the top of the bump while vacancies are pushed into the flat regions. Like a disclination of positive topological charge, an interstitial is attracted to regions of positive Gaussian curvature while a vacancy is attracted to regions of negative Gaussian curvature.

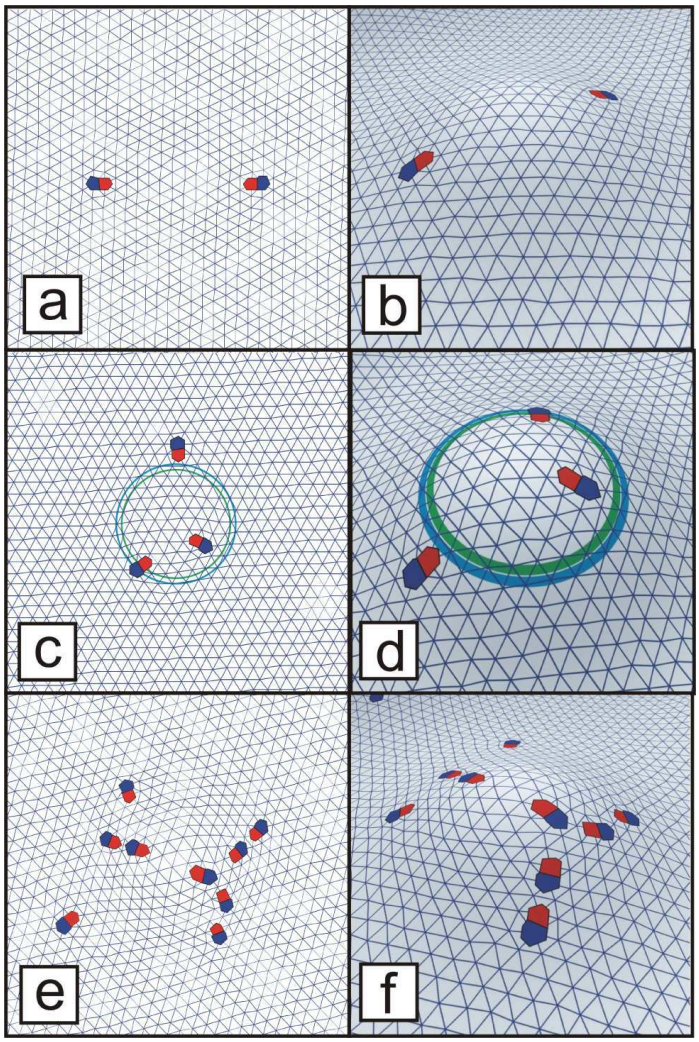

Figure 3.4: (Color online) Delaunay triangulation of 780 particles on a Gaussian bump. (a) and (b) Top view of the lattice containing two dislocations of opposite Burgers vector on a bump of aspect ratio $\alpha = 0.82$. (c) and (d) Three dislocations arranged around a bump of aspect ratio $\alpha = 0.95$. (e) and (f) A more complex arrangements of dislocations on a bump of aspect ratio $\alpha = 1.58$. [Courtesy of Alexander Hexemer, UC Santa Barbara, Santa Barbara, CA. Currently at Lawrence Berkeley National Lab., Berkeley, CA].

The crystalline structure arising on a Gaussian bump has been investigated numerically by Hexemer *et al* [105]. By means of smart Monte Carlo (SMC) simulations, the authors analyzed the ground state configuration of a system of N point-like particles (with N up to 780) interacting on a Gaussian bump of variable aspect ratio with a Yukawa potential of the form $U(r) = \exp(-\kappa r)/r$ with r the Euclidean distance between two particles in $\mathbb{R}^3$. In the first approximation such a potential describes the interaction between charged particles in solution with counter-ions and κ^{-1} is the Deybe-Hückel screening length. Starting from an initially defect-free lattice and relaxing it with order 10^5 SMC iterations, Hexemer *et al* observed the appearance of defects for increasing aspect ratio. Fig. 3.4 shows the arrangement of 780 particles for increasing aspect ratios. As predicted by the elastic theory, the proliferation of defects starts with the appearance of a pair of isolated dislocations (Figs. 3.4a and b). They are sitting at $\lambda = 1.46$ from the center and are rotated by 180°, giving rise to a configuration with total Burgers vector close to zero. Upon increasing the aspect ratio, a third dislocation is observed (Fig. 3.4c and d). The three dislocations are rotated by 120° with respect to each other. The green and blue circles in Fig. 3.4c and d mark the region of zero Gaussian curvature and the minimum of the geometric potential at $1.1\, r_0$. As shown in the figure, for $\alpha = 0.95$ two of the three dislocation are not sitting at $1.1\, r_0$ as one might expect. One is deep inside the area of positive Gaussian curvature while the other is in the region of negative Gaussian curvature. Hexemer *et al* excluded this discrepancy was due to a misconvergence of the algorithm and argued it is to be attributed to the finite size of the system.

Fig. 3.4e and f show the lowest energy state on a bump of aspect ratio $\alpha = 1.58$. In this situation dislocations appear arranged in the form of grain boundaries. This phenomenon has a simple interpretation. The total elastic energy of a collection of defects on a curved surface consists of three parts: the curvature-defect interaction discussed above, that tends to localize the defects where the geometric potential is minimal, a defect-defect interaction which is repulsive for like-sign defects and attrac-

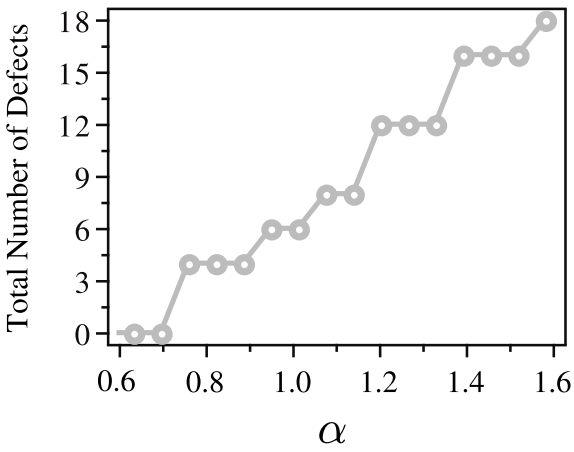

Figure 3.5: Total number of disclinations in the ground state as a function of the aspect ratio α. [Courtesy of Alexander Hexemer, UC Santa Barbara, Santa Barbara, CA. Currently at Lawrence Berkeley National Lab., Berkeley, CA].

tive for defects of opposite sign and an additional contribution due to the curvature alone. For a small number of dislocations, inter-defect interactions are negligible if compared with curvature-defect interactions and dislocations tend to gather where F_{int} is minimal. As shown from the data in Fig. 3.5, however, the total number of dislocations in the bump is linearly proportional to the aspect ratio. When the total number of dislocations on the bump exceeds some threshold value the repulsive interaction takes over and dislocations start spreading. Dislocations with parallel (antiparallel) Burgers vector are organized in such a way as to maximize (minimize) their reciprocal distance while still taking advantage of the Gaussian curvature screening. The final result of this competition are the $Y-$shaped grain boundaries shown in Fig. 3.4. The branching allows the dislocations to lower their potential energy by keeping a large number of dislocations close to the $1.1\, r_0$ circle.

3.4 Paraboloidal crystals

3.4.1 Elastic energy of disclinations on the paraboloid

A paraboloid of revolution is possibly the simplest surface with both variable Gaussian curvature and boundary. Its standard parametrization is given by:

$$\begin{cases} x = r\cos\phi \\ y = r\sin\phi \\ z = \frac{h}{R^2}\, r^2 \end{cases} \tag{3.34}$$

with $r \in [0, R]$ and $\phi = [0, 2\pi]$. Here h is the height of the paraboloid and R the maximum radius. In the following we will call $\kappa = 2h/R^2$ the normal curvature of the paraboloid at the origin. The metric tensor g_{ij} and the Gaussian curvature are given respectively by:

$$g_{rr} = 1 + \kappa^2 r^2, \qquad g_{r\phi} = 0, \qquad g_{\phi\phi} = r^2\,, \tag{3.35a}$$

$$K = \frac{\kappa^2}{(1+\kappa^2 r^2)^2} \tag{3.35b}$$

The problem of finding the optimal arrangement of disclinations in the ground state of paraboloidal crystals has been considered by the authors of this review article [106, 107]. As in the case of a Gaussian bump, when the maximal Gaussian curvature exceeds some critical value (depending on κ and R) defects proliferate in an initially defect-free configuration. Unlike the Gaussian bump, however, the Gaussian curvature on a paraboloid is strictly positive and only vanishes at infinity. Positive isolated disclinations are thus energetically preferred to dislocation dipoles and the defect proliferation mechanism consists of a "migration" of one of the six topologically required +1-disclinations from the boundary to the origin of the paraboloid. Dislocations, on the other hand, appear in the system clustered in the form of grain boundary scars in the high density regime as in spherical crystals. Since the Gaussian curvature is not constant throughout the manifold, however, this transition is preceded by a regime in which isolated disclinations and scars coexist in the crystal.

Let $\rho(\boldsymbol{x})$ be the effective topological charge density of a system of N disclinations on a background of Gaussian curvature $K(\boldsymbol{x})$:

$$\rho(\boldsymbol{x}) = \frac{\pi}{3}\sum_{i=1}^{N} q_i \delta(\boldsymbol{x}, \boldsymbol{x}_i) - K(\boldsymbol{x}) \tag{3.36}$$

If free boundary conditions are choosen, the elastic energy (2.55) can be written as:

$$F_{el} = \frac{1}{2Y}\int d^2x\, \Gamma^2(\boldsymbol{x}) \tag{3.37}$$

where $\Gamma(\boldsymbol{x}) = \Delta\chi(\boldsymbol{x})$, and $\chi(\boldsymbol{x})$ satisfies the inhomogeneous biharmonic equation:

$$\Delta^2\chi(\boldsymbol{x}) = Y\rho(\boldsymbol{x}) \tag{3.38}$$

with boundary conditions:

$$\begin{cases} \chi(\boldsymbol{x}) = 0 & \boldsymbol{x} \in \partial M \\ \nu^i \nabla_i \chi(\boldsymbol{x}) & \boldsymbol{x} \in \partial M \end{cases} \tag{3.39}$$

where ν^i is the ith component of the tangent vector ν perpendicular to the boundary. In the parametrization (3.34), the normal vector $\boldsymbol{\nu}$ is simply given by $\boldsymbol{g}_r/|\boldsymbol{g}_r|$ with $\boldsymbol{g}_r$ the basis vector associated with the coordinate r. The stress function $\Gamma(\boldsymbol{x})$ can thus be expressed as:

$$\frac{\Gamma(\boldsymbol{x})}{Y} = \int d^2y\, G_L(\boldsymbol{x}, \boldsymbol{y})\rho(\boldsymbol{y}) + U(\boldsymbol{x})\,. \tag{3.40}$$

$G_L(\boldsymbol{x}, \boldsymbol{y})$ is given in (3.15) and $U(\boldsymbol{x})$ is a harmonic function on the paraboloid that enforces the Neumann boundary conditions in Eq. (3.39). The conformal distance on the paraboloid is given by:

$$\varrho(r) = \lambda \frac{r e^{\sqrt{1+\kappa^2 r^2}}}{1+\sqrt{1+\kappa^2 r^2}}\,. \tag{3.41}$$

with λ a scale factor which ensures that $\varrho(R) = 1$. The Green's function $G_L(\boldsymbol{x}, \boldsymbol{y})$, and hence the entire elastic free energy, depends only on the coefficients of the first fundamental form of the surface (i.e. the metric tensor g_{ij}). Thus the elastic energy associated with the defect interactions and thus the crystalline order is an *intrinsic*

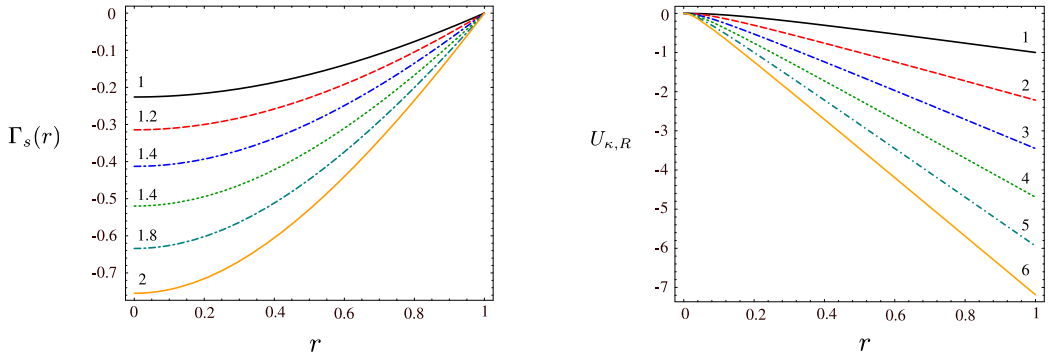

Figure 3.6: (Color online) The function $\Gamma_s(r)$ and $U_{\kappa,R}$ for different values of κ.

property of the manifold and so is invariant under local isometries. This observation, which might appear obvious in the case of isometric surfaces such the Euclidean plane and the cylinder, is quite remarkable when applied to more sophisticated isometric manifolds such as the catenoid and the helicoid or Scherk surfaces.

Using Eq. (3.41) and (3.15) in Eq. (3.37), the elastic energy F_{el} of a collection of N disclinations in a paraboloidal crystal can be expressed as:

$$\frac{\Gamma(\boldsymbol{x})}{Y} = \frac{\pi}{3}\sum_{i=1}^{N} q_i G_L(\boldsymbol{x},\boldsymbol{x}_i) - \Gamma_s(|\boldsymbol{x}|) + U(\boldsymbol{x})\,, \tag{3.42}$$

where the first term represents the bare contribution of the defects to the energy density and the second corresponds to the screening effect of the Gaussian curvature. Explicitly:

$$\Gamma_s(|\boldsymbol{x}|) = \log\left(\frac{\alpha e^{\sqrt{1+\kappa^2 r^2}}}{1+\sqrt{1+\kappa^2 r^2}}\right), \tag{3.43}$$

where $r = |\boldsymbol{x}|$ and

$$\alpha = \frac{1+\sqrt{1+\kappa^2 R^2}}{\exp\left(\sqrt{1+\kappa^2 R^2}\right)} \tag{3.44}$$

is a normalization constant depending on boundary radius R and the ratio κ. Fig. 3.6a shows a plot of the screening function $\Gamma_s(r)$ for different values of $\kappa \in [1,2]$. As expected, the contribution due to Gaussian curvature is maximum at the origin of the paraboloid and drops to zero at the boundary.

The calculation of the harmonic function $U(\boldsymbol{x})$ requires a little more effort. If the crystal was defect-free (or populated by a perfectly isotropic distribution of defects) the function $U(\boldsymbol{x})$ would be azimuthally symmetric and constant on the boundary. By the maximum principle of harmonic functions, $U(\boldsymbol{x})$ would then be constant on the whole manifold and depend only on κ and the radius R: $U(\boldsymbol{x}) = U_{\kappa,R}$. This constant can be determined by integrating $\Delta\chi(\boldsymbol{x}) = \Gamma(\boldsymbol{x})$ and imposing the second boundary condition in Eq. (3.39). This gives:

$$U_{\kappa,R} = \frac{2\pi}{A}\int_0^R dr\,\sqrt{g}\,\Gamma_s(r), \tag{3.45}$$

where A is the area of the paraboloid:

$$A = \frac{2\pi}{3\kappa^2}\left[\left(1+\kappa^2R^2\right)^{\frac{3}{2}} - 1\right]. \tag{3.46}$$

As shown in Figure 3.6b, the value of $U_{\kappa,R}$ quickly approaches the linear regime as the size of the radius increases:

$$U_{\kappa,R} \approx -\frac{1}{4}\,\kappa R + \frac{1}{3}. \tag{3.47}$$

Then, for a defect-free configuration, the contribution of the boundary to the energy density is a constant offset that persists even for large radii. In the presence of disclinations, on the other hand, the function $\chi(\boldsymbol{x})$ is no longer expected to be azimuthally symmetric and the harmonic function $U(\boldsymbol{x})$ will not be constant throughout the paraboloid. In this case $U(\boldsymbol{x})$ can be expressed in the integral form:

$$U(\boldsymbol{x}) = -\int d^2y\, H(\boldsymbol{x},\boldsymbol{y})\rho(\boldsymbol{y}), \tag{3.48}$$

where $H(\boldsymbol{x},\boldsymbol{y})$ is the harmonic kernel (3.18).

3.4.2 Large core energies: pyramidal lattices

In the regime of large core energies $F_c \gg F_{el}$, the creation of defects is strongly penalized and the lattice necessarily has the minimum number of disclinations allowed

by the topology of the paraboloidal substrate. From symmetry considerations, we might expect the optimal distribution of defects to consist of b $+1-$disclinations arranged along the boundary at the base vertices of a b-gonal pyramid and a b-fold apex (of topological charge $q_0 = 6 - b$) at the origin. The homogeneous boundary conditions adopted require the first term in Eq. (3.42) to vanish at the boundary. In the minimal energy configuration then, the system has the freedom to tune the total number of defects along the boundary to minimize the elastic energy Eq. (3.37) for any given value of the ratio κ. This behavior is exclusive to manifolds with boundary and doesn't have any counterpart in crystals on compact surfaces like the sphere and the torus. In the following, we will see how this minimization leads to properties which we believe to hold, in the most general sense, on any surface with boundary.

We will label a pyramidal configuration by Y_b, where b denotes the number of base $+1-$disclinations. The coordinates (r, ϕ) of the vertices are given by:

$$Y_b : \qquad \left\{ (0, \text{any}),\ \left(R, \frac{2\pi k}{b} \right)_{1 \le k \le b} \right\}. \tag{3.49}$$

Using the Euler theorem one can show that it is possible to construct infinite families of polyhedra with the symmetry group C_{bv} from the pyramidal backbone Y_b. The number of vertices is given by:

$$V = \tfrac{1}{2} bn(n+1) + 1, \tag{3.50}$$

where n is a positive integer which represents the number of edges (not necessarily of the same length) of the polyhedron which separates two neighboring disclinations. In the following we will refer to these polyhedra with the symbol $Y_{b,n}$. Fig. 3.7 illustrates two $Y_{b,n}$ lattices for the cases $b = 4$ and $n = 7$ (with $V = 113$), and $b = 5$ and $n = 10$ ($V = 276$). By a numerical minimization of the energy Eq. (3.37) one can establish that the Y_b are indeed equilibrium configurations for $b \in [3, 5]$, for some range of the parameters κ and R. The cases of $b = 5, 6$ are particularly significant because they are characterized by an equal number of defects ($N = 6$) of the same topological

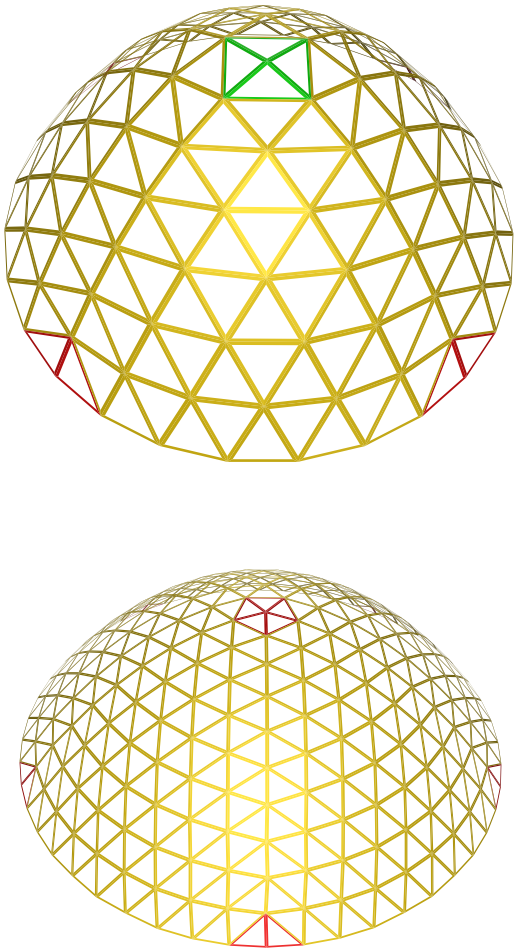

Figure 3.7: (Color online) Two examples of $Y_{b,n}$ triangulations of the paraboloid ($Y_{4,7}$ on the top and $Y_{5,10}$ on the bottom). Plaquettes with disclinations are highlighted in red, for $+1-$disclinations, and green for $+2-$disclinations.

charge ($q = 1$). The two configurations will be associated therefore with the same core energy F_c and this introduces the possibility of a structural transition between Y_5 and Y_6 governed by the curvature ratio κ and the boundary radius R. For fixed R and small values of κ the $6-$fold symmetric configuration Y_6 is the global minimum of the free energy Eq. (3.37). For κ larger than some critical value $\kappa_c(R)$, however, the Y_6 crystal becomes unstable with respect to the $5-$fold symmetric configuration

Y_5. A numerical calculation of the intersection point between the elastic energies of Y_5 and Y_6 for different values of κ and R allow us to construct the phase diagram shown in Fig. 3.8. The word "phase" in this context refers to the symmetry of the ground state configuration as a function of the geometrical system parameters κ and R. In principle, if we keep increasing the curvature we might expect the crystal to undergo a further transition to the Y_4 phase. In this case, however, the core energy will also increase by a factor 4/3 and so this is not generally possible in the regime in which $F_c \gg F_{el}$. For intermediate regimes (i.e. $F_c \sim F_{el}$), $Y_5 \to Y_4$ and $Y_4 \to Y_3$ transitions are also possible. The critical value of the parameters κ and R, however, is not universal and will depend on the precise values of the core energy and the Young modulus.

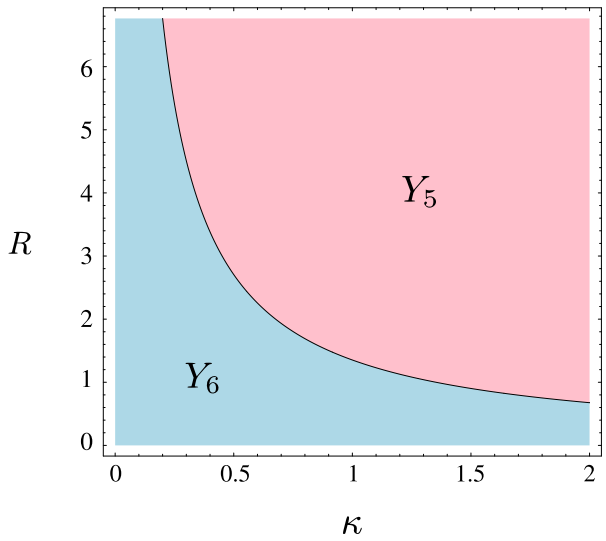

Figure 3.8: (Color online) Phase diagram in the large core energy regime. For small κ the lattice preserves the 6−fold rotational symmetry of the flat case. As the curvature at the origin increases the system undergoes a transition to the Y_5 phase.

The scenario depicted in Fig. 3.8 can be understood heuristically by imagining a system of spherically symmetric equally sized subunits initially arranged on the surface of a planar disk ($\kappa = 0$). The most efficient packing of this system is clearly the one in which the subunits are arranged in a triangular lattice with six 3−fold

sites on the boundary at the vertices of a hexagon. If now we slightly deform the disk into a low-curvature paraboloid ($\kappa > 0$) we might expect the hexagonal configuration to persist for small values of κ. When the deformation is more pronounced, however, the curvature at the origin will be enough to support the existence of a $5-$fold vertex and the system will undergo a structural transition from the Y_6 to the Y_5 phase. In principle, if we keep increasing the curvature we might expect the crystal to undergo a further transition to the Y_4 phase. In this case, however, the core energy will also increase by a factor $4/3$ and so this is not generally possible in the regime in which $F_c \gg F_{el}$. For intermediate regimes (i.e. $F_c \sim F_{el}$), $Y_5 \to Y_4$ and $Y_4 \to Y_3$ transitions are also possible. The critical value of the parameters κ and R, however, is not universal and will depend in detail on the values of the core energy and the Young modulus.

3.4.3 Small core energies: scars and coexistence

When the core energy F_c is small, the elastic energy Eq. (3.37) can be lowered by creating additional defects. Let us assume that a fivefold disclination is sitting at the point $\boldsymbol{x}_0 = (r_0, \phi_0)$. We can introduce a notion of distance on the paraboloid by setting up a system of geodesic polar coordinates (s, φ) with origin at $\boldsymbol{x}_0$. We expect that the stress introduced by the defect is controlled by an effective disclination charge inside a circular domain C_L of geodesic radius L:

$$q_{\mathit{eff}} = q - \int_0^{2\pi} d\varphi \int_0^L ds\, \sqrt{g}\, K(s, \varphi), \tag{3.51}$$

where $q = \pi/3$ is the charge of the isolated defect and the integral measures the screening due to the total Gaussian curvature within the domain. The metric tensor and the Gaussian curvature of a generic Riemannian manifold can be expressed in

geodesic polar coordinates in the form (see for example Do Carmo [108]):

$$g_{ss} = 1, \qquad g_{s\varphi} = 0, \qquad g_{\varphi\varphi} = G, \tag{3.52a}$$

$$K(s,\varphi) = -\frac{\partial_s^2\sqrt{G}}{\sqrt{G}}, \tag{3.52b}$$

where $G = \boldsymbol{g}_\varphi \cdot \boldsymbol{g}_\varphi$. Furthermore, an expansion of the metric around the origin $(0,\varphi)$ yields:

$$\sqrt{G} = s - \tfrac{1}{6}K_0 s^3 + o(s^5).$$

For small distance from the origin, Eq. (3.51) becomes:

$$q_{\mathit{eff}} = q + \int_0^{2\pi} d\varphi \int_0^L ds\, \partial_s^2\sqrt{G} \tag{3.53}$$

$$= q - \pi K_0 L^2 + o(L^4). \tag{3.54}$$

The right hand side of Eq. (3.54) is a very general expression for the effective disclination charge at small distance and doesn't depend on the embedding manifold. If a grain boundary is radiating from the original disclination, we expect the spacing between consecutive dislocations to scale like a/q_{eff}, with a the lattice spacing [72]. When $q_{\mathit{eff}} \to 0^+$ the dislocation spacing diverges and the grain boundary terminates. Since the Gaussian curvature is not constant, the choice of the origin (i.e. the position of the central disclination along the grain boundary) affects the evaluation of q_{eff}. One can identify upper and lower bounds by observing that:

$$\max_r K(r) = K(0) = \kappa^2, \tag{3.55a}$$

$$\min_r K(r) = K(R) = \frac{\kappa^2}{(1+\kappa^2 R^2)^2}. \tag{3.55b}$$

Unlike the case of surfaces of constant Gaussian curvature, the phase diagram for paraboloidal crystals consists of three regions separated by the curves:

$$K_0 L^2 = \frac{1}{3} \qquad K_0 = K_{\min},\, K_{\max}. \tag{3.56}$$

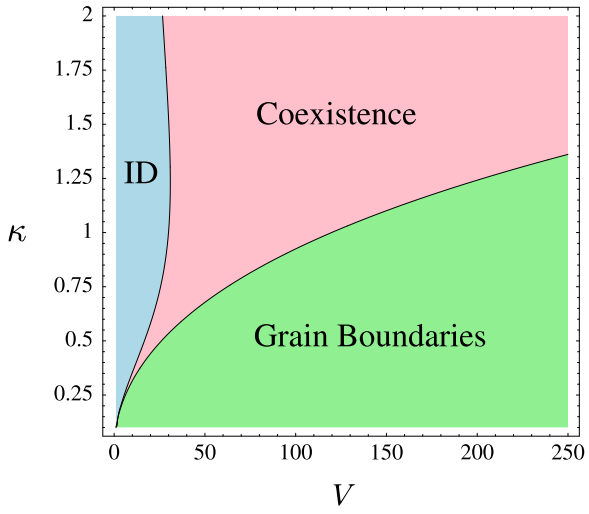

Figure 3.9: (Color online) Defect phase diagram for a paraboloidal crystal of radius $R = 1$. The two phase boundaries that separate the isolated disclinations (ID) regime from the coexistence regime and the coexistence regime from the scar phase correspond to the solutions of Eq. (3.57) for $K_0 = K_{\min}$ and $K_0 = K_{\max}$, respectively.

When $L - L(K_{\min}) \to 0^+$ the effective disclination charge goes to zero and the distance between two consecutive dislocations diverges at any point. On the other hand if $L - L(K_{\max}) \to 0^-$, the disclination charge will prefer to be delocalized in the form of grain boundary scars. For $L(K_{\max}) < L < L(K_{\min})$ the paraboloid will be equipped with regions where the Gaussian curvature is high enough to support the existence of isolated disclinations as well as regions where the screening due to the curvature is no longer sufficient and the proliferation of grain boundary scars is energetically favored. This leads to a three region phase diagram in which the regime of isolated disclinations is separated from the delocalized regime of scars by a novel phase in which both isolated disclinations and scars coexist in different parts of the paraboloid according to the magnitude of the Gaussian curvature.

It is useful to measure the distance L_c in terms of the lattice spacing a and rephrase Eq. (3.56) as a condition on a (or equivalently on the number of vertices V). To do this we note that in order for the domain C_L to completely screen the topological

charge of the shortest scar possible (i.e. $5-7-5$), the geodesic radius L has to be large enough to enclose the entire length of the scar. Calling ℓ the geodesic distance associated with a single lattice spacing a, we will then approximate $L \sim 3\ell$. This leads to the following expression for the lattice spacing a at the onset of scar formation:

$$a^2 \approx \frac{2}{K_0}\left(1-\cos\frac{1}{3\sqrt{3}}\right). \tag{3.57}$$

The lattice spacing a can be approximately expressed as a function of the number of vertices of the crystal by dividing the area A of the paraboloid by the area of a hexagonal Voronoi cell of radius $a/2$ with $a^2 \approx A/\frac{\sqrt{3}}{2}V$. The phase diagram arising from the solution of Eq. (3.57) is sketched in Fig. 3.9 for the case $R=1$. The two phase boundaries that separate the isolated defects (ID in the plot) regime from the coexistence regime and this one from the grain boundaries phase correspond, respectively, to the solutions for $K_0 = K_{\min}$ and $K_0 = K_{\max}$. The simplicity of the criteria used to derive Eqs. (3.56) doesn't allow us to predict the regions surrounding the phase boundaries with high numerical accuracy, but does provide a semi-quantitative picture of the novel phenomenology of defects in non-Euclidean crystals that is generally supported by the numerical results presented in §3.4.4.

3.4.4 Paraboloidal Coulomb crystals

In the following section I report the results of a numerical minimization of a system of V classical particles interacting via a Coulomb potential $E = \sum_{i<j} 1/|\boldsymbol{x}_i - \boldsymbol{x}_j|$ on the surface of a paraboloid. The equilibrium configuration arising from this optimization problem can be viewed as a direct realization of a paraboloidal crystal and thus provides a testing ground for our analytical results.

The determination of the equilibrium properties of complex systems is complicated by the rich topography of the energy landscape, with its many, often deep, local minima (valleys) separated by high barriers (passes). The number of local minima grows rapidly with system size, making it increasingly difficult, or impossible, to find

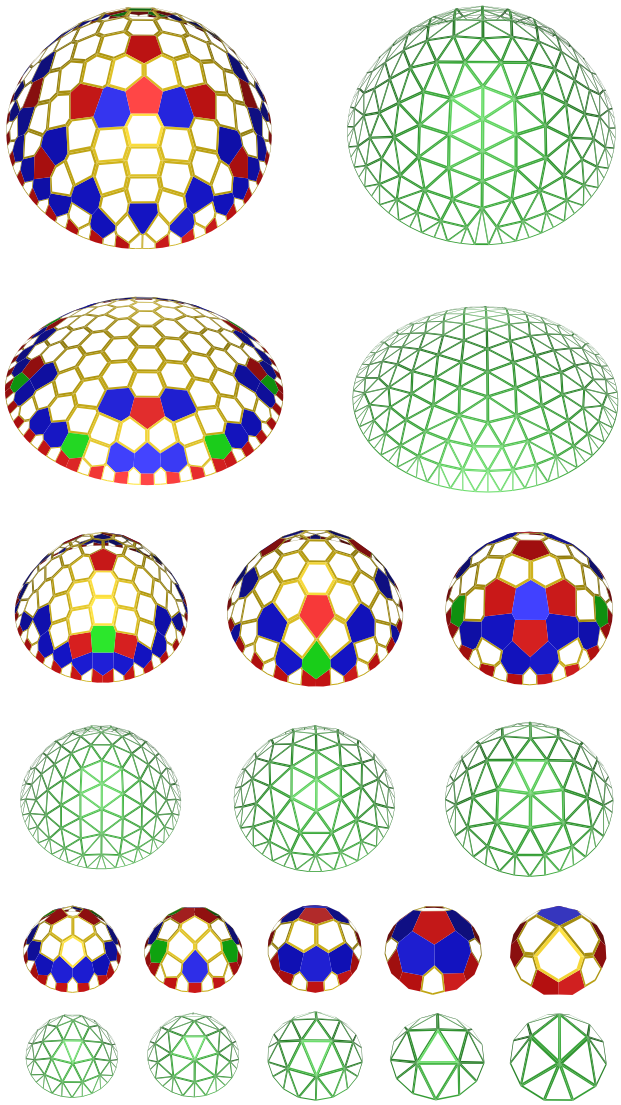

Figure 3.10: (Color online) Voronoi lattice and Delaunay triangulations for ten selected systems from numerical simulations with $R = 1$. The first row corresponds to $V = 200$ and $\kappa = 1.6$, while the second row is for $V = 200$ and $\kappa = 0.8$. In the bottom four rows $V = 150\,, 100\,, 80\,, 60\,, 50\,, 30\,, 20\,, 16$ and $\kappa = 1.6$. From [107].

the global minimum. The effort in solving a given global optimization problem is described by computational complexity theory. Locating the global minimum for a potential energy surface belongs to the class of problems known as NP-hard, for which there is no known algorithm that is certain to solve the problem within a time that scales as a power of the system size.

The Thomson problem [78–80, 89–92, 109] of finding the optimal configuration of V interacting charges on a 2-sphere represents, in this context, a celebrated example of a hard optimization problem. The existence of novel arrays of topological defects in minimal energy configurations provides further insight into the structure of the energy landscape. Computer experiments on the Thomson problem indicate that, in the range $70 \leq V \leq 112$, the number of local minima for each value of V grows exponentially: $\mathcal{N} \simeq 0.382 \exp(0.0497\, V)$ [90]. This trend is believed to continue for larger values of V, making the determination of the global minimum a formidable computational challenge. In the case of the paraboloid we believe the prefactor in this scaling law is larger due to the additional constraint of the boundary.

To construct equilibrium lattice configurations we adopted a parallel implementation of Differential Evolution (DE) [106, 110] (see Appendix 3.A for an introductory description of the algorithm together with the parallelization strategy). The initial pool of candidate solutions is generated at the beginning of the simulation by randomly creating $NP = 20V$ configurations uniformly distributed over the whole search space $\{r \in [0, R]\} \otimes \{\phi \in [0, 2\pi]\}$. The population is then evolved by $3 \cdot 10^5$ DE iterations on ten processors working in parallel.

In Fig. 3.10 we show the Voronoi lattice and the Delaunay triangulations for five selected systems up to $V = 200$ particles. The lowest energy seen, together with the number of $n-$fold vertices, for each one of these lattices is reported in Table 3.4.4. In all the systems observed disclinations always appear clustered in either grain boundary scars or dislocations with the exception of isolated $+1-$disclinations which appearing in the bulk as expected from the curvature screening argument discussed

V	V_{-2}	V_{-1}	V_0	V_1	Energy
10	0	0	4	6	36.94485696974016
20	0	4	6	10	179.5291483377297
30	0	6	12	12	439.0497473530407
40	2	5	18	15	818.8300625504069
50	4	4	24	18	1321.878894548272
60	2	10	28	20	1949.230291403783
70	2	16	26	26	2701.959660541221
80	3	17	31	29	3581.110585181344
90	2	16	46	26	4588.364706108566
100	3	15	55	27	5722.503370970009
150	1	30	81	38	13323.70617345018
200	3	35	115	47	24173.21580330549

Table 3.1: Numerical data for twelve selected lattices. The quantities V_q represent the number of vertices in the crystal with topological charge q.

in §3.4.1. The complex aggregation of defects along the boundary together with the presence of negatively charged clusters indicates that the effect of the boundary, in the case of relatively small systems like the ones simulated, is more drastic than predicted by the homogeneous boundary conditions Eq. (3.39). Even in the computationally expensive case of $V = 100$, the distance between the origin and the boundary of the paraboloid is only four lattice spacings. In this situation we expect the distribution of particles along the boundary to play a major role in driving the order in the bulk.

For larger systems, such as $V = 200$ (top of Fig. 3.10), the behavior of the particles in the bulk is less affected by the boundary and the crystalline order reflects more closely the free-boundary problem discussed in §3.4.1. A comparison of the lattices in the first two rows of Fig. 3.10, in particular, reveals substantial agreement with the scenario described in Sec. 3.4.2. For $\kappa = 0.8$ and $V = 200$, the defects are all localized along the boundary with the exception of one length-3 scar in the bulk at distance $r \approx 0.63$ from the center. For $\kappa = 1.6$, the pattern of defects in the bulk is characterized by the coexistence of an isolated $+1-$disclination at the origin and a length-5 $W-$shaped scar displaced along a parallel one lattice spacing away from the central disclination. Apart from the evident difficulty in comparing the structures of small systems with those predicted from continuum elasticity theory, this behavior is consistent with the simple picture sketched in the phase-diagram of Fig. 3.9. The local $5-$fold symmetry at the origin of the $\kappa = 1.6$ configuration, compared with $6-$fold symmetry for $\kappa = 0.8$, suggests, as in the case of spherical crystals [111], that the complicated structure of defect clusters appearing in large systems is the result of the instability of the simpler $Y_{b,n}$ configurations from which they partially inherit their overall symmetry. A more accurate numerical verification of our theory remains a challenge for the future.

The symmetry of the configurations presented in Fig. 3.10 deserves special attention. As for any surface of revolution, the circular paraboloid belongs possesses the symmetry group $O(2)$ of all rotations about a fixed point and reflections in any axis

through that fixed point. Any given triangulation of the paraboloid may destroy the full rotational symmetry completely or just partially, leaving the system in one of the following two subgroups: the pyramidal group C_{nv} or the reflection symmetry group C_s. In general we found the latter symmetry group for system sizes up to $V = 200$ particles. The symmetry for larger system sizes is under investigation.

3.5 Experimental realization of paraboloidal crystals

Some sixty years ago Bragg and Nye used bubble rafts to model metallic crystalline structures [112]. A carefully made assemblage of bubbles, floating on the surface of a soap solution and held together by capillary forces, forms an excellent two-dimensional replica of a crystalline solid, in which the regular triangular arrangement of bubbles is analogous to the close packed structure of atoms in a metal. Feynman considered this technique to be important enough that the famous Feynman lectures in physics include a reproduction of the original Bragg-Nye paper in its entirety [113]. Bubble rafts can be made easily and inexpensively, equilibrate quickly, exhibit topological defects such as disclinations, dislocations and grain boundaries, and provide vivid images of the structure of defects. Bubble raft models have been used to study two-dimensional polycrystalline and amorphous arrays [114], nanoindentation of an initially defect-free crystal [115], and the dynamic behavior of crystals under shear [116]. In this section we review the experimental realization of a bubble-raft model for a paraboloidal crystal done in collaboration with H. Shin and C. Thomas [100] by assembling a single layer of millimeter-sized soap bubbles on the surface of a rotating liquid, thus extending the classic work of Bragg and Nye on planar soap bubble rafts.

As we mentioned in the introduction, paraboloidal shapes naturally occur across the air/liquid interface of a fluid placed in a rotating cylindrical vessel. It is simple to verify that the height z of such an interface above the $xy-$plane of a system of

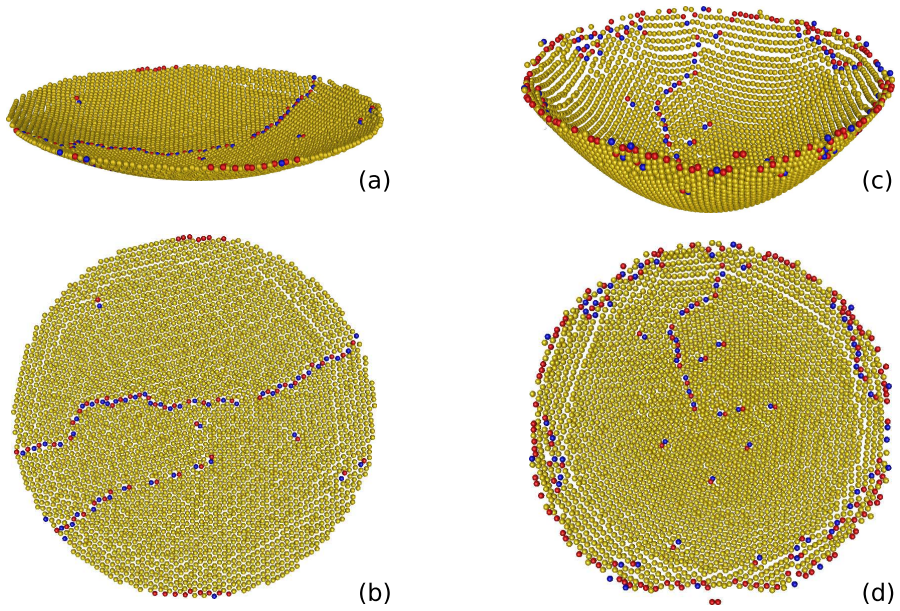

Figure 3.11: (Color online) Lateral and top view of a computer reconstruction of two paraboloidal rafts with $\kappa_1 \approx 0.15\,\mathrm{cm}^{-1}$ (a, b) and $\kappa_2 \approx 0.32\,\mathrm{cm}^{-1}$ (c, d). The number of bubbles is $N_1 = 3813$ and $N_2 = 3299$ respectively. The color scheme highlights the 5−fold (red) and 7−fold (blue) disclinations over 6−fold coordinated bubbles (yellow). From Ref. [100].

Cartesian coordinates is given by:

$$z = \frac{\omega^2}{2g}\, r^2 + C\,, \tag{3.58}$$

where ω is the angular velocity and g the gravitational acceleration and $C = D - \omega^2 R^2/4g$ is an integration constant following from the requirement that the volume of the liquid during rotation be equal to the volume of the liquid at rest (D is its height) [117]. Thus the normal curvature at the origin is given by $\kappa = \omega^2/g$.

To make the bubble rafts, we pump air through a needle into soapy water. Because the larger bubble sizes we prefer are most easily made when the vessel is still, we first make the bubbles and only later spin the vessel to make the paraboloid (cf. Bragg and Nye [112], who spun their system in order to generate smaller bubbles but stopped the spinning to look at the bubbles on a flat surface). To image the bubbles, we mount a CCD digital camera on the top of the vessel, with lighting from a ring

around the (clear) vessel to eliminate glare. The camera rotates along with the whole system so that the shutter speed is unimportant in imaging the bubbles. We use a second camera to find the aspect ratio of the paraboloid. We equilibrate the system and eliminate stacking of bubbles by imposing small perturbations of the angular frequency to mimic the role of thermal noise. The vessel has radius $R = 5$ cm; the height of paraboloids varies from $h = 0$–4 cm. The bubble diameter, extracted from the Delaunay triangulation of our images, is $a = 0.84(1)$ mm with monodispersity $\Delta a/a \approx 0.003$. The normal curvature κ of the paraboloid at the origin varies from 0–0.32 cm^{-1}. In addition to the flat disk, we observe two different curvature regimes: small curvature $\kappa_1 \approx 0.15\,\mathrm{cm}^{-1}$ and large curvature $\kappa_2 \approx 0.32\,\mathrm{cm}^{-1}$. In each curvature class we collected several data sets with qualitatively similar results.

Fig. 3.11 shows a computer reconstruction of two bubble rafts with $\kappa = \kappa_1$ and κ_2 respectively. We extract two dimensional coordinates from the images with a brightness based particle location algorithm through the IDL platform [118]. Data sets are then processed to correct possible imprecisions and finally Delaunay triangulated. The adjacency list obtained from the Delaunay triangulation is then used to determine the valency and the position of disclination defects. We choose to exclude from the triangulation the first 3–4 bubble rings formed along the boundary of the cylindrical vessel, where the sharp concave meniscus due to the surface tension combined with the native curvature of the paraboloid was observed to produce a stacking of bubbles in a narrow double layer surrounding the perimeter of the vessel. This is the only significant boundary effect we observe in our system and does not hamper the identification of disclinations in the bulk.

To characterize the order of the crystalline raft, we measure the translational and orientational correlation functions $g(r)$ and $g_6(r)$ [119]. The former gives the probability of finding a particle at distance r from a second particle located at the origin. The function is normalized with the density of an equivalent homogeneous system in order to ensure $g(r) = 1$ for a system with no structure. Interactions between

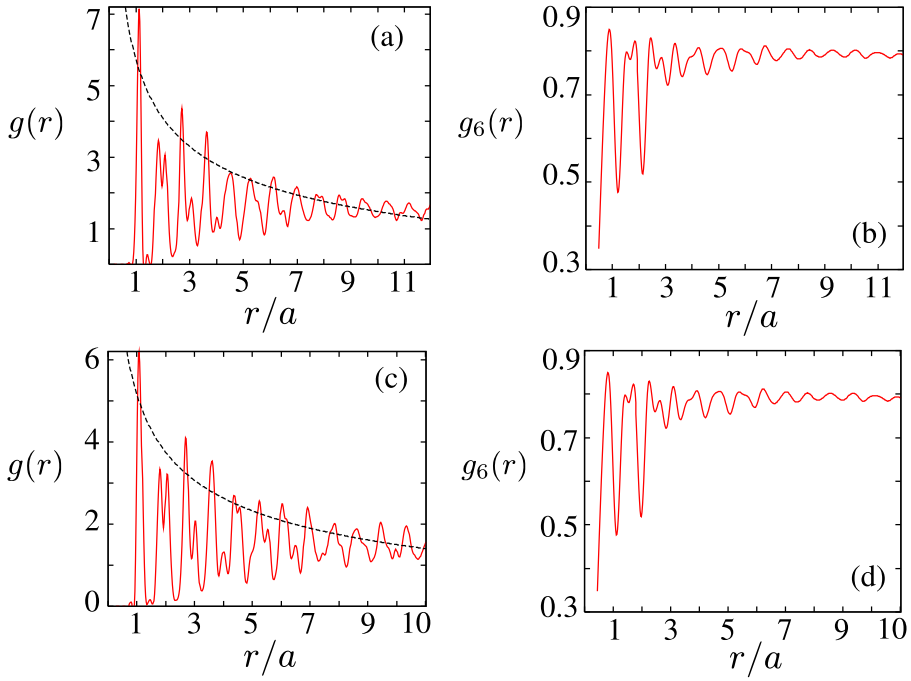

Figure 3.12: (Color online) Translational and orientational correlation functions (g and g_6, respectively) for rafts with (a,b) $\kappa \approx 0.32$ cm^{-1}, $a = (0.8410 \pm 0.0025)$ mm, and (c,d) $\kappa \approx 0.15$ cm^{-1}, $a = (0.9071 \pm 0.0037)$ mm. All the curves are plotted as functions of r/a, where r is the planar distance from the center and a is the bubble radius. The envelope for the crystalline solid decays algebraically (dashed line), while the orientational correlation function approaches the constant value 0.8. From Ref. [100].

particles build up correlations in their position and $g(r)$ exhibits decaying oscillations, asymptotically approaching one. For a two-dimensional solid with a triangular lattice structure the radial correlation function is expected to exhibit sharp peaks in correspondence with the sequence $r/a = \sqrt{n^2 + nm + m^2} = 1, \sqrt{3}, 2, 2\sqrt{3} \ldots$ while the amplitude of the peaks decays algebraically as $r^{-\eta}$ with $\eta = 1/3$ (dashed line in Fig. 3.12). Within the precision of our data, the positional order of the paraboloidal crystals assembled with the bubble raft model reflects this behavior, although with more accurate measurements, one might see dependence of the exponent η on the curvature (because of the proliferation of defects with curvature).

The orientational correlation function $g_6(r)$ is calculated as the average of the

product $\langle\psi(0)\psi^*(r)\rangle$ of the hexatic order parameter over the whole sample. For each bubble (labeled j) that has two or more neighbors, $\psi_j(r) = (1/Z_j)\sum_{k=1}^{Z_j}\exp(6i\theta_{jk})$, where Z_j is the number neighbors of i and θ_{jk} is the angle between the $j-k$ bonds and a reference axis. One expects $g_6(r)$ to decay exponentially in a disordered phase, algebraically in a hexatic phase and to approach a non zero value in the case of a crystalline solid. In the systems studied $g_6(r)$ approaches value 0.8 in the distance of 5–6 lattice spacings.

Of particular interest is the structure of the grain boundaries appearing in the paraboloidal lattice for different values of the curvature parameter κ. Grain boundaries form in the bubble array during the growing process as a consequence of geometrical frustration. As noted, any triangular lattice confined in a simply connected region with the topology of the disk is required to have a net disclination charge $Q = 6$. In absence of curvature, however, the elastic stress due to an isolated disclination is extremely high and defects are energetically favored to cluster in the form of a grain boundary consisting of one-dimensional arrays of tightly bound $(5,7)-$fold disclinations pairs. In a planar confined system, grain boundaries typically span the entire length of the crystal, but if a non-zero Gaussian curvature is added to the medium, they can appear in the form of scars carrying a net +1 topological charge and terminating in the bulk of the crystal.

Prominent examples of grain boundaries are visible in the two lattices shown in Fig. 3.11. For a gently curved paraboloid (with $\kappa \approx 0.15$ cm^{-1}), grain boundaries form long (possibly branched) chains running from one side to the other and passing through the center. As the curvature of the paraboloid is increased, however, this long grain boundary is observed to terminate in the center (see Fig. 3.11d; a close-up version of this image is seen in Fig. 3.13). For $R = 5$ cm, the elastic theory of defects predicts a structural transition at $\kappa_c = 0.27$ cm^{-1} in the limit of large core energies. In this limit the creation of defects is strongly penalized and the lattice has the minimum number of disclinations required by the topology of the embedding

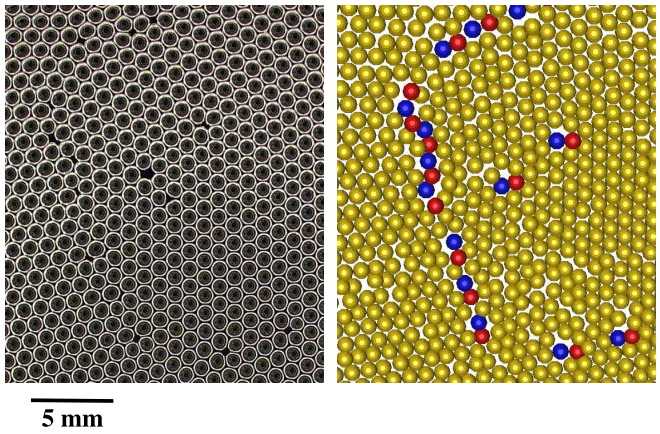

Figure 3.13: (Color online) An enlarged view of the terminating grain boundary scar shown in Fig 3.11d for a system with large Gaussian curvature. The scar starts from the circular perimeter of the vessel and terminates roughly in the center carrying a net +1 topological charge. The image of the bubbles (left) shows that they may deform slightly to better fill space, whereas the computer reconstruction of the lattice (right) uses perfect spheres of uniform size. From Ref. [100].

surface. In a low curvature paraboloid ($\kappa < \kappa_c$) these disclinations are preferentially located along the boundary to reduce the elastic energy of the system. When the aspect ratio of the paraboloid exceeds a critical value $\kappa_c(R)$, however, the curvature at the origin is enough to support the existence of a $5-$fold disclination and the system undergoes a structural transition. In the limit of large core energies, when only six disclinations are present, such a transition implies a change from the C_{6v} to the C_{5v} rotational symmetry group.

Together with the theoretical argument reviewed in the previous section, these experimental observations point to the following mechanism for scar nucleation in a paraboloidal crystal. In the regime in which the creation of defects is energetically inexpensive, geometrical frustration due to the confinement of the lattice in a simply connected region is responsible for the formation of a long side-to-side grain boundary. However, when the curvature of the paraboloid exceeds a critical value dependent on the radius of the circular boundary , the existence of a +1 disclination near the center is energetically favored. Such a disclination serves as a nucleation site for

5 7 dislocations and the side-to-side grain boundary is replaced by a terminating center-to-side scar. Above the critical curvature the elastic theory outlined in §3.4 also predicts a regime of coexistence of isolated disclinations and scars due to the variable Gaussian curvature. For dense systems (i.e. number of subunits larger than a few hundred for our geometry), the coexistence is suppressed because the embedding surface will appear nearly flat at the length scale of a lattice spacing. The bulk of the system is thus populated uniquely by scars. This is consistent with our experimental observation.

Away from the center of the paraboloid, we have compared the crystalline directions with the geodesics starting from a given reference point (see Fig. 3.14). Near the boundary, the directions of both first and second neighbors (in red and blue respectively), are reasonably aligned with the geodesics. The alignment becomes decorrelated after roughly five lattice spacings with the decorrelation more pronounced in the radial direction (maximal principal curvature) where the normal curvature is largest. As one gets closer to the center, the geodesic correlation becomes weaker and almost completely vanishes along the radial direction. Along the angular direction (minimal principal curvature), on the other hand, the crystalline axes appear aligned with the geodesic directions.

Appendix 3.A Optimization via Parallel Differential Evolution

Many of the techniques proposed to determine the crystalline structure of systems of interacting particles, as in the Thomson problem, are based on local optimization procedures such as steepest descent, conjugate gradient and the quasi-Newton method. Such methods belong to the class of line-search algorithms for multidimensional non-linear programming problems. They can be described, in general, as a sequence of line minimizations of an objective function along a set of directions that

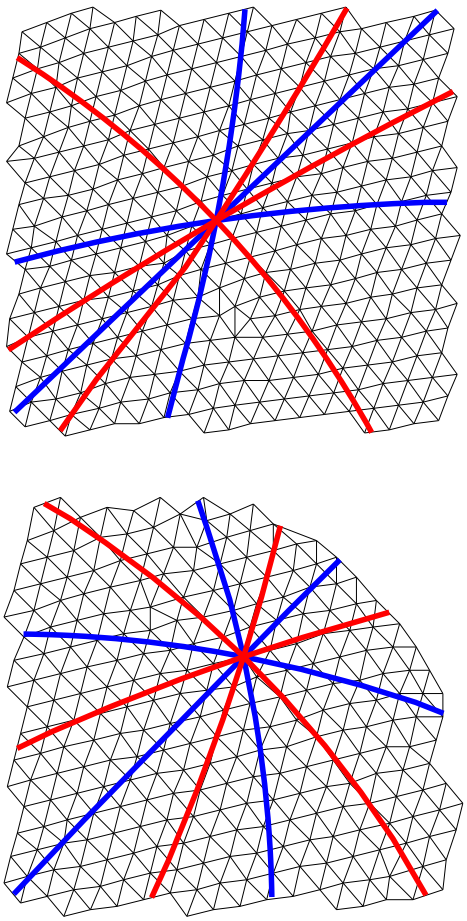

Figure 3.14: (color online) Delaunay triangulation of a portion of the paraboloidal lattice with $\kappa \approx 0.32$ cm^{-1} near the center (top) and the boundary (bottom). Red (lighter) and blue (darker) lines represent the geodesics directed toward first and second neighbors, respectively.

are generated differently in different algorithms. Besides the well known local convergence properties of these methods, they are generally unable to locate the global minimum since they inherently approach the closest local minimum for a given set of initial conditions.

To avoid the misconvergence problem described we adopt the Differential Evolution (DE) algorithm of Storn and Price [110]. This algorithm, which has been successfully applied to several optimization problems in engineering [120], belongs to the family of evolutionary algorithms which are considerably faster than other stochas-

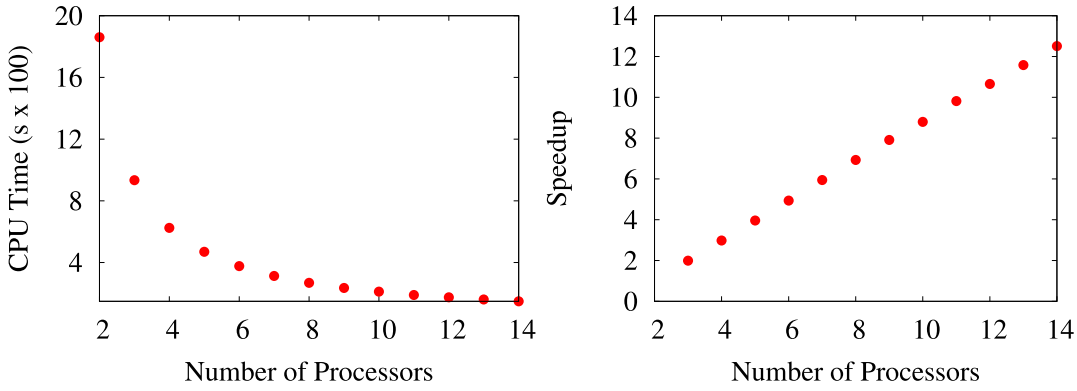

Figure 3.15: (Color online) CPU-Time and speedup (i.e. the time employed by n processors to accomplished a given number of iterations divided by the time employed by a single machine to achieve the same task).

tic optimization methods, such as simulated annealing and genetic algorithms, and more likely to find the correct global minimum. These methods heuristically mimic biological evolution by implementing natural selection and the principle of "survival of the fittest". An adaptive search procedure based on a population of candidate solutions is used. Iterations involve a competitive selection that drops the poorer solutions. The remaining pool of candidates are perturbed (or mutated) in order to generate trial individuals and then recombined with other solutions by a swap of the components. The recombination and mutation moves are applied sequentially; their aim is to generate new solutions that are biased towards subsets of the search space in which good, although not necessarily globally optimized, solutions have already been found.

An essential feature of Differential Evolution is the establishment of genetic diversity, which helps to maximize the probability of finding the true global minimum and to avoid misconvergence. One begins with a large population of individuals uniformly distributed in the search space. A good choice, in practice, is to choose the number of individuals to be an order of magnitude more than the number of variables in the

problem. The price one pays is a dramatic slowing down of the algorithm when applied to large scale optimization. Considerable effort has therefore been made in the past ten years to develop parallel implementations of evolutionary algorithms aimed at reducing the overall time to completion of the task by distributing the work on different processors working in parallel. More recently some researchers have conjectured that some parallelizations of a task improve the quality of the solution obtained for a given overall amount of work (e.g. emergent computation).

The *Island Model* is a popular choice among parallelization strategies and is implemented within a message passing model. It consists of dividing the initial population into several sub-populations and letting each of them evolve independently on a single machine for a predetermined number of iterations (called the *epoch*). The exchange of genetic information is promoted by swapping individuals between different sub-populations at the end of each epoch. In the present work the migration strategy consists in swapping the best individual of each sub-population with a randomly selected individual on another island with the ring topology chosen for the connectivity between islands. This choice allowed us to achieve a substantial reduction of the CPU time and a linear speedup (see Fig. 3.15).

Appendix 3.B The function $\Gamma_s(\boldsymbol{x})$ on the paraboloid

To obtain the expression for $\Gamma(\boldsymbol{x})$ given in Eq. (3.43) one has to calculate the integral:

$$\Gamma_s(\boldsymbol{x}) = \int d^2y\, G_L(\boldsymbol{x},\boldsymbol{y}) K(|\boldsymbol{y}|) = \Gamma_{s,1}(\boldsymbol{x}) - \Gamma_{s,2}(\boldsymbol{x}), \tag{3.59}$$

having called:

$$\Gamma_{s,1}(\boldsymbol{x}) = \frac{1}{2\pi} \int d\phi'\, dr'\, \sqrt{g}\, K(r') \log|z-\zeta|, \tag{3.60a}$$

$$\Gamma_{s,2}(\boldsymbol{x}) = \frac{1}{2\pi} \int d\phi'\, dr'\, \sqrt{g}\, K(r') \log|1-z\overline{\zeta}|. \tag{3.60b}$$

For this purpose one can use the expansion:

$$\log|z-\zeta| = \log\varrho_> - \sum_{n=1}^{\infty}\frac{1}{n}\left(\frac{\varrho_<}{\varrho_>}\right)^n \cos n\delta\phi, \tag{3.61}$$

where $\varrho_>$ ($\varrho_<$) represents the largest (smallest) modulus between z and ζ, while $\delta\phi = \phi - \phi'$. The factorization of the angular variables in Eq. (3.61), together with the pure radial dependence of the Gaussian curvature and $\sqrt{g}$, makes the angular dependence of $\Gamma_{s,1}$ vanish, so that we have:

$$\Gamma_{s,1}(\boldsymbol{x}) = \log\varrho(r)\int_0^r dr'\,\frac{\kappa^2 r'}{(1+\kappa^2 r'^2)^{\frac{3}{2}}} + \int_r^R dr'\,\frac{\kappa^2 r'}{(1+\kappa^2 r'^2)^{\frac{3}{2}}}\log\varrho(r'), \tag{3.62}$$

which integrated by parts gives:

$$\Gamma_{s,1}(\boldsymbol{x}) = \log\left(\frac{\alpha e^{\sqrt{1+\kappa^2 r^2}}}{1+\sqrt{1+\kappa^2 r^2}}\right). \tag{3.63}$$

Using an expansion similar to (3.61) it is also possible to prove that

$$\log|1-z\overline{\zeta}| = -\sum_{n=1}^{\infty}\frac{1}{n}\left(\varrho\varrho'\right)^n\cos\delta\phi, \tag{3.64}$$

which integrated over the surface of the paraboloid gives $\Gamma_{s,2} = 0$. This last conclusion, combined with Eq. (3.63), yields Eq. (3.43).

Chapter 4

Crystalline and $p-$atic order in toroidal geometries

4.1 Introduction

Circa twenty years afer their first observation in partially polymerized diacetylenic phospholipid membranes by Mutz and Bensimon [121], self-assembled toroidal aggregates are now considered the progenitors of a magnificent cornucopia of complex structures, also featuring branched network and micellar surfaces of high genus. The existence of such complex structures has become an experimental fact thanks to the enormous work in the past decade on the study of self-assembly of amphiphilic compounds such as lipids, surfactants and amphiphilic block copolymers. After the work of Eisenberg and coworkers [122–124] it became clear that block copolymer in particular afford access to a variety of complex structures spanning an unexpectedly vast range of topologies and geometries. More recently, several experimental studies have been performed on di- and triblock copolymers with the intent of unraveling the origin of morphological complexity in copolymer surfactants and some possible pathways for micelle and vesicle formation have been proposed.

Jain and Bates, for instance, reported the formation of several non-simply-connected

micellar structures from the self-assembly of diblock copolymer poly(1,2-butadiene-*b*-ethylene oxide) (PB-PEO) [125] (see Fig. 4.1). These polymers self-assemble in $Y-$shaped junctions and these form the building blocks for more complex micellar structures via re-assembly. Later, Pochan *et al.* [126] found that almost all of the microstructures assembled from poly(acrylic acid-*b*-methyl acrylate-*b*-styrene) (PAA99-PMA73-PS66) triblock copolymers are ringlike or toroidal micelles. The route to toroidal micelles in block copolymers, however, is believed to be different from that to more complex network structures suggested by Jain and Bates, since residual $Y-$shaped aggregates are very rarely found in the sample. According to the authors of Ref. [126], the formation of toroidal micelles has to be attributed primarly to the collapse of cylindrical micelles. On the other hand, mere end-to-end connection of cylindrical micelles doesn't appear to be the exclusive ring-forming mechanism in triblock systems since the average circumference of the self-assembled tori appears smaller than the contour length of the average cylindrical micelles. It seems some more complicated process, possibly involving interactions and exchange of matter between neighboring cylinders.

Toroidal micelles have also been observed in recent experiments by Kim *et al* [127] from the self-assembly of amphiphilic dumbbell molecules based on a aromatic rod segment that is grafted by hydrophilic polyether dendrons at one end and hydrophobic branches at the other end. Molecular dumbbells dissolved in a selective solvent self-assemble in an aggregate structure due to their amphiphilic character. This process has been observed to yield coexisting spherical and open-ended cylindrical micelles. These structures, however, change slowly over the course of a week to toroidal micelles which thus appear more stable. The formation of ring-like structures was explained in this case as result of the coalescence of spherical micelles occurring to reduce the contact between hydrophobic segments and water molecules.

An alternative pathway for the self-assembly of toroidal structures in copolymer solutions has been proposed and numerically tested by He and Schimd [128]. In this

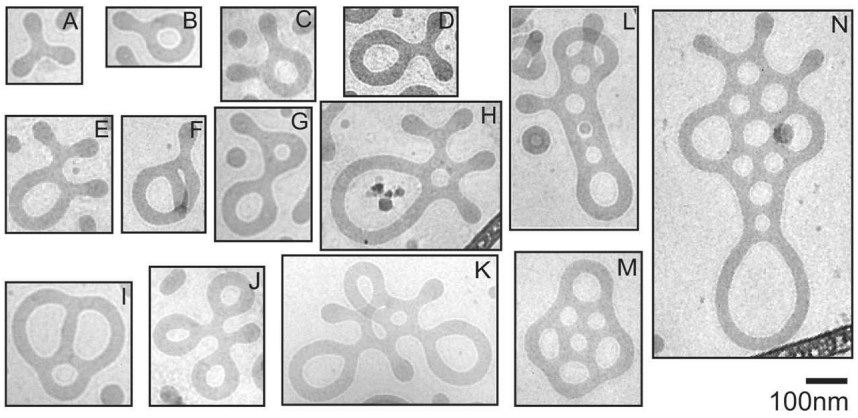

Figure 4.1: Complex non-simply connected structures from self-assembly of diblock copolymer poly(1,2-butadiene-b-ethylene oxide) (PB-PEO). From Ref. [125].

pathway, the micelles do not coalesce, but simply grow by attracting copolymers from the solution. Once a critical micelle size is exceeded, copolymers start to flip-flop in such a way that the micelle core becomes itself solvent-philic (semi-vesicle state). Finally the solvent diffuses inside the core and the semi-vesicle swells into a vesicle.

The existence of toroidal aggregates in amphiphilic compounds was suggested theoretically for smectic-C (SmC) membranes, based on the argument that orientational order is not frustrated on a surface with zero Euler characteristic and thus a toroidal topology may be energetically favoured in $p-$atic membranes with large order parameter coupling compared with the bending rigidity [58, 129]. This hypothesis was tested by Evans in 1995 with the result that a toroidal topology is indeed prefered over the spherical one for wide range of geometrical and mechanical parameters in defect-free $p-$atic tori. The role of disclinations in $p-$atic tori was investigated systematically by Bowick, Nelson and Travesset nine years after the original work of Evans with the conclusion that, even if not required by topological constraints, unbound disclinations can be energetically convenient even in very dense systems [130]. The precise number of unbound disclinations is controlled primarly by the aspect ratio of the torus. The existence of defects in the ground state of an ordered phase on the torus becomes

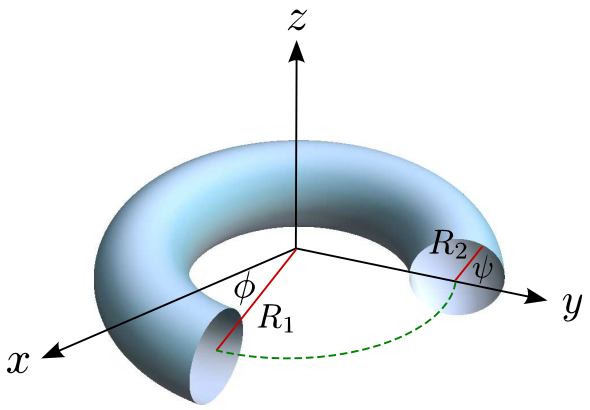

Figure 4.2: (Color online) The standard parametrization of a circular torus of radii R_1 and R_2.

crucial for toroidal crystals where it leads to some unique structural features as well as a spectacular example of a curvature-driven transition to a disordered, liquid-like, state in the limit the aspect ratio approaches to one [131, 132]. In the remainder of this section we will review these three examples of order on embedded tori.

4.2 Geometry of the torus

The standard two-dimensional axisymmetric torus embedded in $\mathbb{R}^3$ is obtained by revolving a circle of radius R_2 about a coplanar axis located at distance $R_1 \geq R_2$ from its center. Choosing the symmetry axis as the z direction of a Cartesian frame, a convenient parametrization can be found in terms of the polar angle ψ along the revolving circle and the azimuthal angle ϕ on the $xy-$plane:

$$\begin{cases} x = (R_1 + R_2 \cos\psi)\cos\phi \\ y = (R_1 + R_2 \cos\psi)\sin\phi \\ z = R_2 \sin\psi \end{cases} , \tag{4.1}$$

where $\psi\,, \phi \in [-\pi, \pi)$. These coordinates satisfy the Cartesian equation:

$$\left(R_1 - \sqrt{x^2 + y^2}\right)^2 + z^2 = R_2^2 \tag{4.2}$$

In this parametrization the metric tensor g_{ij} and Gaussian curvature K are given by:

$$g_{\psi\psi} = R_2^2\,, \qquad g_{\psi\phi} = 0\,, \qquad g_{\phi\phi} = (R_1 + R_2\cos\psi)^2\,, \tag{4.3}$$

$$K = \frac{\cos\psi}{R_2(R_1 + R_2\cos\psi)}\,. \tag{4.4}$$

The Gaussian curvature is therefore positive on the outside of the torus, negative on the inside and zero along the two circles of radius R_1 at $\psi = \pm\pi/2$ (see Fig. 4.2). Moreover K is maximally positive along the external equator at $\psi = 0$ and maximally negative on the internal equator at $\psi = \pm\pi$. The Gauss-Bonnet theorem requires the total topological charge and the integrated Gaussian curvature to be zero on the torus:

$$\sum_{k=1}^{N} q_k = \int d^2x\, K(\boldsymbol{x}) = 0 \tag{4.5}$$

A global measure of the curvature of the embedded torus is provided by the aspect ratio $r = R_1/R_2$. Our discussion will be limited to the case $r \geq 1$. A "fat" torus with $r = 1$ is obtained by taking $R_1 = R_2$ and is characterized by a singularity in the Gaussian curvature along the internal equator at $\psi = \pm\pi$. The case $r < 0$ corresponds to a self-intersecting torus whose symmetry axis lies in the interior of the revolving circle. The "skinny" torus limit, $r \to \infty$, can be obtained either by taking $R_2 \to 0$ with finite R_1 or by letting R_2 stay finite and taking $R_1 \to \infty$. The Gaussian curvature diverges in the first case and goes to zero in the second. Neither case, however, reflects a real physical situation since the area $A = (2\pi)^2 R_1 R_2$ of the torus becomes zero or infinite rispectivelly.

Non-axisymmetric tori can be generated in various ways by deforming the surface of revolution (4.1). A special and physically relevant transformation consists in an inversion at the unit sphere, a translation about a vector $\boldsymbol{\beta}$ and a second inversion. Thus a point $\boldsymbol{R}$ on the surface is mapped onto:

$$\boldsymbol{R}' = \frac{\frac{\boldsymbol{R}}{R^2} + \boldsymbol{\beta}}{|\frac{\boldsymbol{R}}{R^2} + \boldsymbol{\beta}|^2} \tag{4.6}$$

This map is conformal and transforms an axisymmetric shape to a non-axisymmetric one if the vector $\boldsymbol{\beta}$ is not parallel to the symmetry axis [133]. As $\boldsymbol{\beta}$ is increased in magnitude, the asymmetry increases until, in the limit, the torus becomes a perfect sphere with an infinitesimal handle. The physical importance of mapping (4.6) relies on the fact that it leaves the bending energy $\kappa \int d^2x\, H^2$ invariant with significant consequences for the equilibrium shape and stability of fluid toroidal membranes.

As in any closed manifold the traditional Green-Laplace equation doesn't have a solution on the torus. An alternative Green function, can be obtained from the modified equation:

$$\Delta_g G_L(\boldsymbol{x}, \boldsymbol{y}) = \delta_g(\boldsymbol{x}, \boldsymbol{y}) - A^{-1} \tag{4.7}$$

As usual the calculation of the Green function can be simplified considerably by conformally mapping the torus to a domain of the Euclidean plane via a suitable system of isothermal coordinates. Intuitively the torus is conformally equivalent to a rectangular domain described by a system of Cartesian coordinates. To make this explicit, one can equate the metric of the torus in the coordinates (ψ, ϕ) to a conformally Euclidean metric in the coordinates (ξ, η):

$$ds^2 = R_2^2 d\psi^2 + (R_1 + R_2 \cos\psi)^2 d\phi^2 = w\,(d\xi^2 + d\eta^2)\,,$$

where w is a positive conformal factor. Taking $\eta = \phi$ and $w = (R_1 + R_2\cos\psi)^2$, the coordinate ξ is determined by the differential equation:

$$\frac{d\xi}{d\psi} = \pm \frac{1}{r + \cos\psi}\,, \tag{4.8}$$

where $r = R_1/R_2$, the aspect ratio of the torus, may be taken greater or equal to one without loss of generality. Choosing the plus sign and integrating both sides of Eq. (4.8) we find:

$$\xi = \int_0^{\psi} \frac{d\psi'}{r + \cos\psi'}\,. \tag{4.9}$$

Taking $\psi \in [-\pi, \pi)$, the integral (4.9) yields:

$$\xi = \kappa \arctan\left(\omega \tan\frac{\psi}{2}\right)\,,$$

where

$$\kappa = \frac{2}{\sqrt{r^2-1}}\,, \qquad\qquad \omega = \sqrt{\frac{r-1}{r+1}}\,. \tag{4.10}$$

In the transformed coordinate system (ξ, η) the modified Green-Laplace equation reads:

$$\Delta G_L(\boldsymbol{x}, \boldsymbol{y}) = \delta(\boldsymbol{x}, \boldsymbol{y}) - \frac{w}{A}\,, \tag{4.11}$$

where Δ and δ are now the Euclidean Laplacian and delta function. The function $G_L(\boldsymbol{x}, \boldsymbol{y})$ can be expressed in the form:

$$G_L(\boldsymbol{x}, \boldsymbol{y}) = G_0(\boldsymbol{x}, \boldsymbol{y}) - \langle G_0(\boldsymbol{x}, \cdot\,)\rangle - \langle G_0(\cdot\,, \boldsymbol{y})\rangle + \langle G_0(\cdot\,, \cdot\,)\rangle\,,$$

where $G_0(\boldsymbol{x}, \boldsymbol{y})$ is the Laplacian Green function on a periodic rectangle and the angular brackets stand for the normalized integral of the function $G_0(\boldsymbol{x}, \boldsymbol{y})$ with respect to the dotted variable:

$$\langle G_0(\boldsymbol{x}, \cdot\,)\rangle = \int \frac{d^2y}{A}\, G_0(\boldsymbol{x}, \boldsymbol{y})\,. \tag{4.12}$$

Analogously the function $\langle G_0(\cdot\,, \cdot\,)\rangle$ is given by

$$\langle G_0(\cdot\,, \cdot\,)\rangle = \int \frac{d^2x\, d^2y}{A^2}\, G_0(\boldsymbol{x}, \boldsymbol{y})$$

and ensures the neutrality property:

$$\int d^2x\, G_L(\boldsymbol{x}, \boldsymbol{y}) = \int d^2y\, G_L(\boldsymbol{x}, \boldsymbol{y}) = 0\,. \tag{4.13}$$

The modified Laplacian Green function on a periodic rectangle of edges p_1 and p_2 can be conveniently calculated in the form:

$$G_0(\boldsymbol{x}, \boldsymbol{y}) = \sum_{\lambda \neq 0} \frac{u_\lambda(\boldsymbol{x})\overline{u}_\lambda(\boldsymbol{y})}{\lambda}\,, \tag{4.14}$$

where u_λ is the eigenfunction of the Laplace operator with periodic boundary conditions:

$$\Delta u_\lambda(\boldsymbol{x}) = \lambda u_\lambda(\boldsymbol{x})\,, \tag{4.15}$$

such that:

$$\begin{cases} u_\lambda(0,\eta) = u_\lambda(p_1,\eta) \\ u_\lambda(\xi,0) = u_\lambda(\xi,p_2) \end{cases} .$$

In Cartesian coordinates the eigenfunctions are simple plane waves of the form:

$$u_\lambda(\xi,\eta) = \frac{e^{i(\lambda_n\xi+\mu_m\eta)}}{\sqrt{p_1 p_2}} , \tag{4.16}$$

where λ_n and μ_m are given by:

$$\lambda_n = \frac{2\pi n}{p_1} \qquad \mu_m = \frac{2\pi m}{p_2} \qquad n,\, m = 0,\, \pm 1,\, \pm 2 \ldots$$

and the eigenvalue λ is given by:

$$\lambda = -\lambda_n^2 - \mu_m^2 . \tag{4.17}$$

Calling for simplicity $\boldsymbol{x} = (x, y)$ and $\boldsymbol{y} = (\xi, \eta)$, the function G_0 is given by:

$$G_0(\boldsymbol{x},\boldsymbol{y}) = -\frac{1}{p_1 p_2} \sum_{(n,m)\neq(0,0)} \frac{e^{i\lambda_n(x-\xi)} e^{i\mu_m(y-\eta)}}{\lambda_n^2 + \mu_m^2} . \tag{4.18}$$

Summing this series eventually leads to [132]:

$$G_0(\boldsymbol{x},\boldsymbol{y}) = \frac{\log 2}{6\pi} - \frac{1}{2\,p_1 p_2}|y-\eta|^2 + \frac{1}{2\pi}\log\left|\frac{\vartheta_1(\frac{z-\zeta}{p_1/\pi}|\frac{ip_2}{p_1})}{\vartheta_1'^{\frac{1}{3}}(0|\frac{ip_2}{p_1})}\right| , \tag{4.19}$$

where $\vartheta_1(u|\tau)$ is the Jacobi theta function [134, 135] defined as:

$$\vartheta_1(u|\tau) = 2q^{\frac{1}{4}}\sin u \prod_{n=1}^{\infty}\left(1-2q^{2n}\cos 2u + q^{4n}\right)\left(1-q^{2n}\right) , \tag{4.20}$$

with $q = \exp(i\pi\tau)$, $z = x + iy$ and $\zeta = \xi + i\eta$. A step-by-step derivation of Eq. (4.19) is reported in Appendix 4.B.

4.3 Defect-free $p-$atic textures and *genera* transition

There has been much effort in recent years to shed light on possible pathways in the self-assembly of toroidal micelles and vesicles from block copolymer solutions and

other amphiphilic compounds. In particular, the spontaneous formation of structure of genus $g \geq 1$ from preexisting spherical objects, a mechanism which is in common to several different scenarios proposed in the literature, has attracted the most attention and debate because of its exotic character. The simplest question one can ask in this context is whether a vesicle can be energetically favored to change its topology from spherical to toroidal once, the total surface area and therefore the number of constituent molecules in the vesicle, is specified. Evans addressed this problem in 1995 [129] and showed how such a transition between *genera* is indeed possible in fluid membranes and is even enhanced if the membrane is endowed with in-plane orientational order. Although oversimplified if compared to the great complexity of the real self-assembly mechanism, Evans' calculation provides insight into the delicate problem of stability of toroidal vesicles as well as a good starting point for our discussion of order on the torus.

Let θ be the local orientation of a $p-$atic director field on a surface as defined in Sec. 2. A standard orientational order parameter is given by scalar field:

$$\psi(\boldsymbol{x}) = \langle e^{ip\theta(\boldsymbol{x})} \rangle \,, \tag{4.21}$$

where $\langle \cdot \rangle$ deontes a thermal average. The total elastic energy of the vesicle consists of a pure bending term F_b, describing the elasticity of the membrane in the liquid state, and a term F_p associated with the internal $p-$atic order. Thus $F = F_p + F_b$, with:

$$F_p = \int d^2x \, \left(\tau |\psi|^2 + \frac{u}{2} |\psi|^4 + C |(\nabla - ip\boldsymbol{\Omega})\psi|^2 \right) \tag{4.22a}$$

$$F_b = \int d^2x \, \left(2\kappa H^2 + \kappa_g K \right) \tag{4.22b}$$

where κ and κ_g are the bending and Gaussian rigidity respectively[1] and the operator $\nabla - ip\boldsymbol{\Omega}$ is obtained from the covariant derivative of a $p-$atic tensor order parameter

[1]The expression of the bending energy used in Eq. (4.22b) is that originally gave by Helfrich for a membrane with zero pre-existing curvature [136]. Often the equivalent expression $\int d^2x \, (\frac{1}{2}\kappa H^2 + \kappa_g K)$ is found in the literature. In this case, however, the mean curvature H is defined as the sum of the principal curvatures rather than their average.

expressed in a local orthonormal frame as described in Sec. 2.4, with $\boldsymbol{\Omega}$ the covariant vector of Eq. (2.53) that parametrizes the spin-connection. The free energy (4.22a) is invariant under rotations of the local reference frame by an arbitrary angle χ:

$$\psi \to \psi\, e^{ip\chi} \tag{4.23a}$$

$$\Omega_i \to \Omega_i - \partial_i \chi\,, \tag{4.23b}$$

which is a typical gauge transformation. The gradient term in Eq. (4.22a) is the same of Eq. 2.52, upon identifying $K_A = p^2 C$. As observed by Park *et al.* [137], Eq. (4.22a) and (4.22b) closely resemble the Landau-Ginzburg Hamiltonian of a superconductor in an external magnetic field:

$$\mathcal{H} = \int d^3x \left\{ \left| \left(\nabla - \frac{2ie}{\hbar c} \boldsymbol{A} \right) \psi \right|^2 + \tau |\psi|^2 + \frac{u}{2} |\psi|^4 + \frac{1}{8\pi} |\nabla \times \boldsymbol{A} - \boldsymbol{H}|^2 \right\} . \tag{4.24}$$

When exposed to an external magnetic field, a super-conducting material can undergo a second order mean-field transition from a metal to a super-conductor characterized by an Abrikosov lattice of vortices whose density is determined by the temperature and the applied magnetic field $\boldsymbol{H}$. The magnetic field, in particular, is conjugate to the vortex number N_v since:

$$\int d^3x\, \nabla \times \boldsymbol{A} = \phi_0 L N_v\,, \tag{4.25}$$

where L is the length of the sample in the direction of $\boldsymbol{H}$ and $\phi_0 = hc/2e$ is the flux quantum. In this context the vector potential associated with the applied magnetic field is replaced by the covariant vector $\boldsymbol{\Omega}$ whose curl is the Gaussian curvature. Morover, on a closed surface:

$$\int d^2x\, \nabla \times \boldsymbol{\Omega} = \int d^2x\, K = \frac{2\pi}{p} \sum_{i=1}^{N} q_i\,.$$

Thus a $p-$atic phase on a closed $2-$manifold is analogous to an Abrikosov phase with a fixed total vorticity rather than a fixed applied magnetic field.

The transition to an ordered phase in controlled by the parameter τ in Eq. (4.22a). For τ above a critical value τ_c ($\tau_c = 0$ on a flat surface), $\psi = 0$ and the system is in the isotropic phase. In this regime the only contribution to the energy is determined by the shape of the vesicle as expressed by the bending term (4.22b). For $\tau < \tau_c$, on the other hand, the gauge symmetry is spontaneously broken and $\psi \neq 0$, with the exception of a number of isolated defective points. Within a meanfield approach, thermal fluctuations can be neglected and the preferred configuration of the system corresponds to the minimum of the free energy. A ground state configuration for the $p-$atic order parameter can be found by rewriting the gradient energy term in Eq. (4.22a) as:

$$\begin{aligned}\int d^2x\, |(\nabla - ip\mathbf{\Omega})\psi|^2 &= \int dx^1\, dx^2 \sqrt{g}\, D^k\psi\, D_k^*\psi^* \\ &= -\int dx^1\, dx^2\, \psi^* \left(D^k \sqrt{g}\, D_k\right) \psi\,,\end{aligned}$$

with $D_k = \partial_k - ip\Omega_k$, and expressing ψ in the basis of eigenfunctions of the operator in parentheses:

$$\psi = \sum_n a_n \varphi_n \tag{4.26}$$

with φ_n satisfying the Hermitean equation:

$$-\frac{1}{\sqrt{g}}\, D^k \left(\sqrt{g}\, D_k\right) \varphi_n = \frac{4\pi\lambda}{A}\, \varphi_n \tag{4.27}$$

with the normalization condition:

$$\int d^2x\, \varphi_n^* \varphi_m = \frac{A}{4\pi}\, \delta_{nm} \tag{4.28}$$

The complex coefficients a_k are then determined by minimization of the free energy F. The eigenfunctions are sometimes referred to as "Landau levels" and are typically degenerate. If ψ is expandend in this complete set of eigenfunctions then, in meanfield, the partition function is dominated by configurations involving only Landau levels with the lowest eigenvalue λ_0. Taking lowest levels only, the $p-$atic free energy

(4.22a) becomes:

$$F_p = \int d^2x \left[\left(\tau + \frac{4\pi\lambda_0 C}{A} \right) |\psi|^2 + \frac{u}{2}|\psi|^4 \right] \tag{4.29}$$

To find the lowest energy configuration of the field ψ one now has to solve the eigenvalue problem (4.27) to determine the lowest eigenvalue λ_0 and minimize the free energy with respect to the parameters of the linear combination (4.26). Notice that the mean field transition has been lowered form $\tau_c = 0$ to $\tau_c = -4\pi\lambda_0 C/A$. On flat surface $\lambda_0 = 0$, but is finite and positive-definite on a surface with finite Gaussian curvature [129].

For a sphere of unit radius parametrized in standard spherical coordinates (θ, ϕ), the eigenvalue problem (4.27) is solved by $\lambda_0 = p$ and φ_n of the form [138]:

$$\varphi_n = \sqrt{\frac{2p+1}{4\pi(p+n)!(p-n)!}} \sin^{p+n}\left(\frac{\theta}{2}\right) \cos^{p-n}\left(\frac{\theta}{2}\right) e^{in\phi} \tag{4.30}$$

for integer values of n between $-p$ and p. These functions have $2p$ zeros, corresponding to topological defects of unitary charge and winding number $1/p$. Because of the lowest Landau level approximation used to derive Eq. (4.29), eigenfunctions (4.30) are degenerate to quadratic order in ψ. This implies the freedom to place defects anywhere on the sphere with no additional energy cost of order ψ^2. The ψ^4 term, on the other hand, lifts this degeneracy and make the defects repel.

For axisymmetric, tori the eigenvalue problem (4.27) was solved numerically by Evans with the result shown in Fig. 4.3. Eigenvalues are plotted as a function of the aspect ratio r of the torus for various $p-$atic textures labelled p_n with $0 \leq n \leq p$. Eigenfunctions φ_n have $4n$ zeros corresponding to $2n$ disclinations of topological charge $q = 1$ (winding number $1/n$) and $2n$ disclinations of topological charge $q = -1$ (winding number $-1/n$). Except for vector order ($p = 1$), defective configurations are energetically favored for small aspect ratios and the number of disclination pairs increases with r as a consequence of the larger (in magnitude) Gaussian curvature.

Carrying out the integrals in Eq. (4.22a) and (4.22b) in the lowest Landau level approximation, the total elastic free energy of spherical and toroidal vesicles can be

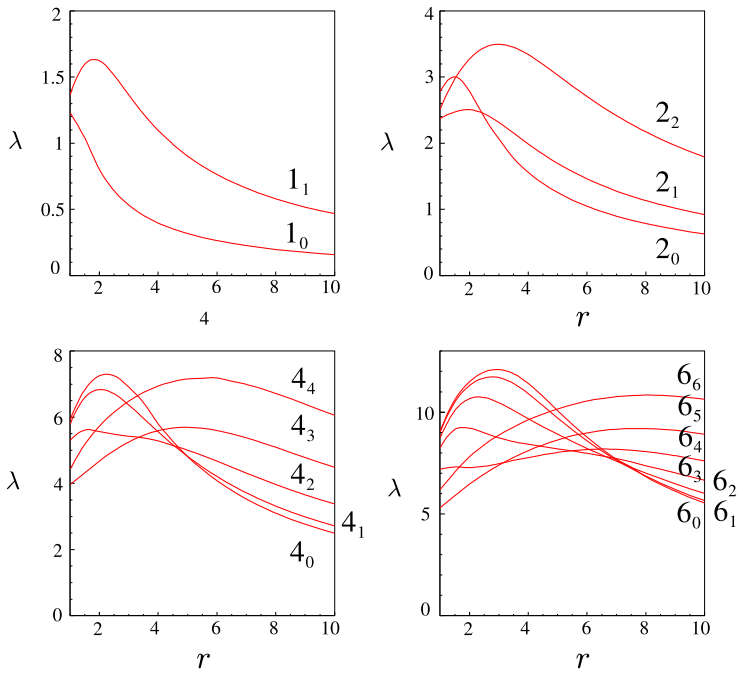

Figure 4.3: (Color online) Eigenvalues λ versus the aspect ratio r for varius $p-$atic configurations (labelled p_n) on the axisymmetric torus. The number of disclination pairs for each configuration is $2n$. Data are taken from [129].

written as:

$$F_{\text{sphere}} = 4\pi(2\kappa + \kappa_g) - 2\pi \left(\frac{C^2}{uA}\right) \frac{\left[\frac{\tau A}{4\pi C} + p\right]^2}{J_{\text{sphere}}(p)} \tag{4.31a}$$

$$F_{\text{torus}} = \kappa \frac{2\pi^2 r^2}{\sqrt{r^2-1}} - 2\pi \left(\frac{C^2}{uA}\right) \frac{\left[\frac{\tau A}{4\pi C} + \lambda_0(r)\right]^2}{J_{\text{torus}}(p,r)} \tag{4.31b}$$

where J is the minimal value of the integral of $|\psi_{\text{MF}}|^4$ and

$$\psi_{\text{MF}} = \begin{cases} \sum_{n=-p}^{p} a_n \varphi_n & \text{sphere} \\ a_+ \varphi_p + a_- \varphi_{-n} & \text{torus} \end{cases}$$

is the linear combination of eigenfuctions that are degenerate to quadratic order in ψ. The second term in Eqs. (4.31a) and (4.31b) disappears in the isotropic phase when $\tau > -4\pi\lambda_0 C/A$ due to the intrinsic orientational order on the manifold. Even in this case, Eqs. (4.31a) and (4.31b) reveal the existence of a transition line

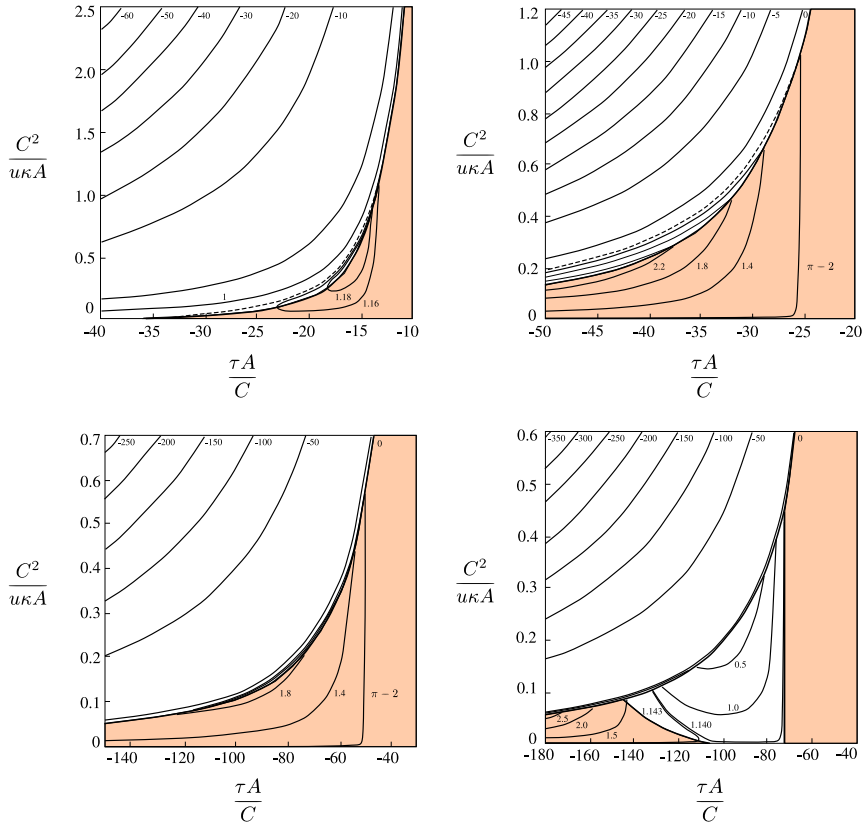

Figure 4.4: (Color online) Phase diagram for vesicles of constant area of genus zero and one with intrinsic vector (top left), nematic (top right), tetradic (bottom left) and hexatic (bottom right) order. The position of the transition line depends on the value of κ_g/κ. Toroidal vesicles that exist in the shaded region are non-axisymmetric. Data are taken from [129].

between spherical and toroidal shape. In the absence of in-plane orientational order the bending energy term in Eq. (4.31b) is minimized by the so called Clifford torus with $r = \sqrt{2}$. In this case $F_{\text{torus}} = 4\pi^2\kappa$, which is smaller than $F_{\text{sphere}} = 4\pi(2\kappa + \kappa_g)$ when $\kappa_g/\kappa > \pi - 2$. Toroidal vesicles with $r = \sqrt{2}$ are therefore energetically favored in the fluid phase for large values of κ_g/κ. This argument cannot be invoked to explain the complex self-assembly of toroidal structures from homogeneous solutions mentioned in the introduction, but does provide a simple (but non-trivial) example of a situation where a toroidal shape is energetically preferred to a spherical one.

The critical value of κ_g/κ of the genera transition is lowered for vesicles equipped

with in-plane $p-$atic order. This is displayed in the phase diagrams of Fig. 4.4 for the case of vector ($p = 1$), nematic ($p = 2$), tetradic ($p = 4$) and hexatic ($p = 6$) order. The lines, whose position depends on κ_g/κ, separate spheres (above the line) from tori (below the line). Even for simple vector order, stable toroidal vesicles exist as well for $\kappa_g/\kappa < \pi - 2$. For $\kappa_g/\kappa > \pi - 2$, furthermore, transition lines are closed, with spheres on the inside and tori on the outside. In the shaded regions non axisymmetric tori are favored over symmetric ones. The hexatic phase diagram (bottom right corner of Fig. 4.4) deserves special attention. The shaded region is split in two parts. That on the right contains spheres if $\kappa_g/\kappa < \pi-2$ and non-axisymmetric tori otherwise, while that on the left contains spheres above the transition line and non-axisymmetric tori below. The white region of the phase diagram is also divided in two parts. The part in the top left of the diagram behaves as described above, while the other part is characterized by closed lines separating spheres (outside) and small tori (inside). These last class of tori exhibit ten pairs of $q = \pm 1$ disclinations with positive disclinations distributed on the external equator of the torus and negative disclinations along the internal equator. This last feature is an important property sheared by toroidal objects with in-plane order and will be clarified in the following sections. The results reviewed here are valid within the mean-field approach and the lowest Landau level approximation, which both hold deep in the ordered phase that we are most interested in. At higher temperatures Evans proved the approximations are still valid away from the transition line and for $C/A \gg \kappa/k_BT \gg 1$ [129]. The latter condition is generally fulfilled by several systems (i.e. $\kappa/k_BT = 1 - 10$ for lipid bilayers).

4.4 Defective ground states in hexatics

Evans' analysis, summarized in the previous section, indicates that disclinations, even if not required by topological constraints, can nonetheless appear in the ground state

of $p-$atic tori as a consequence of the coupling between in-plane orientational order and spatial curvature. The occurrence of defects in the ground state of toroidal hexatic vesicles was systematically investigated by Bowick, Nelson and Travesset based on the formalism outlined in Sec. 2 [130]. Before embarking on a detailed analysis of the elasticity of defects in hexatic tori, it is instructive to obtain a rough estimate of how many pairs of ± 1-disclinations would be required to achieve a perfect screening of the background topological charge associated with the Gaussian curvature of the torus. Consider a wedge of angular width $\Delta\phi$ on the outside wall of positive Gaussian curvature. The net curvature charge associated with this region is:

$$s_{eff} = \int_{\phi_0-\frac{\Delta\phi}{2}}^{\phi_0+\frac{\Delta\phi}{2}} d\phi \int_{-\frac{\pi}{2}}^{\frac{\pi}{2}} d\psi \, \sqrt{g}\, K = 2\Delta\phi \,. \tag{4.32}$$

Upon equating s_{eff} to $2\pi/6$, the charge of a single disclination, one finds that $\Delta\phi = 2\pi/12$, independently of R_1 and R_2. Thus, $2\pi/\Delta\phi = 12$ positive disclinations would be required to completely compensate the negative curvature of the inner wall. This simple argument neglects core energies and interactions between disclinations, effects which will cause the preferred number of defect pairs to be less than twelve.

The total elastic energy of a toroidal hexatic vesicle containing N disclinations of topological charge q_i $(i = 1 \ldots N)$ takes the form:

$$\frac{F}{K_A} = \frac{\pi^2}{9} \sum_{i<j}^{1,N} q_i q_j \mathcal{Q}(\boldsymbol{x}_i, \boldsymbol{x}_j) - \frac{\pi}{3} \sum_{i=1}^{N} q_i \mathcal{L}(\boldsymbol{x}_i) + \frac{2\pi^2}{r + \sqrt{r^2-1}} + \frac{\kappa}{K_A} \frac{2\pi^2 r^2}{\sqrt{r^2-1}} + \frac{\epsilon_c}{K_A} \sum_{i=1}^{N} q_i^2 \tag{4.33}$$

where the first two terms represent the contributions due to the pair interaction between defects and the interaction of defects with the topological charge of the substrate associated with the Gaussian curvature. The third term in Eq. (4.33) is the spin-wave part of the frustrated hexatic energy while the last two terms represents the bending energy and the defect core energy respectively. The defect-defect interaction

potential has been calculated in Ref. [130]:

$$\mathcal{Q}(\boldsymbol{x}_i,\boldsymbol{x}_j) = -\frac{1}{4\pi}\log\frac{\left|\vartheta_1\left(\frac{\phi_i-\phi_j}{2\pi}+\frac{i}{2\pi}\frac{\alpha_i-\alpha_j}{\sqrt{r^2-1}}\middle|\frac{i}{\sqrt{r^2-1}}\right)\right|^2}{4\pi^2\left|\eta\left(\frac{i}{\sqrt{r^2-1}}\right)\right|^6} + \frac{1}{2\sqrt{r^2-1}}\left(\frac{\alpha_i-\alpha_j}{2\pi}\right)^2 \tag{4.34}$$

where α is related to the polar angle ψ on a cross-section of the torus by:

$$\cos\psi = \frac{r\cos\alpha - 1}{r-\cos\alpha} \tag{4.35}$$

and η is the Dedekind eta function:

$$\eta(\tau) = e^{\frac{2\pi i\tau}{24}}\prod_{n=1}^{\infty}(1-e^{2\pi i n\tau})\,. \tag{4.36}$$

The one-body interaction between defects and curvature, on the other hand, is expressed via the potential energy:

$$\mathcal{L}(\boldsymbol{x}_i) = \log\left(\frac{1}{r-\cos\alpha_i}\right)\,. \tag{4.37}$$

For opposite sign disclinations, the defect-defect interaction, determined by the function $\mathcal{Q}(\boldsymbol{x}_i,\boldsymbol{x}_j)$, is attractive for all separations at contrast ϕ. If only this term was present, the attraction would bring both charges as close as possible, binding all dislcinations into dipoles which have a higher energy than a defect-free configuration. Thus if no other terms were present, the ground state configuration would be defect free. The defect-curvature interaction term $\mathcal{L}(\boldsymbol{x}_i)$, however, favors the appearance of additional defects. This term acts like an electric field pulling the positive (negative) disclinations into regions of positive (negative) Gaussian curvature.

The elastic energy (4.33) was analyzed numerically in Ref. [130] for various aspect ratios and defect core energies. A plot of the energy of configurations obtained by placing a ring of $(N/2)$ +1-disclinations equally spaced along the same parallel on the outside of the torus and a second ring of $(N/2)$ −1-disclinations on the inside, is

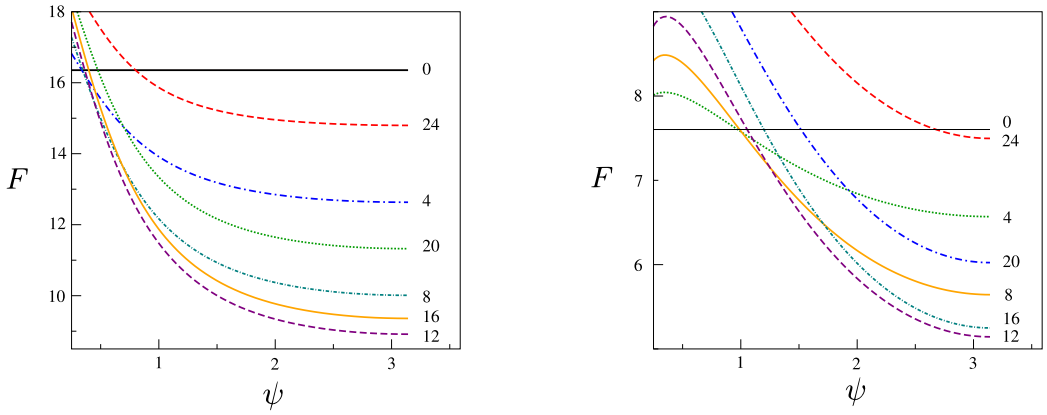

Figure 4.5: (Color online) The total energy (in units of $K_A/2$ of hexatic tori of aspect ratio $r = \sqrt{2}$ (left) and $r = 2.6926$) for varying number of defects. The bending energy at fixed r is subtracted off. The disclination core energy is set to $0.1K_A$, which is 0.2 in the above units.

shown in Fig. 4.5 for various N and variable angular separation $\Delta\psi$ between the rings. The disclination core energy is taken to be $\epsilon_c = cK_A$, with c a numerical constant taken equal to 0.1 in the plots. The energy at the maximum separation ($\Delta\psi = \pi$) first decreases and then increases with N. The optimal number of defect pairs $N/2$ is 6 and 7 (the latter curve is not shown in the plot) for $r = \sqrt{2}$ and $r = 2.6926$ respectively.

The existence of defects in the ground state of a toroidal vesicle with hexatic order is also affected by the total number of molecules $\mathcal{N}$ forming the hexatic phase. In Ref. [130] it was found that defects disappear in the limit $\mathcal{N} \to \infty$, but are present for numbers of molecules as large as $\mathcal{N} = 10^{10}$. This number is several orders of magnitude larger than the typical number of molecules of biological vesicles such as red-blood cells (i.e. $\mathcal{N} \sim 10^8$). To make this estimate, one considers a pair of opposite sign disclinations that have been pulled apart from the circle of zero Gaussian curvature to the equators in the regions of like sign Gaussian curvature; thus $\psi_+ = 0$ and $\psi_- = \pi$. Upon approximating the defect-pair energy by its flat space value, the

total energy reads:

$$F = -\frac{\pi}{3} K_A \log\left(\frac{r+1}{r-1}\right) + \frac{\pi}{18} K_A \log\left(\frac{R_2}{a_0}\right) + 2\epsilon_c \,, \tag{4.38}$$

where a_0 is the lattice spacing. Eq. (4.38) changes sign when

$$\frac{R_2}{a_0} = e^{-\frac{36\epsilon_c}{K_A}} \left(\frac{r+1}{r-1}\right)^6 . \tag{4.39}$$

Taking

$$\mathcal{N} \approx \frac{A}{\frac{\sqrt{3}}{2} a_0^2} = \frac{8\pi^2}{\sqrt{3}\, r \left(\frac{R_2}{a_0}\right)^2}$$

leads to the conclusion that defects are favored for:

$$\mathcal{N} < \frac{8\pi^2}{\sqrt{3}} e^{-\frac{72\epsilon_c}{\pi K_A}} \left[r \left(\frac{r+1}{r-1}\right)^{12} \right] \approx 4.6\, r \left(\frac{r+1}{r-1}\right)^{12} \tag{4.40}$$

where the last identity has been obtained by taking $\epsilon_c/K_A = 0.1$. This result establishes that defects are present in the ground state of a hexatic tours for any fixed number of molecules provided the torus is sufficiently fat. For the energetically favored Clifford torus with $r = \sqrt{2}$, Eq. (4.40) predicts a critical number of molecules to be order $\mathcal{N} \sim 10^{10}$.

In absence of defects the ratio between the hexatic stiffness K_A and the bending rigidity κ dictates the optimal shape of the toroidal vesicle. Taking $q_i = 0$ in Eq. (4.33) one obtains in this case:

$$F = \frac{2\pi^2 K_A}{r + \sqrt{r^2 - 1}} + \kappa \frac{2\pi^2 r^2}{r^2 - 1} \,. \tag{4.41}$$

The first term represents the energetic cost associated with the distortion of the hexatic director field due to the Gaussian curvature alone. In the limit of large and small hexatic stiffness Eq. (4.41) is minimized by:

$$r = \sqrt{2} \qquad K_A \ll \kappa$$

$$r = \sqrt{\tfrac{K_A}{2\kappa}} \qquad K_A \gg \kappa$$

which provides a compelling example of the interplay between order and geometry: if the stiffness associated with the intrinsic hexatic order is much smaller than the bending rigidity, the Clifford torus is the optimal geometry; if on the other hand, the hexatic stiffness dominates, then a thin torus, similar to a bicycle tire, is optimal.

4.5 Toroidal crystals

Crystalline assemblages of identical sub-units packed together and elastically bent in the form of a torus have been found in the past ten years in a variety of systems of surprisingly different nature, such as viral capsids, self-assembled monolayers and carbon nanomaterials. In the introduction we mentioned the self-assembly of toroidal micelles and vesicles from homogeneous solutions of amphiphilic molecules such as oligomers of aromatic compounds or block copolymers. Toroidal geometries also occur in microbiology in the viral capsid of the coronavirus *torovirus* [139]. The torovirus is an RNA viral package of maximal diameter between 120 and 140 nm and is surrounded, as other coronaviridae, by a double wreath/ring of cladding proteins.

Carbon nanotori form another fascinating and technologically promising class of toroidal crystals [48] with remarkable magnetic and electronic properties. The interplay between the ballistic motion of the π electrons and the geometry of the embedding torus leads to a rich variety of quantum mechanical properties including Pauli paramagnetism [140] and Aharonov-Bohm oscillations in the magnetization [141]. Ring closure of carbon nanotubes by chemical methods [142] suggest that nanotubes may be more flexible than at first thought and provides another technique of constructing carbon tori. In this section we review some recent developments in the study of the geometry and the elasticity of toroidal crystals. Additional details can be found in Refs. [131, 132].

4.5.1 Geometry of toroidal polyhedra

Before analyzing the defect distribution arising from the elastic theory, it is necessary to understand the geometry of triangulated tori. Reconciling the predictions of a continuum elastic theory with the intrinsically discrete nature of crystallography requires an understanding of the possible lattices that can be embedded on the torus and the associated defects. The problem of classifying the possible triangulations of the 2−torus has received considerable attention from mathematicians, physicists and chemists over the past twenty years. Lavrenchenko [143] proved in 1984 that all the triangulations of the torus can be generated from 21 irreducible triangulations by certain sequences of operations called vertex splitting[2]. After the discovery of carbon nanotubes in 1991 and the subsequent theoretical construction (later followed by the experimental observation) of graphitic tori, many possible tessellations of the circular torus have been proposed by the community [144–153]. In this section we review the construction of a defect-free triangulated torus and we show how the most symmetric defective triangulations can be generally grouped into two fundamental classes corresponding to symmetry groups D_{nh} and D_{nd} respectively.

For the sake of consistency with the existing literature we adopt here the language developed to describe the structure of carbon nanotubes. The structure of a triangulated cylinder can be specified by a pair of triangular lattice vectors $\boldsymbol{c}$ and $\boldsymbol{t}$, called the *chiral* and *translation* vector respectively, which together define how the planar lattice is rolled up. In the canonical basis $\boldsymbol{a_1} = (1, 0)$ and $\boldsymbol{a}_2 = (\frac{1}{2}, \frac{\sqrt{3}}{2})$, the vector $\boldsymbol{c}$ has the form:

$$\boldsymbol{c} = n\boldsymbol{a}_1 + m\boldsymbol{a}_2 \qquad n,\, m \in \mathbb{Z}\,. \tag{4.42}$$

The translation vector $\boldsymbol{t}$, on the other hand, can be expressed as an integer multiple

$$\boldsymbol{t} = l\boldsymbol{e}_t \qquad l \in \mathbb{Z} \tag{4.43}$$

[2]Analogously it can be proved that the number of irreducible triangulations is one for the sphere and two for the projective plane. The extraordinary larger value obtained for the torus should be indicative of the high structural complexity of a crystalline torus.

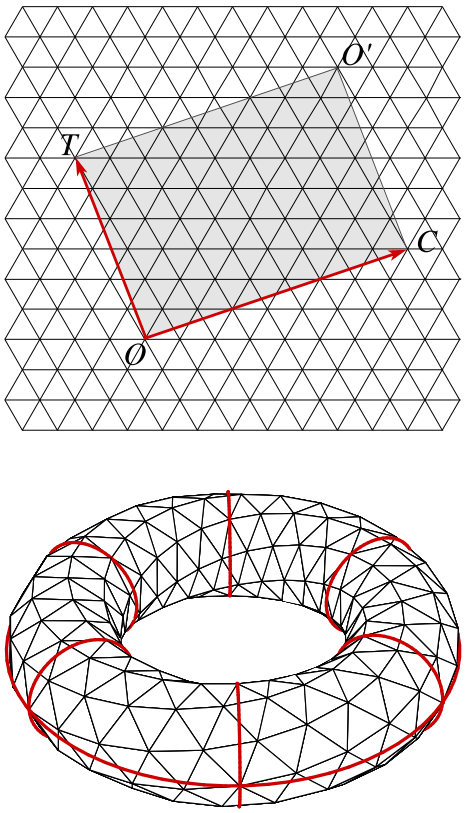

Figure 4.6: (Color online) Construction of a defect-free triangulation of the torus. On top planar map of the triangulated torus corresponding to the (n, m, l) configuration $(6, 3, 1)$. On the bottom $(6, 3, 6)$ chiral torus. The edges of each one of the six tubular segments has been highlighted in red.

of the shortest lattice vector $\boldsymbol{e}_t$ perpendicular to $\boldsymbol{c}$. The vector $\boldsymbol{e}_t$ is readily found to be of the form:

$$\boldsymbol{e}_t = \frac{(n+2m)\boldsymbol{a}_1 - (2n+m)\boldsymbol{a}_2}{(n+2m : 2n+m)}\,,$$

where $(a : b)$ denotes the greatest common divisor of a and b and enforces the minimal length. The three-dimensional structure of the torus is obtained by connecting the edge $\overline{OT}$ of the rectangle in Fig. 4.6 (top) to $\overline{O'C}$ and $\overline{OC}$ to $\overline{O'T}$. The edge $\overline{OT}$ is then mapped to the external equator of the torus while the edge $\overline{OC}$ to the $\phi = 0$ meridian. The resultant toroidal lattice has characteristic chirality related to the initial choice of the vector $\boldsymbol{c}$. In the nanotubes literature *armchair* referes to the lattice obtained by choosing $n = m$, *zigzag* to that obtained for $m = 0$ and *chiral* to all other lattices. An example of a (n, m, l) chiral torus is shown in Fig. 4.6 (bottom) for the case $n = 6$, $m = 3$ and $l = 6$. The chirality is extremely important in graphitic carbon nanotube or nanotori, where it determines whether the electronic behavior of the system is metallic or semiconducting.

By Euler's theorem one can prove that the number of triangular faces F and the number of vertices V of a triangular toroidal lattice is given by:

$$V = \tfrac{1}{2}F\,.$$

Denoting A_R the area of the rectangle with edges $\boldsymbol{c}$ and $\boldsymbol{t}$ and A_T the area of a fundamental equilateral triangle, the number of vertices of a defect-free toroidal triangulation is then:

$$V = \frac{A_R}{2A_T} = \frac{2l\,(n^2+nm+m^2)}{(n+2m : 2n+m)}\,. \tag{4.44}$$

The planar construction reviewed above allows only lattices with an even number of vertices. Defect-free toroidal deltahedra with an odd number of vertices are also possible and their construction is generally achieved by assembling congruent octahedral building blocks. An example of this scheme will be briefly discussed in Sec. 4 for the case $V = 87$ and $r = 6$. We refer the reader to Ref. [154] for an comprehensive review of the topic.

The embedding of an equal number of pentagonal and heptagonal disclinations in the hexagonal network was first proposed by Dunlap in 1992 as a possible way to incorporate positive and negative Gaussian curvature into the cylindrical geometry of carbon tubules [144]. According to the Dunlap construction the necessary curvature is incorporated by the insertion of "knees" (straight cylindrical sections of the same diameter joined with a kink) in correspondence with each pentagon-heptagon pair arising from the junction of tubular segments of different chirality (see Fig. 4.8). In

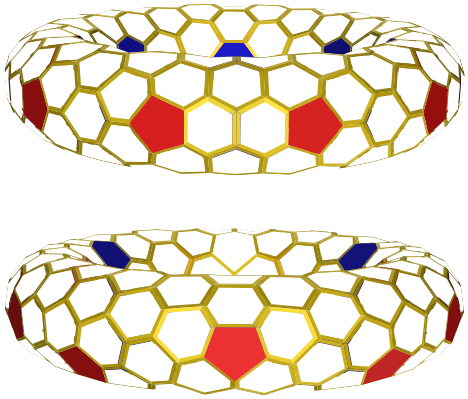

Figure 4.7: (Color online) Voronoi lattices of a TPn prismatic (top) and TAn antiprismatic (bottom) toroids with $R_1 = 1$ and $R_2 = 0.3$.

particular, a junction between a $(n, 0)$ and a (m, m) tube can be obtained by placing a 7−fold disclination along the internal equator of the torus and a 5−fold disclination along the external equator. Since the radii of the two segments of a junction are different by construction, the values of n and m are commonly chosen to minimize the ratio $|\boldsymbol{c}_{(n,0)}|/|\boldsymbol{c}_{(m,m)}| = n/\sqrt{3}m$. By repeating the $5-7$ construction periodically it is possible to construct an infinite number of toroidal lattices with an even number of disclinations pairs and dihedral symmetry group D_{nh} (where $2n$ is the total number of $5-7$ pairs, Fig 4.9). The structure of the lattice is described by the alternation of two motifs with crystalline axes mutually rotated by 30° as a consequence of the connecting disclination. One of the fundamental aspects of Dunlap's construction is that all the disclinations are aligned along the two equators of the torus where the

like-sign Gaussian curvature is maximal. As we will see below, this feature makes these arrangements optimal in releasing the elastic stress due to curvature.

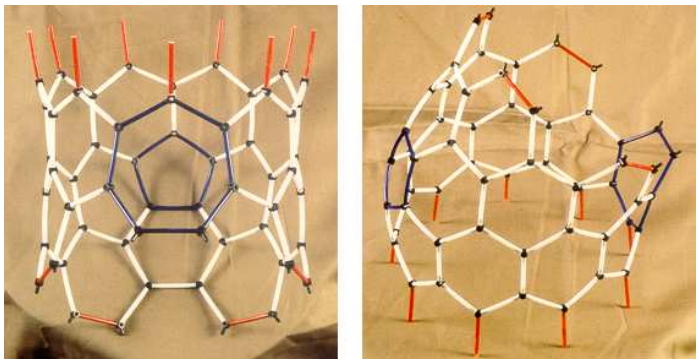

Figure 4.8: (Color online) Dunlap knees obtained by joining two straight tubular segments with $(n, 0)$ and (m, m) chirality. [Courtesy of A. A. Lucas and A. Fonseca, Facultés Universitaries Notre-Dame de la Paix, Namur, Belgium].

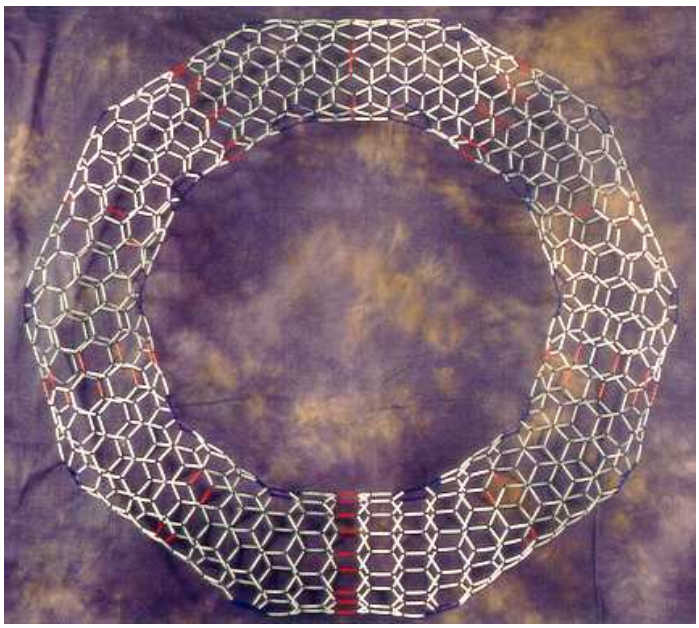

Figure 4.9: (Color online) Five-fold polygonal torus obtained by joining $(5, 5)$ and $(9, 0)$ tubular segments via ten pairs of $5 - 7$ rings. This structure was originally proposed by the authors of Ref. [155] as a possible low-strain configuration for carbon nanotori. [Courtesy of A. A. Lucas and A. Fonseca, Facultés Universitaries Notre-Dame de la Paix, Namur, Belgium].

Another class of crystalline tori with dihedral antiprismatic symmetry D_{nd} was initially proposed by Itoh *et al* [145, 151, 152] shortly after Dunlap. Aimed at reproducing a structure similar to the C_{60} fullerene, Itoh's original construction implied ten disclination pairs and the point group D_{5d}. In contrast to Dunlap tori, disclinations are never aligned along the equators in antiprismatic tori, instead being staggered at some angular distance $\delta\psi$ from the equatorial plane. Hereafter we will use the symbol TAn to refer to toroidal deltahedra with $2n$ disclination pairs and D_{nd} symmetry group.

A systematic construction of defected triangulations of the torus can be achieved in the context of planar graphs [143, 156, 157]. A topological embedding of a graph in a two-dimensional manifold corresponds to a triangulation of the manifold if each region of the graph is bounded by exactly three vertices and three edges, and any two regions have either one common vertex or one common edge or no common elements of the graph. The simplest example of toroidal polyhedra with D_{nd} symmetry group, featuring only $5-$fold and $7-$fold vertices, can be constructed by repeating n times the unit cell of Fig. 4.11a. These *toroidal antiprisms* [3] have $V = 4n$ vertices and can be obtained equivalently from the edge skeleton of a $n-$fold antiprism by attaching at each of the base edges a pentagonal pyramid and by closing the upper part of the polyhedron with n additional triangles. By counting the faces one finds $F = 5n + 2n + n = 8n$ from which $V = 4n$. The simplest polyhedron of this family has $V = 12$ and D_{3d} symmetry group (see top left of Fig. 4.10) and corresponds to the "drilled icosahedron" obtained by removing two parallel faces of an icosahedron and connecting the corresponding edges with the six lateral faces of an antiprism with triangular base (i.e. a prolate octahedron). Starting from this family of toroidal antiprisms a number of associated triangulations having the same defect structure can be obtained by geometrical transformations such as the Goldberg inclusion [38,

[3] Although we presume this class of toroidal polyhedra is not discussed here for the first time, we couldn't find any previous reference in the literature.

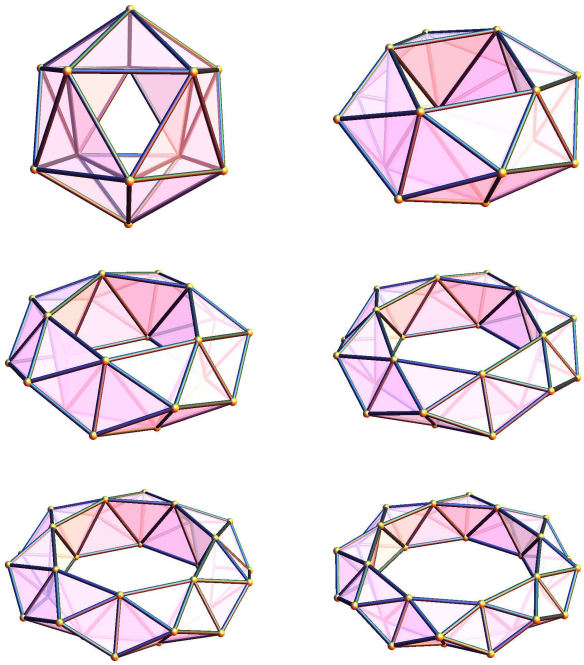

Figure 4.10: (Color online) First six toroidal antiprisms obtained by repeating the unit cell of Fig. 4.11. The first polyhedron on the left is the "drilled icosahedron".

158, 159]. Such transformations, popularized by Caspar and Klug for the construction of the icosadeltahedral structure of spherical viruses [38], consist in partitioning each triangular face of the original graph into smaller triangular faces in such a way that old vertices preserve their valence and new vertices have valence six. The partition is obtained by specifying two integer numbers (L, M) which define how the original vertices of each triangle are connected by the new edges so that the total number of vertices is increased by a factor $T = L^2 + LM + M^2$.

A general classification scheme for D_{nd} symmetric tori was provided by Berger and Avron [156, 157] in 1995. Their scheme is based on the construction of unit graphs comprising triangular tiles of different *generations*. In each generation, tiles are scaled in length by a factor $1/\sqrt{2}$ with respect to the previous generation. This rescaling approximates the non-uniformity of the metric of a circular torus.

Dunlap toroids can be obtained from unit cells such as those shown in Fig. 4.12.

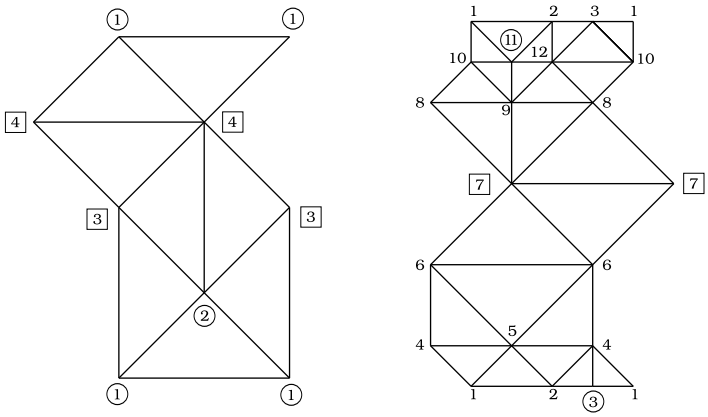

Figure 4.11: (a) Unit cell for toroidal antiprisms. 5−fold vertices are circled and 7−fold vertices are boxed. (b) Unit cell of a D_{nd} torus in the Berger-Avron construction. The graph consists of four generation of tiles and the internal equator of the torus is mapped into the horizontal line passing to the mid-point between the 6th and the 7th vertex.

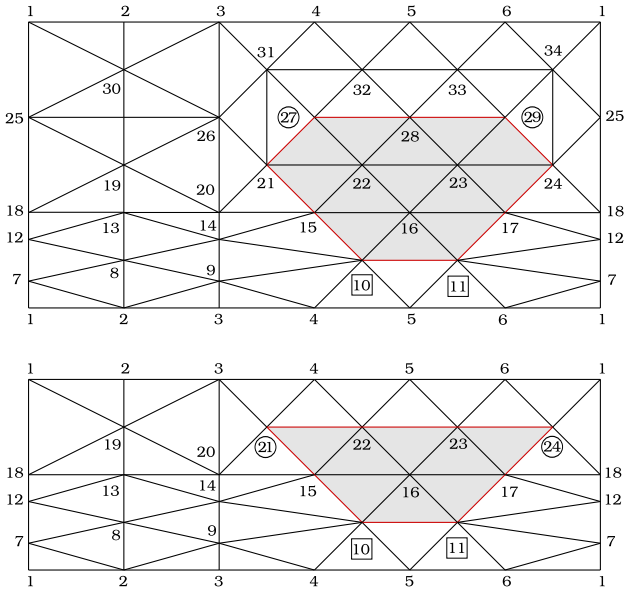

Figure 4.12: (Color online) Unit cells for Dunlap toroids of type $(2,1,3,1)$ and $(3,1,3,1)$ according to the classification scheme given here. Highlighted regions correspond to the central polygon.

The geometrical properties of these graphs can be described in different ways. A particularly intuitive way, in the spirit of this work, consists in specifying the distances

between 5− and 7−fold pairs. One starts by drawing the smallest convex loop passing through defective sites. This identifies a central polygon whose upper vertices (v_1 and v_2 in Fig.4.13) have degree five and lower vertices (v_5 and v_6 in Fig. 4.13) have degree seven. Then calling a the distance between 5−fold vertices v_1 and v_2, b that between 7−fold vertices v_5 and v_6 and c the length of the segment $\overline{v_3 v_4}$ ($d = a$ for a trapezoid), we can express the total number of triangles enclosed by the central polygon as:

$$f = 2c^2 - a^2 - b^2 \,.$$

Each 7−fold vertex sits at the apex of a diamond-shaped complex of $f' = 7$ triangles. Each 5−fold vertex, on the other hand, is at the apex of a triangular region of $f'' = (c - a + 1)^2$ triangles. The graph is completed by a rectangle of height $c - a + 4$ and base of arbitrary length $2d$ containing:

$$f''' = 4d(c - a + 4)$$

triangles. The total number of vertices is

$$\begin{aligned} V_g &= f + f' + f'' + f'''/2 \\ &= c^2 - b^2 + 2(c - a)(c + d + 1) + 8(d + 1) \,. \end{aligned} \tag{4.45}$$

The final triangulation of the torus is obtained by repeating the prismatic unit cell l times and therefore has $V = lV_g$ vertices. This scheme provides direct information on the arrangement of defective sites. Thus for instance an $(a, b, c, d) = (2, 1, 3, 1)$ unit cell (see top of Fig. 4.12) has 5−fold vertices separated by two lattice spacings and 7−fold vertices by one lattice spacing. On the other hand the integers n and m giving the chirality of the two segments of the junction $(n, 0)/(m, m)$ are given directly by as:

$$\begin{aligned} n &= c - a + 4 \\ m &= 2c - a - b \,. \end{aligned}$$

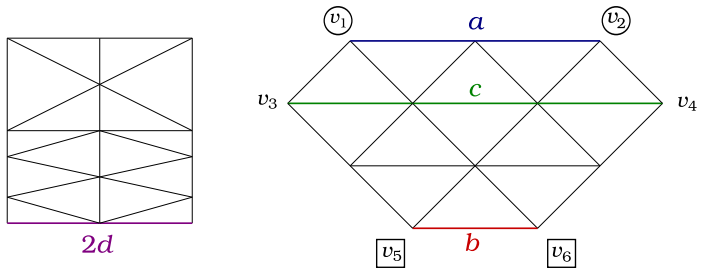

Figure 4.13: (Color online) Central polygon (right) and rectangular (zig-zag) region in our construction scheme of Dunlap's toroids. In this example $(a, b, c, d) = (2, 1, 3, 1)$.

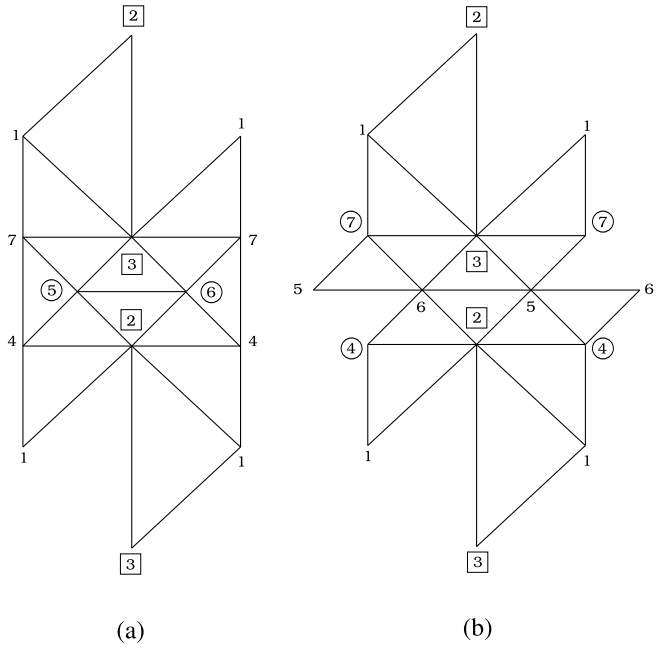

Figure 4.14: Unit cells for TP(2)n and TP(3)n toroids.

Thus the $(2, 1, 3, 1)$ cell of Fig. 4.12 is obtained from the junction between a $(5, 0)$ and a $(3, 3)$ tubular segment.

Dunlap's toroids are not the only examples of defective triangulations of the torus with dihedral prismatic symmetry group D_{nh}. With the help of numerical simulations (see Sec. 4) we found two other classes whose unit cell is shown in Fig. 4.14. Unlike Dunlap's toroids, the 7−fold vertices in these prismatic triangulations are not aligned along the internal equator of the torus, but rather grouped in dimers normal to the

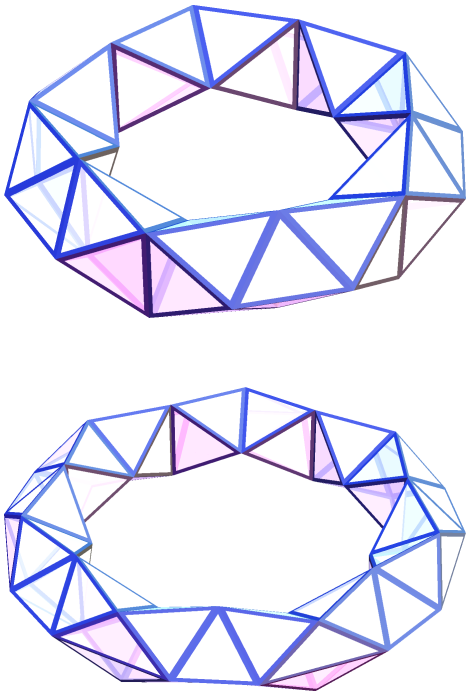

Figure 4.15: (Color online) (a) TP5a and (b) TP7b toroids with $V = 35$ and 49 obtained by repeating the unit cells of Fig. 4.14. 7−fold vertices form dimers normal to the equatorial plane while 5−fold vertices are (a) distributed along the external equator or (b) form a double ring above and below the equatorial plane.

equatorial plane. 5−fold vertices are distributed along the external equator in the graph of Fig. 4.14a or form a double ring above and below it in the case of the graph Fig. 4.14b. Toroidal deltahedra obtained by embedding the prismatic graphs of Fig. 4.14 on a circular torus are shown in Fig. 4.15 for the case of a 5−fold symmetric toroid with $V = 35$ and a 7−fold symmetric toroid with $V = 49$. In the rest of the paper we will reserve the symbol TPn for Dunalp's toroids and refer with TPna and TPnb to the other two classes of toroids with symmetry group D_{nh} and unit cell of as shown in Fig. 4.14a and Fig. 4.14b respectively.

All defective triangulations presented so far are characterized by an even number of disclination pairs. Regular tessellations of the torus comprising an odd number of defects pairs are also possible. Such tessellations are obtained by combining segments

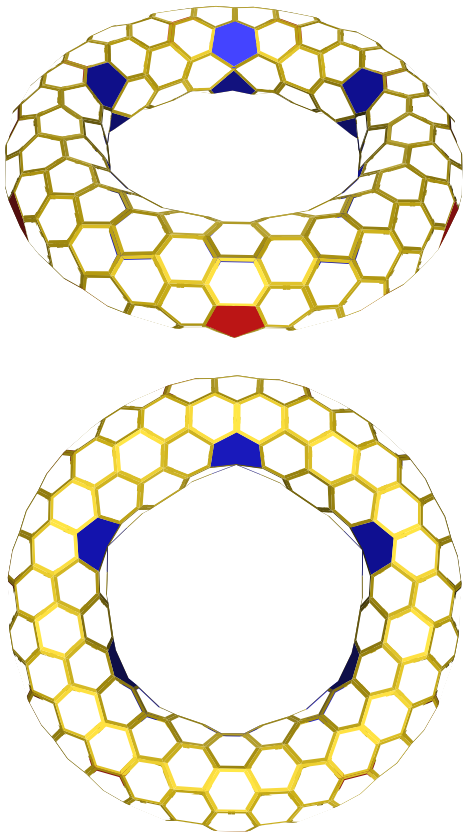

Figure 4.16: (Color online) Voronoi diagram of a toroidal lattice with $r = 10/3$ and $V = 200$ vertices. The lattice exhibits 11 disclination pairs and has C_s symmetry group.

of prismatic and antiprismatic lattices with a consequent loss of dihedral symmetry. Fig. 4.16 shows the Voronoi diagram of a toroidal lattice, with $r = 10/3$ and $V = 200$ vertices, containing 11 disclination pairs. For an angular length of approximately $\Delta\phi = 7/5\,\pi$ the lattice is a prismatic D_{5d} toroid while in the remaining $3/5\,\pi$ the local structure is that of an antiprismatic toroid. The global structure has only bilateral symmetry about a sagittal plane dividing the lattice in two mirror halves and thus point group C_s.

In the past few years, alternative constructions of triangulated tori have been proposed as well as novel geometrical and graph-theoretical methods to express the coordinates of their three-dimensional structures (see for example Kirby [146], László

at al [147, 153, 160], Diudea *et al* [148, 161]). Here we choose to focus on the defect structure associated with the two most important class TPn and TAn with groups D_{nh} and D_{nd}.

4.5.2 Elasticity of defects on the torus

Isolated defects regime

The total free energy of a toroidal crystal with N disclinations can be expressed as usual as:

$$F = \frac{1}{2Y}\int d^2x\,\Gamma^2(\boldsymbol{x}) + \epsilon_c \sum_{i=1}^{N} q_i^2 + F_0 \tag{4.46}$$

where Y is the two dimensional Young modulus and:

$$\Gamma(\boldsymbol{x}) = \frac{\pi}{3}\sum_{k=1}^{N} q_k \Gamma_d(\boldsymbol{x},\boldsymbol{x}_k) - \Gamma_s(\boldsymbol{x})\,, \tag{4.47}$$

The defect part of the stress function $\Gamma(\boldsymbol{x})$ can be found by integrating the Green function (4.19) and takes the form:

$$\begin{aligned}\frac{\Gamma_d(\boldsymbol{x},\boldsymbol{x}_k)}{Y} = \frac{\kappa}{16\pi^2}\left(\psi_k - \frac{2}{\kappa}\,\xi_k\right)^2 - \frac{1}{4\pi^2\kappa}(\phi-\phi_k)^2 + \frac{1}{4\pi^2 r}\log(r+\cos\psi_k) \\ - \frac{\kappa}{4\pi^2}\,\mathrm{Re}\{\mathrm{Li}_2(\alpha e^{i\psi_k})\} + \frac{1}{2\pi}\log\left|\vartheta_1\left(\frac{z-z_k}{\kappa}\middle|\frac{2i}{\kappa}\right)\right|\,,\end{aligned} \tag{4.48}$$

where Li_2 is the usual Eulerian dilogarithm and

$$\alpha = \sqrt{r^2-1} - r\,. \tag{4.49}$$

The function $\Gamma_s(\boldsymbol{x})$ representing the stress field due to the Gaussian curvature of the torus, on the other hand, is given by:

$$\frac{\Gamma_s(\boldsymbol{x})}{Y} = \log\left[\frac{r+\sqrt{r^2-1}}{2(r+\cos\psi)}\right] + \frac{r-\sqrt{r^2-1}}{r}\,. \tag{4.50}$$

A derivation of the functions $\Gamma_d(\boldsymbol{x},\boldsymbol{x}_k)$ and $\Gamma_s(\boldsymbol{x})$ will be given in Appendices 4.C, 4.D and 4.E.

To analyze the elastic free energy (4.46) we start by considering the energies of two opposite sign disclinations constrained to lie on the same meridian. The elastic free energy of this system is shown in Fig. 4.17 as a function of the angular separation between the two disclinations. The energy is minimized for the positive (5−fold) disclination on the external equator (maximally positive Gaussian curvature) and the negative (7−fold) disclination on the internal equator (maximally negative Gaussian curvature). The picture emerging from this simple test case suggests that a good *ansatz* for an optimal defect pattern is a certain number p of equally spaced $+1$ disclinations on the external equator matched by the same number of equally spaced -1 disclinations on the internal equator. We name this configuration with the symbol T_p, where p stands for the total number of disclination pairs.

$$T_p: \quad \left\{ \left(0, \frac{2\pi k}{p}\right)_{1\le k\le p} ; \left(\pi, \frac{2\pi k}{p}\right)_{1\le k\le p} \right\} , \tag{4.51}$$

where the two pairs of numbers specify the (ψ, ϕ) coordinates of the positive and negative disclinations respectively. A comparison of the energy of different T_p configurations, as a function of aspect ratio and disclination core energy, is summarized in the phase diagram of Fig. 4.18. We stress here that only T_p configurations with p even have an embedding on the torus corresponding to lattices of the $\mathrm{TP}\frac{p}{2}$ class. Nevertheless a comparison with $p-$odd configurations can provide additional information on the stability of $p-$even lattices. For small core energies, moreover, thermally excited configurations with a large number of defects and similar $p-$polar distributions of topological charge are expected to exhibit an elastic energy comparable in magnitude with that of these minimal constructions. The defect core energy has been expressed here in the form:

$$F_c = \epsilon_c \sum_{i=1}^{2p} q_i^2 = 2p\epsilon_c \ . \tag{4.52}$$

The core energy ϵ_c of a single disclination depends on the details of the crystal-forming material and the corresponding microscopic interactions. A simple phenomenological

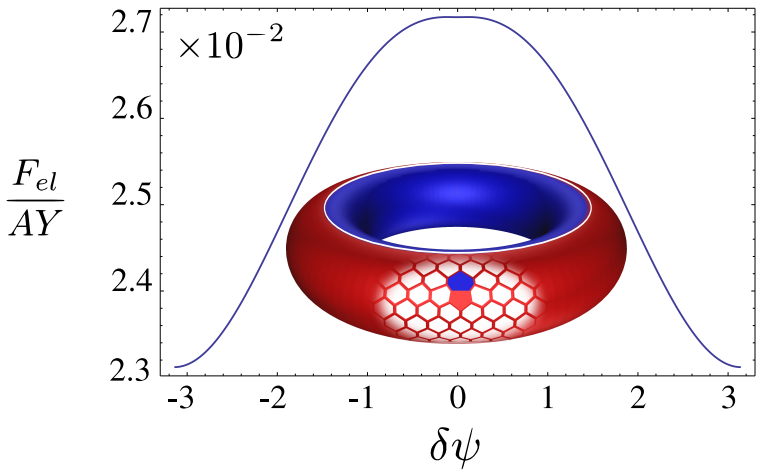

Figure 4.17: (Color online) Elastic energy of a $5-7$ disclination dipole constrained to lie on the same meridian, as a function of the angular separation. In the inset, illustration of a circular torus of radii $R_1 > R_2$. Regions of positive and negative Gaussian curvature have been shaded in red and blue respectively.

argument (see for example Ref. [162]) gives

$$\frac{\epsilon_c}{Y} \sim \frac{a^2}{32\pi} \,,$$

where a the lattice spacing. Taking $a^2 = A/\frac{\sqrt{3}}{2}V$, with A the area of the torus, yields:

$$\frac{\epsilon_c}{AY} \sim \frac{1}{16\sqrt{3}\,\pi V} \sim \frac{10^{-2}}{V} \,. \tag{4.53}$$

For a system of order $V = 10^3$ subunits, then, the dimensionless core energy on the left hand side of Eq. (4.53) is of order 10^{-5}. This estimate motivates our choice of the scale for $\epsilon_c/(AY)$ in Fig. 4.18.

For dimensionless core energies below $4 \cdot 10^{-5}$ and aspect ratios r between 3.68 and 10.12 the ground state structure is the TP5 lattice corresponding to a double ring of $+1$ and -1 disclinations distributed on the external and internal equators of the torus as the vertices of a regular decagon (the T_{10} configuration). The TP5 lattice has dihedral symmetry group D_{5h}. That this structure might represent a stable configuration for polygonal carbon toroids has been conjectured by the authors of

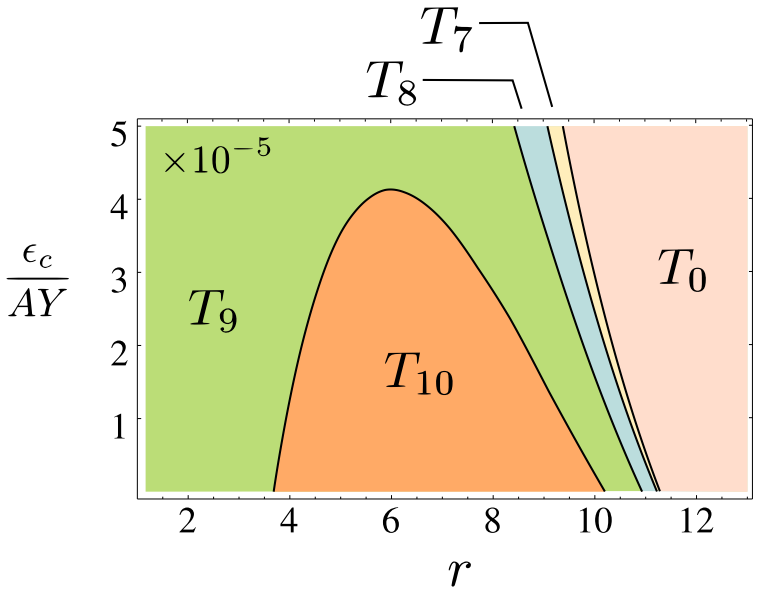

Figure 4.18: (Color online) Phase diagram for T_p configurations in the plane $(r, \epsilon_c/AY)$. For $r \in [3.68, 10.12]$ and $\epsilon_c \sim 0$ the structure is given by a T_{10} configuration with symmetry group D_{5h}.

Ref. [155], based on the argument that the 36° angle arising from the insertion of ten pentagonal-heptagonal pairs into the lattice would optimize the geometry of a nanotorus consistently with the structure of the sp^2 bonds of the carbon network (unlike the 30° angle of the 6−fold symmetric configuration originally proposed by Dunlap). In later molecular dynamics simulations, Han [163, 164] found that a 5−fold symmetric lattice, such as the one obtained from a (9,0)/(5,5) junction (see Fig. 4.9), is in fact stable for toroids with aspect ratio less then $r \sim 10$. The stability, in this case, results from the strain energy per atom being smaller than the binding energy of carbon atoms. Irrespective of the direct experimental observation of such disclinated toroidal crystals, which is still open, we show here how continuum elasticity predicts that a 5−fold symmetric lattice indeed constitutes a minimum of the elastic energy for a broad range of aspect ratios and defect core energies.

For small aspect ratios the 5−fold symmetric configuration becomes unstable and is replaced by the 9−fold symmetric phase T_9. As we mentioned, however, this configuration doesn't correspond to a possible triangulation of the torus. It is likely

that the ground sate in this regime consists of ten skew disclination pairs as in the antiprismatic TAn lattice. The latter can be described by introducing a further degree of freedom $\delta\psi$ representing the angular displacement of defects from the equatorial plane:

$$\mathrm{TA}n: \quad \left\{ \left((-1)^{2k}\delta\psi, \frac{2\pi k}{n} \right)_{1\le k\le n} ; \left((-1)^{2k}(\pi-\delta\psi), \frac{2\pi k}{n} \right)_{1\le k\le n} \right\} \tag{4.54}$$

A comparison of the TP5 configuration and the TA5 configuration is shown in Fig. 4.19 for different values of $\delta\psi$. The intersection points of the boundary curves with the $\delta\psi-$axis has been calculated by extrapolating the $(r, \delta\psi)$ data points in the range $\delta \in [0.07, 0.8]$ with $\Delta(\delta\psi) = 2.5\pi \cdot 10^{-3}$. For small $\delta\psi$ and $r \in [3.3, 7.5]$ the prismatic TP5 configuration is energetically favored. For $r < 3.3$, however, the lattice undergoes a structural transition to the TA5 phase. For $r > 7.5$ the prismatic symmetry of the TP5 configuration breaks down again. In this regime, however, the elastic energy of both configurations rapidly rises because of the lower curvature and defects disappear.

Defect free tori

For aspect ratio $r \gtrsim 11$ the TP5 phase is replaced by a defect free configuration (T_0 in Fig. 4.18) so that configurations with defects are no longer energy minima. Any toroidal crystal with aspect ratio larger than ~ 11 is than energetically favored to be defect-free. In the thin torus limit the ground state structure is directly related to the simple problem of finding the most efficient packing of congruent equilateral triangles on the torus of a given aspect ratio. Given V subunits (vertices) one seeks the densest packing of equilateral triangles of edge-length $a = (A/\frac{\sqrt{3}}{2}V)^{1/2}$ on the torus with aspect ratio r, such that each vertex has valence six. Using the planar construction described in §4.5.1, the optimal choice of the indices (n, m, l), can be translated into the minimization of the following quantity:

$$\Delta^{n,m}(r, V) = n^2 + nm + m^2 - \tfrac{\sqrt{3}}{2}\, r^{-1} V\,, \tag{4.55}$$

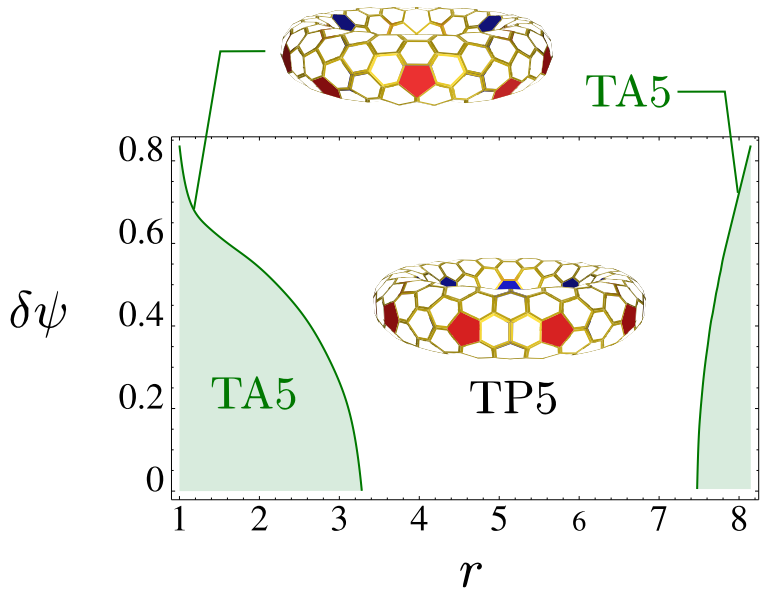

Figure 4.19: (Color online) Phase diagram of a 5−fold symmetric lattice in the plane $(r, \delta\psi)$. For small $\delta\psi$ and r in the range [3.3, 7.5] the prismatic TP5 configuration is energetically favored. For $r < 3.3$ the system undergoes a structural transition to the antiprismatic phase TA5.

obtained by equating the magnitude of the chiral vector $\boldsymbol{c}$ with that of the sectional circumference of the embedding torus, under the constraints:

$$\begin{cases} l = \frac{V}{2}\frac{(n+2m:2n+m)}{n^2+nm+m^2} \\ \\ n,\, m,\, l \in \mathbb{Z} \end{cases} . \tag{4.56}$$

This construction successfully predicts the structure of the lattices of Fig. 4.20.

So far we have studied the elasticity of toroidal crystals exclusively in terms of interacting topological defects on a rigid toroidal substrate. Thus the elastic strain due to defects and curvature takes the form of pure stretching on the tangent plane of the torus and no out-of-plane deformation takes place. In a more realistic scenario, a crystalline torus would undergo both in-plane stretching and out-of-plane bending. The latter implies an energy cost:

$$F_b = \frac{\kappa_b}{2}\int d^2x\, H^2(\boldsymbol{x}) = \kappa_b \frac{2\pi^2 r^2}{\sqrt{r^2-1}}\ , \tag{4.57}$$

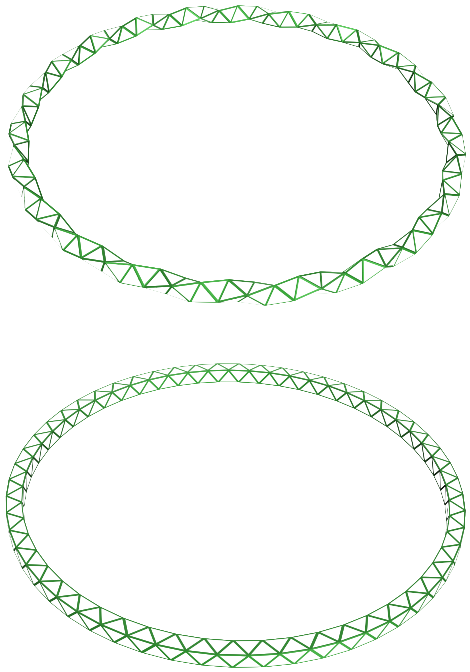

Figure 4.20: (Color online) Two examples of defect free "crop circle" toroids with $r = 20$ and $V = 180$ (left) and 220 (right).

with H the mean curvature (see Ref. [130]). The case of defect-free tori is simple enough to incorporate bending in the problem and see what the optimal aspect ratio of a defect-free torus would be as a function of the Föppl-von Kármán number $\gamma = AY/\kappa_b$ representing the ratio of the stretching energy scale to the bending rigidity. In absence of defects the only source of stress is given by the curvature. Thus

$$F_s = \frac{1}{2Y}\int d^2x\,\Gamma_s^2(\boldsymbol{x}) = AY\Big\{\frac{1+4r(r^2-1)^{\frac{1}{2}}[1-\log(2+2r\alpha)]}{2r^2} + \mathrm{Li}_2(\alpha^2) - 2\Big\}\,.$$

Summing Eq. (4.57) and (4.58) and taking the derivative with respect to r (assuming constant area), one obtains the following equation for the optimal value of r:

$$2\pi^2\frac{r(r^2-2)}{(r^2-1)^{\frac{3}{2}}} - \frac{\gamma}{r^3}\Big[1+2r\alpha-2r(r^2-1)^{\frac{1}{2}}\log(2+2r\alpha)\Big] = 0\,. \qquad (4.58)$$

The optimal aspect ratio r as obtained form Eq. (4.58) is shown in Fig. 4.21 as a function of γ. For $\gamma \sim 0$, when the major contribution to the elastic energy is given

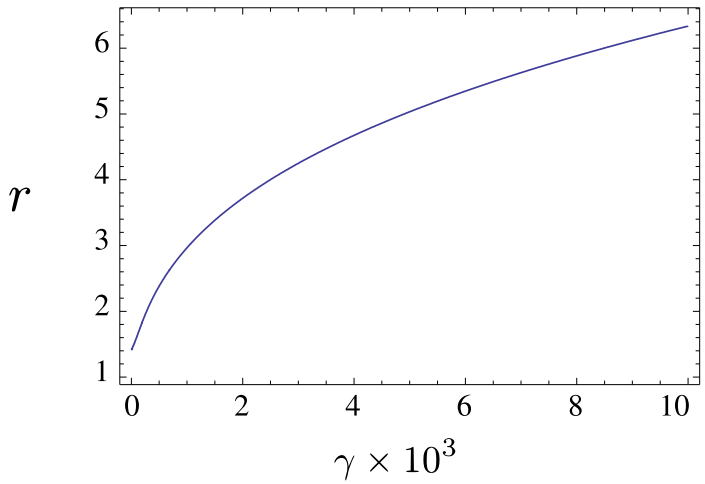

Figure 4.21: (Color online) Optimal value of the aspect ratio r as function of the Föppl-von Kármán number $\gamma = AY/\kappa_b$. For $\gamma \sim 0$ the Clifford torus with $r = \sqrt{2}$ is optimal. Larger values of γ favour instead a "skinnier" torus.

by the bending, the optimal geometry is given by the Clifford torus ($r = \sqrt{2}$). If, on the other hand, the in-plane stretching dominates, a "skinny" torus (large r) is energetically favoured.

Scars and coexistence

In the regime of large particle numbers, the amount of curvature required to screen the stress field of an isolated disclination in units of lattice spacing becomes too large and disclinations are unstable to grain boundary "scars" consisting of a linear array of tightly bound $5-7$ pairs radiating from an unpaired disclination [72, 106]. In a manifold with variable Gaussian curvature this effects leads to a regime of coexistence of isolated disclinations (in regions of large curvature) and scars. In the case of the torus the Gaussian curvature inside ($|\psi| > \pi/2$) is always larger in magnitude than that outside ($|\psi| < \pi/2$) for any aspect ratio and so we may expect a regime in which the negative internal curvature is still large enough to support the existence of isolated $7-$fold disclinations, while on the exterior of the torus disclinations are delocalized in the form of positively charged grain boundary scars.

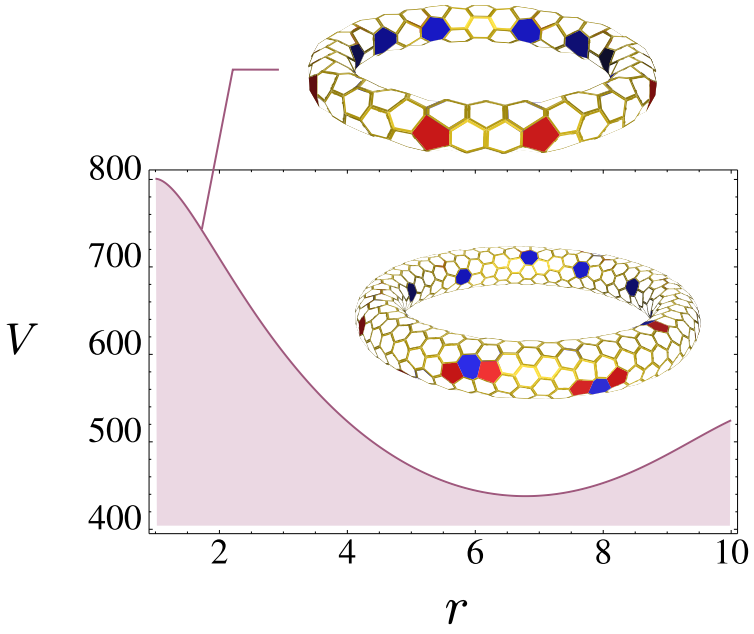

Figure 4.22: (Color online) Isolated defects and scar phases in the (r, V) plane. When the number of vertices V increases the range of the screening curvature becomes smaller than one lattice spacing and disclinations appear delocalized in the form of a $5-7-5$ grain boundary mini-scar.

This hypothesis can be checked by comparing the energy of the TP5 lattice previously described with that of "scarred" configurations obtained by decorating the original toroid in such a way that each $+1$ disclination on the external equator is replaced by a $5-7-5$ mini-scar. The result of this comparison is summarized in the phase diagram of Fig. 4.22 in terms of r and the number of vertices of the triangular lattice V (the corresponding hexagonal lattice has twice the number of vertices, i.e. $V_{hex} = 2V$). V can be derived from the angular separation of neighboring disclinations in the same scar by approximating $V \approx A/A_V$, with $A_V = \frac{\sqrt{3}}{2}a^2$ the area of a hexagonal Voronoi cell and a the lattice spacing. When the aspect ratio is increased from 1 to 6.8 the range of the curvature screening becomes shorter and the number of subunits required to destroy the stability of the TP5 lattice decreases. For $r > 6.8$, however, the geodesic distance between the two equators of the torus becomes too small and the repulsion between like-sign defects takes over. Thus the

trend is inverted.

4.5.3 Numerical simulation of toroidal crystals

In this section we report the result of a numerical minimization of a system of V point-like particles constrained to lie on the surface of a torus and interacting via a pair potential of the form $U_{ij} = 1/|\boldsymbol{x}_i - \boldsymbol{x}_j|^3$ where $|\cdot|$ denotes the Euclidean distance in $\mathbb{R}^3$. The problem of finding the minimal energy configuration of repulsively interacting points on a 2-manifold has become a standard problem of potential theory and has its paradigm in the classical Thomson problem on the sphere. The choice of the cubic potential is motivated here by the so called "poppy seed bagel theorem" [80], according to which the configuration of points that minimizes the Riesz energy $E = \sum_{i<j} 1/|\boldsymbol{x}_i - \boldsymbol{x}_j|^s$ on a rectifiable manifold of Hausdorff dimension d is uniformly distributed on the manifold for $s \geq d$. In the case of a torus of revolution this implies that for small s the points are mostly distributed on the exterior of the torus (the interior becomes completely empty in the limit $V \to \infty$). As s is increased, however, the points cover a progressively larger portion of the surface. The distribution becomes uniform for $s \geq 2$. On the other hand, since the number of local minima of the Riesz energy increases with s, it is practical to choose a value not much larger than two. The choice $s = 3$ has the further advantage of modelling a real physical system of neutral colloidal particles assembled at an interface [35] and is therefore suitable for direct comparison with experiments on colloidal suspensions.

To construct low energy configurations we adopt an carefully designed hybrid optimization algorithm named Tapping (TA). Like other hybrid algorithms, TA consists in a combination of fast local optimizations and global stochastic moves designed to release the system from the local minimum to which it is confined at the end of a local minimization step. A more detailed description of our algorithm is reported in Appendix 4.A We study four different aspect ratios: $r = 3\,, 4\,, 6$ and 20. For each aspect ratio we consider several different particle numbers up to $V = 1000$ and each

simulation is performed for 10^5 to 10^6 TA iterations.

The lowest energies configurations found are shown in Fig. 4.23. Additional informations, including energies and defect structures of the lattices shown here, are available as electronic-only material. The complete set of data produced in our simulations together with a collection of interactive 3D graphics for each low energy configuration studied can be found on-line [165].

The lattices are best presented using a Voronoi construction corresponding to the dual lattice of the Delaunay triangulation. Here pentagonal faces are colored in red while heptagonal faces are colored in blue. For fewer than $V \sim 180$ particles the results of our numerical minimization are in good agreement with the continuum elastic theory. In particular for $180 < V < 500$ and $r = 3$, 4 and 6, we always find minimal energy configurations consisting of ten $5-$fold disclinations on the outside of the torus and ten $7-$fold disclinations in the inside as predicted by the elastic theory in the regime of $\epsilon_c/(AY) \sim 0$. For $r = 20$ and $V > 110$ we also find the lowest energy configurations to be defect free.

For small numbers of particles we don't expect the continuum approximation to accurately describe the lowest energy structure of the toroidal clusters presented in Fig. 4.23. Loosely speaking the limit of validity of the elastic theory can be quantified by requiring the average lattice spacing $a = 2\pi[R_1 R_2/(\frac{\sqrt{3}}{2}V)]^{1/2}$ to be much smaller than the radius R_2 of the torus. This condition requires V to be of order 500 particles for a torus with aspect ratio $r = 3$. Remarkably, good agreement between the theory and simulations is found starting from much smaller values of V and in some cases (see the following discussion on the configuration with $r = 3$ and $V = 130$), we already observe the onset of the ideal behavior predicted by theory for $a \sim R_2$. The occurrence of a ground state configuration with exact prismatic or antiprismatic symmetry, in particular, is only possible when the number of particles V belongs to a specific sequence of "magic numbers" described in §4.4. Nevertheless for V outside such a sequence it is still possible to observe in the ground state a predominant

prismatic or antiprismatic character depending on the aspect ratio.

V	$r_{\min} \pm 0.05$	$r_{\max} \pm 0.05$
16	1.0	1.6
20	1.4	2.6
24	1.8	3.4
28	2.4	4.0
32	2.9	4.6

Table 4.1: Maximum and minimum aspect ratio for which the toroidal antiprisms are a global minimum.

Some configurations deserve special attention. For $V = 16$, 20, 24, 28 and 32 and r within a specific range (see Table 4.1) the global minima are represented by the second to sixth toroidal antiprims discussed in §4.5.1. The drilled icosahedron, on the other hand, would require the aspect ratio be less than one, as can be understood from Table 4.1, and is therefore never a minimum for $V = 12$. We next describe the salient features of the four aspect ratios simulated.

$r = 3$

The smallest minimal energy state with D_{5h} symmetry is obtained for $V = 35$. It features ten disclination pairs and belongs to the class of TP5a graphs. For $V = 42$, a TP6b lattice is obtained with no defects along the two equators. Two 6−fold chiral configurations are obtained for $V = 60$ and 126. The global minimum obtained for $V = 130$ displays a fascinating example of 5−fold antiprismatic symmetry with the ten isolated negative disclinations in the interior of the torus replaced by a simplicial complex consisting of five triangles with a common 5−fold apex and four 7−fold coordinated vertices along the base. A peculiar example is also represented by the minimum obtained for $V = 180$. The lattice exhibits the typical pattern of a TPn graph with $(3, 1, 4, 7)$−type unit cell. The angular distance between neighboring

disclinations is $\delta\phi \sim 2\pi/9$. Since a prismatic graph cannot have an odd number of disclination pairs the toroidal lattice is closed by a simplicial complex consisting of two positive disclinations on the exterior of the torus at the opposite sides of the external equator and two negative disclinations in the interior arranged similarly. The total number of disclination pairs is therefore ten. The typical pattern of the $5-$fold antiprismatic toroid can be found in all configurations with $V > 200$. A single $5-7-5$ scar appears in the $r = 3$ configurations at $V = 420$, while larger lattices (i.e $V = 460$ and 500) also feature $4-$fold disclinations in the interior of the torus. It is not clear, however, whether the presence of disclinations with topological charge $|q| > 1$ is a genuine property of the ground state or rather an artifact due to a misconvergence of our algorithm.

$r = 4$

An interesting feature is observed at $V = 42$. As in the case of $r = 3$ we also find a minimum with D_{6h} symmetry group, but unlike the latter configuration, it belongs to the TP6a class and has $5-$fold disclinations along the external equator. A TP7b configuration is obtained again for $V = 49$. For $V = 66$ and $V = 104$ the global minimum is achieved by two spectacular antiprismatic configurations with D_{11d} and D_{13d} symmetry group respectively. These toroids can be obtained from the toroidal antiprisms discussed in §4.5.1 by splitting [4] one or more times the initial set of $5-$fold vertices. Thus starting from a $11-$fold toroidal antiprism with $V = 4 \times 11 = 44$ vertices and splitting all 22 $5-$fold vertices one obtains $V = 44 + 22 = 66$ vertices. Splitting twice all 26 $5-$fold vertices of a $13-$fold toroidal antiprism with $V = 4 \times 13 = 52$, on the other hand, we have $V = 52 + 2 \times 26 = 104$. For $V = 120$ the global minimum is represented by a fascinating lattice of TP5a type. Lattices

[4] *Vertex splitting* is a standard operation to generate larger triangulations from an irreducible one. It consists in dividing an existing vertex v in two such that the total number of vertices is increased by one. The two newly created vertices have coordination number $c - 1$, with c is the coordination number v, while two of the c neighbors of v gain a bond.

with $V = 121\,, 125$ and 126 resemble very closely the structure of a TP5 graph while for $V = 260$ the lattice has a more antiprismatic character with ten defect pairs.

$r = 6$

Three defect-free configurations are found at $V = 87$, 112 and 116. The case $V = 87$ is a particular example of a defect-free lattice that cannot be obtained form the planar construction reviewed in §4.5.1. It consists of 29 octahedra connected in the form of a chain. Since each octahedron is attached to other two, it contributes with six faces to the total face count. Thus $F = 6 \times 29 = 174$ and $V = 174/2 = 87$. For $180 \leq V < 460$ we always find configurations with ten disclination pairs as expected from continuum elasticity. For $V > 460$ the regime of coexistence between isolated disclinations and scars described in §4.5.2 is observed. The delocalization of isolated disclinations into scars, however, doesn't take place at each defective site simultaneously and the regime of coexistence between positively charged scars and isolated 7−fold disclinations is preceded by a phase with isolated 5− and 7−fold disclinations and scars. For tori with aspect ratio as large as $r = 20$ we find defect-free ground states every time it is possible to construct a purely 6−valent toroidal graph with the same number of vertices V.

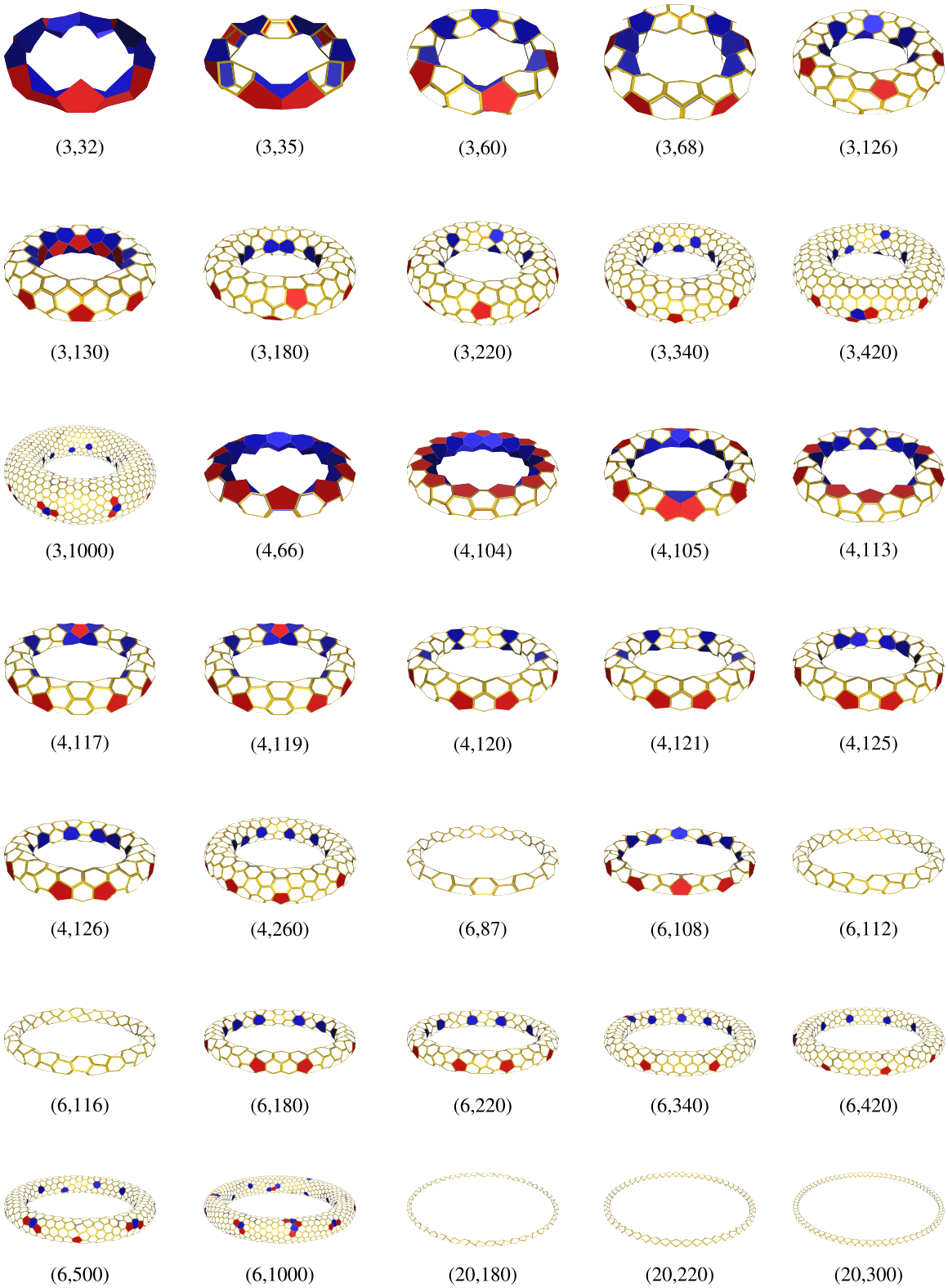

Figure 4.23: (Color online) Selected low energy configurations for toroidal lattices of aspect ratio $r = 3$, 4, 6 and 20. Lattices are labeled by (r, V), with V the number of particles.

Table 4.2: Low energy configuration for a selected number of toroidal lattices with aspect ratios $r = 3$, 4, 6 and 20. For each aspect ratio the table displays the number of particles V, the lowest energy found and the number of $k-$fold vertices V_k with $k = 4$–8.

r	V	V_4	V_5	V_6	V_7	V_8	Energy
3	32	0	16	0	16	0	505.086593
	35	0	10	15	10	0	637.633663
	42	0	12	18	12	0	1020.466912
	120	0	14	92	14	0	14671.476332
	121	0	20	81	20	0	14981.224344
	125	0	19	87	19	0	16255.583992
	126	0	12	102	12	0	16586.793347
	130	0	20	90	20	0	17930.955152
	180	0	10	160	10	0	40623.325218
	220	0	10	200	10	0	67176.585493
	260	2	16	222	20	0	102100.926892
	300	1	10	277	12	0	146139.605664
	340	0	10	320	10	0	199812.441922
	420	0	11	398	11	0	339147.966681
	460	2	14	426	18	0	425754.968401
	500	2	16	462	20	0	524508.172150
	1000	1	17	963	19	0	2965940.674307
4	66	0	22	22	22	0	4905.964854
	104	0	26	52	26	0	15598.534409
	105	0	15	75	15	0	15984.990289
	113	0	19	75	19	0	19237.981548
	117	0	22	73	22	0	21007.172188
	119	0	12	95	12	0	21914.283713
	120	0	10	100	10	0	22371.402771
	121	0	12	97	12	0	22859.735385
	125	0	10	105	10	0	24816.591295
	126	0	10	106	10	0	25311.298095
	180	0	10	160	10	0	62142.129092
	220	0	10	200	10	0	102919.127703
	260	0	10	240	10	0	156499.285669
	300	0	10	280	10	0	223997.341297
	340	0	10	320	10	0	306568.539431
	420	0	13	394	13	0	520431.653442
	460	0	11	438	11	0	653485.181907
	500	0	14	472	14	0	805206.972227

Continue to the next page ...

r	V	V_4	V_5	V_6	V_7	V_8	Energy
	87	0	0	87	0	0	17765.124942
	108	0	12	84	12	0	30894.374674
	112	0	0	112	0	0	33902.717714
	115	0	0	115	0	0	36254.709031
	116	0	0	116	0	0	37074.949162
6	180	0	10	160	10	0	112810.451302
	220	0	10	200	10	0	187146.462245
	260	0	10	240	10	0	284907.016076
	340	0	10	320	10	0	559161.546358
	420	0	10	400	10	0	950488.931696
	500	0	13	474	13	0	1471923.063515
	1000	0	30	940	30	0	8351619.696538
	160	0	0	160	0	0	463967.242489
	170	0	0	160	0	0	543799.839326
	180	0	0	180	0	0	631751.371902
20	220	0	0	220	0	0	1065625.748639
	260	0	0	260	0	0	1636942.532923
	300	0	0	300	0	0	2370110.403872

4.5.4 The Fat Torus Limit

We have seen that disclination defects, forbidden in the lowest energy state of a planar crystal, may be energetically favored on a substrate of non-vanishing Gaussian curvature. It is therefore natural to ask whether large curvature can completely destroy crystalline order by driving the proliferation of a sufficiently high density of defects. The resulting state would be amorphous. The problem of generating amorphous structures by tiling a two-dimensional curved space with identical rigid subunits has drawn attention over the years, particularly through the connection to the structure of such disordered materials as supercooled liquids and metallic glasses. Since the work of Frank [166] the notion of geometrical frustration arises frequently in investigations of supercooled liquids and the glass transition. A paradigmatic example is represented by the icosahedral order in metallic liquids and glasses which, although locally favored, cannot propagate throughout all of three-dimensional Euclidean space. A two-dimensional analog, consisting of a liquid of monodisperse hard

disks in a 2-manifold of constant negative Gaussian curvature (the hyperbolic plane) was first proposed by Nelson and coworkers in 1983 [16]. In such a system the impossibility of covering the entire manifold with a 6-fold coordinated array of disks mimics many aspects of the geometrical frustration of icosahedral order in three dimensions. In all these models of geometrical frustration, however, the origin of the disorder is primarily due to the short-range nature of the potential between the subunits. In a more realistic setting, part of the frustration is relieved by the fact that hexagonal unit cells can compress in order to match the underlying geometry.

The embedding of a triangular lattice on an axisymmetric torus, provides a particularly suitable playground to study curvature-driven disorder. When $r \to 1$ the Gaussian curvature on the inside of the torus grows like $1/(r-1)$ and diverges on the internal equator at $\psi = \pi$. We thus expect a high density of defects in the vicinity of the curvature singularity and a resultant loss of the local $6-$fold bond orientational order. In this regime the system will have crystalline regions on the outside of the torus and amorphous regions near the curvature singularity.

In this section we substantiate this claim analytically based on the elastic theory of continuous distributions of edge dislocations on a "fat" torus. Our argument is based on the following construction. As a consequence of the curvature singularity the surface area of an arbitrary wedge of angular width $\Delta\phi$ becomes smaller and smaller as the sectional angle ψ increases and vanishes at $\psi = \pi$. If a defect-free lattice is embedded on such a wedge, Bragg rows will become closer and closer as the singularity is approached with a consequent rise in the elastic energy (see Fig. 4.24). An intuitive way to reduce the distortion of the lattice is to recursively remove Bragg rows as one approaches the point $\psi = \pi$ (see Fig. 4.25). This is equivalent to introducing a growing density of edge dislocations. This dislocation "cloud" will ultimately disorder the system by destroying the local $6-$fold bond orientational order. One might therefore view the curvature as playing the role of a local effective temperature which can drive "melting" by liberating disclinations and dislocations.

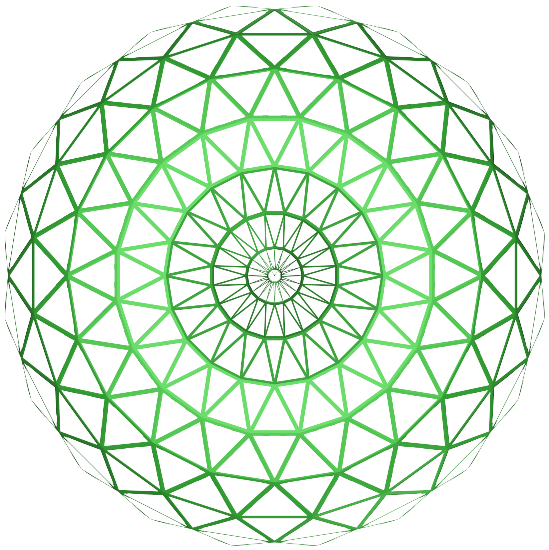

Figure 4.24: (Color online) Top view of a defect free triangulation of a fat torus with $(n, m, l) = (10, 10, 20)$ and $V = 400$. The corresponding elastic energy becomes very high in the interior of the torus where the triangles are more compressed to match the reduction of surface area.

In two-dimensional non-Euclidean crystals at $T = 0$, however, the mechanism for dislocation proliferation is fundamentally different from the usual thermal melting. While the latter is governed by an entropy gain due to unbinding of dislocation pairs, the amorphization at $T = 0$ is due to the adjustment of the lattice to the geometry of the embedding manifold via the proliferation of defects and the consequent release of elastic stress. A similar phenomenon occurs in the disorder-driven amorphization of vortex lattices in type-II and high-T_c superconductors [167].

Since the shrinking area per plaquette on the inside of the torus necessitates a high density of dislocations we may approximate the dislocation cloud in this region by a continuous distribution of Burgers vector density $\boldsymbol{b}$. Minimizing the elastic energy with respect to $\boldsymbol{b}$ yields a variational equation from which the optimal dislocation density can be calculated as a function of the ratio $\epsilon_d/(YR^2)$ between the dislocation core energy ϵ_d and elastic energy scale YR^2 with $R = R_1 = R_2$.

As a starting point, we calculate the Green function $G_L(\boldsymbol{x}, \boldsymbol{y})$ in the fat torus limit

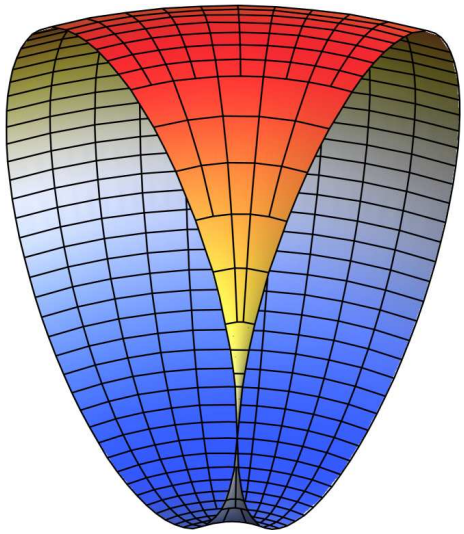

Figure 4.25: (Color online) A schematic example of a dislocation pile-up on a square lattice resulting from the shrinking of the area on a regular wedge of a fat torus.

$r \to 1$ (i.e. $\kappa \to \infty$ and $\omega \to 0$, see Eq. (4.10)). The conformal angle ξ in this limit is:

$$\lim_{r\to 1} \xi = \tan\frac{\psi}{2}\,,$$

and to leading order of κ we have:

$$\frac{\kappa}{16\pi^2}\left(\psi - \frac{2}{\kappa}\xi\right)^2 \to \frac{\kappa}{16\pi^2}\,\psi^2 - \frac{\psi}{4\pi}\tan\frac{\psi}{2}\,,$$

$$\frac{\kappa}{4\pi^2}\,\mathrm{Re}\{\mathrm{Li}_2(\alpha e^{i\psi})\} \to \frac{\kappa}{16\pi^2}\,\psi^2 + \frac{1}{2\pi^2}\log\left(\cos\frac{\psi}{2}\right)\,.$$

To handle the limit of the Jacobi theta function we can take $u = \Delta z/\kappa$, $q = e^{i\pi\tau} = e^{-\frac{2\pi}{\kappa}}$ and calculate the limit $q \to 1$. This can be done by using the modular transformation properties of Jacobi functions [134, 135]:

$$\vartheta_1\left(\tfrac{u}{\tau}|-\tfrac{1}{\tau}\right) = -i(-i\tau)^{\frac{1}{2}} e^{\frac{iu^2}{\pi\tau}}\vartheta_1(u|\tau)\,. \tag{4.59}$$

Thus $\tau' = -1/\tau = i\kappa/2$, $u' = u/\tau = \Delta z/(2i)$ and $q' = e^{i\tau'} = e^{-\frac{\pi\kappa}{2}}$, where:

$$\lim_{q\to 1}\vartheta_1(u,q) = \lim_{q'\to 0} i\left(\frac{i}{\tau'}\right)^{-\frac{1}{2}} e^{\frac{iu'^2}{\pi\tau'}}\vartheta_1(u',q')\,.$$

This is easily evaluated by means of the expansion:

$$\vartheta_1(u,q) = 2q^{\frac{1}{4}} \sin u + o\left(q^{\frac{9}{4}}\right) .$$

Taking the logarithm and neglecting irrelevant constant terms, we obtain:

$$\log \left| \vartheta_1 \left(\frac{z-z'}{\kappa} \middle| \frac{2i}{\kappa} \right) \right| \sim \log \left| \sinh \left(\frac{z-z'}{2} \right) \right| ,$$

which finally leads to:

$$G_L(\psi,\phi,\psi',\phi') \sim -\frac{\psi'}{4\pi^2} \tan\frac{\psi'}{2} + \frac{1}{2\pi} \log \left| \sinh \left(\frac{z-z'}{2} \right) \right| \tag{4.60}$$

with $z = \tan(\psi/2) + i\phi$. With the Green function in hand, we can calculate the effect of the curvature singularity at $\psi = \pi$ on the distribution of defects. Let $\boldsymbol{b}$ be the Burgers vector density of the dislocation cloud. Hereafter we work in a local frame, so that:

$$\boldsymbol{b} = b^{\psi} \boldsymbol{g}_{\psi} + b^{\phi} \boldsymbol{g}_{\phi} , \tag{4.61}$$

with $\boldsymbol{g}_i = \partial_i \boldsymbol{R}$ a basis vector in the tangent plane of the torus. $\boldsymbol{R}$ is a three-dimensional surface vector parameterizing the torus and its Cartesian components are given in Eq. (4.1). The quantity $\boldsymbol{b}$ has to be such that:

$$\int_D d^2x \, \boldsymbol{b}(x) = \boldsymbol{b}_D ,$$

with $\boldsymbol{b}_D$ the total Burger's vector in a generic domain D. Because on a closed manifold dislocation lines cannot terminate on the boundary, extending the integration to the whole torus we have:

$$\int d^2x \, \boldsymbol{b}(\boldsymbol{x}) = 0 . \tag{4.62}$$

Since the basis vectors $\boldsymbol{g}_i$ in Eq. (4.61) have the dimension of length, contravariant coordinates b^i have dimensions of an inverse area. Assuming all defects to be paired in the form of dislocations (i.e. $q_i = 0$ everywhere), the total energy of the crystal reads:

$$F = \frac{1}{2Y} \int d^2x \, \Gamma^2(\boldsymbol{x}) + \epsilon_d \int d^2x \, |\boldsymbol{b}(\boldsymbol{x})|^2 , \tag{4.63}$$

where ϵ_d is the dislocation core energy and

$$|\boldsymbol{b}|^2 = g_{ij} b^i b^j = g_{\psi\psi}(b^\psi)^2 + g_{\phi\phi}(b^\phi)^2 \,.$$

The function $\Gamma(\boldsymbol{x})$ encoding the elastic stress due to the curvature and the screening contribution of the dislocation cloud obeys

$$\frac{1}{Y}\Delta_g \Gamma(\boldsymbol{x}) = \epsilon^i_k \nabla_i b^k(\boldsymbol{x}) - K(\boldsymbol{x}) \,, \tag{4.64}$$

where ∇_i is the usual covariant derivative along the coordinate-direction i and ϵ^i_k is the Levi-Civita antisymmetric tensor on the torus:

$$\epsilon_{\psi\phi} = -\epsilon_{\phi\psi} = \sqrt{g} \,, \qquad\qquad \epsilon^j_i = g_{ik}\epsilon^{jk} \,.$$

The stress function $\Gamma(\boldsymbol{x})$ can be expressed in the form $\Gamma(\boldsymbol{x}) = \Gamma_d(\psi,\phi) - \Gamma_s(\psi)$ with

$$\frac{\Gamma_s(\psi)}{Y} = \log\left[\frac{1}{2(1+\cos\psi)}\right] + 1 \,, \tag{4.65a}$$

$$\frac{\Gamma_s(\psi,\phi)}{Y} = \int d^2y \, \epsilon^i_k \nabla_i b^k(\boldsymbol{y}) \, G_L(\boldsymbol{x},\boldsymbol{y}) \,. \tag{4.65b}$$

Taking advantage of the closeness of the torus we can integrate Eq. (4.65b) by parts so that:

$$\frac{\Gamma_d(\psi,\phi)}{Y} = -\int d^2y \, \epsilon^i_k b^k(\boldsymbol{y}) \partial_i \, G_L(\boldsymbol{x},\boldsymbol{y}) \,. \tag{4.66}$$

Now we want reduce the integral term in Eq. (4.66) to a more friendly functional of $\boldsymbol{b}$, suitable for a variational approach. Given the azimuthal symmetry we assume that all dislocations are aligned along $\boldsymbol{b} = b^\phi \boldsymbol{g}_\phi$. Even though not necessarily true, we argue this to be a reasonable work hypothesis as well as a solid starting point to capture the essential physics of the fat limit. In this case $\Gamma_d(\psi,\phi) = \Gamma_d(\psi)$ can be recast in the form

$$\frac{\Gamma_d(\psi)}{Y} = \frac{1}{2\pi}\int_{-\pi}^{\pi} d\psi' \sqrt{g}\, b^\phi(\psi') \left[\psi' + \sin\psi' + \pi\,\mathrm{sgn}(\psi-\psi')\right] \,. \tag{4.67}$$

Substituting Eq. (4.67) and (4.65a) in Eq. (4.63) and minimizing with respect to b^ϕ we can now write the variational equation:

$$4\epsilon_d R^2(1+\cos\psi)^2 b^\phi(\psi) + \int_{-\pi}^{\pi} d\psi\, \sqrt{g}\, \Gamma_d(\psi')\, \mathrm{sgn}(\psi-\psi') = \int_{-\pi}^{\pi} d\psi\, \sqrt{g}\, \Gamma_s(\psi')\, \mathrm{sgn}(\psi-\psi')\,. \tag{4.68}$$

By inverting the order of integration in the integral on the right hand side, Eq (4.68) can be expressed in the form of a Fredholm equation of the second kind:

$$\lambda B(\psi) - \int_{-\pi}^{\pi} d\psi'\, B(\psi')\mathcal{K}(\psi,\psi') = f(\psi)\,, \tag{4.69}$$

where $\lambda = \epsilon_d/(YR^2)$, $B(\psi) = R^2(1+\cos\psi)^2 b^\phi(\psi)$ and the kernel $\mathcal{K}(\psi,\psi')$ is given by:

$$\mathcal{K}(\psi,\psi') = \frac{1}{4(1+\cos\psi')}\Bigg\{\pi^{-1}(\psi'+\sin\psi')(\psi+\sin\psi) + |\psi-\psi'| + 2\cos\frac{\psi+\psi'}{2}\sin\frac{|\psi-\psi'|}{2}\Bigg\}. \tag{4.70}$$

The function $f(\psi)$ on the right hand side of Eq. (4.69) is given by:

$$f(\psi) = -\frac{1}{4}\int_{-\psi}^{\psi} d\psi'\,(1+\cos\psi')\,\Gamma_s(\psi') = \frac{1}{2}\big\{[\log 2(1+\cos\psi)-2]\sin\psi - 2\,\mathrm{Cl}_2(\psi+\pi)\big\} \tag{4.71}$$

where Cl_2 is the Clausen function (see Ref. [168], pp. 1005-1006) defined as:

$$\mathrm{Cl}_2(x) = -\int_0^x dx\, \log\left(2\sin\frac{t}{2}\right) = \sum_{k=1}^{\infty}\frac{\sin kx}{k^2}\,.$$

As previously noted the dislocation core energy is ϵ_d is much smaller than the elastic energy scale YR^2. Eq (4.69) is then suitable to be solved in powers of the dimensionless number λ:

$$B(\psi) = B_0(\psi) + \lambda B_1(\psi) + \lambda^2 B_2(\psi) + \cdots$$

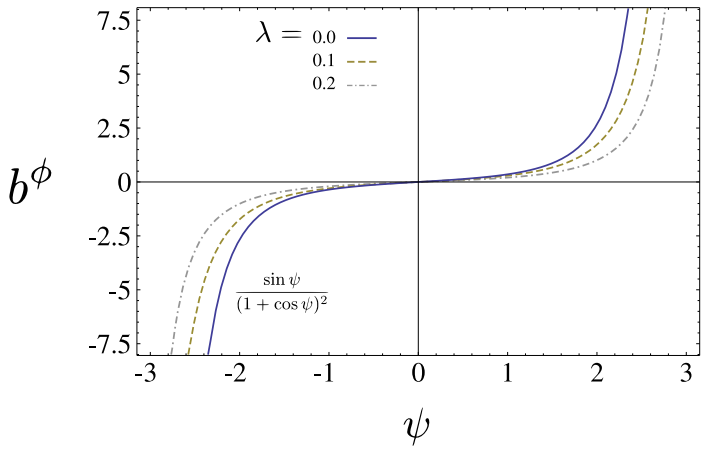

Figure 4.26: (Color online) The Burgers vector component $b(\psi)$ for different choices of λ.

The corrections to the zero-order term $B_0(\psi)$ can be calculated recursively by solving a set of Fredholm equations of the first kind:

$$B_{k-1}(\psi) = \int_{-\pi}^{\pi} d\psi'\, B_k(\psi)\mathcal{K}(\psi,\psi') \qquad k \geq 1\,.$$

The function $B_0(\psi)$ associated with the Burgers vector density of the dislocation cloud in the limit $\lambda \to 0$, on the other hand, can be calculated directly from Eq. (4.64) by setting the effective topological charge density on the right hand side to zero:

$$\epsilon^i_k \nabla_i b^k(\boldsymbol{x}) - K(\boldsymbol{x}) = 0\,. \tag{4.72}$$

For a torus of revolution the only nonzero Christoffel symbols are

$$\Gamma^\phi_{\phi\psi} = \Gamma^\phi_{\psi\phi} = -\frac{R_2 \sin\psi}{R_1 + R_2\cos\psi}\,,$$

$$\Gamma^\psi_{\phi\phi} = R_2^{-1}\sin\psi(R_1 + R_2\cos\psi)\,.$$

Since $b^\psi = 0$ by assumption, the first term in Eq. (4.72) can be expressed as:

$$\begin{aligned}\epsilon^i_k \nabla_i b^k &= \epsilon^\psi_\phi(\partial_\psi b^\phi + \Gamma^\phi_{\psi\phi} b^\phi) + \epsilon^\phi_\psi \Gamma^\psi_{\phi\phi} b^\phi \\ &= (1+\cos\psi)\partial_\psi b^\phi - 2\sin\psi\, b^\phi\,,\end{aligned}$$

and Eq. (4.72) becomes an ordinary differential equation

$$\partial_\psi b^\phi - \frac{2\sin\psi}{1+\cos\psi}\, b^\phi = \frac{\cos\psi}{R^2(1+\cos\psi)^2}\,, \tag{4.73}$$

whose solution is given by

$$b^\phi = \frac{\sin\psi}{R^2(1+\cos\psi)^2}\,, \tag{4.74}$$

so that $B_0(\psi) = \sin\psi$. The Burgers vector density b^ϕ obtained by a numerical solution of Eq. (4.69) is shown in Fig. 4.26 for different values of λ. The Burgers vector density is measured in units of R^{-2}. The function b^ϕ has cubic singularities at $\psi = \pm\pi$ and is approximately zero on the outside of the torus. The solid blue curve in Fig. 4.26 represents the zeroth order solution of Eq.(4.74).

Now, in the theory of dislocation mediated melting a system at the solid liquid phase boundary is described as a crystalline solid saturated with dislocations. In three-dimensions, in particular, there is a strong experimental evidence of the existence of a critical dislocation density at the melting point $\rho(T_m) \approx 0.6 b^{-2}$ where b is the length of the length of the smallest perfect-dislocation Burgers vector [169]. Several theoretical works have motivated this evidence both for three-dimensional solids and vortex lattices in super conductors [167]. On the other hand, given the existence of such a critical density, its value can be empirically used to determine whether a system is in a solid or liquid-like phase in the same spirit as the Lindemann criterion. With this goal in mind we can calculate the dislocation density by requiring $|\boldsymbol{b}| = \rho a$ with ρ the density of single lattice spacing dislocations. This yields:

$$\rho(\psi, V) a^2 = 2\pi \left(\frac{\sqrt{3}}{2}\, V\right)^{-\frac{1}{2}} \left|\tan\frac{\psi}{2}\right| + o(\lambda) \tag{4.75}$$

Solving $\rho(\psi, V)a^2 = 0.6$ as a function of ψ and V we obtain the diagram of Fig. 4.27. As expected the inside of the torus contains an amorphous region whose angular size decreases with the number of vertices V as a consequence of the reduction of the lattice spacing.

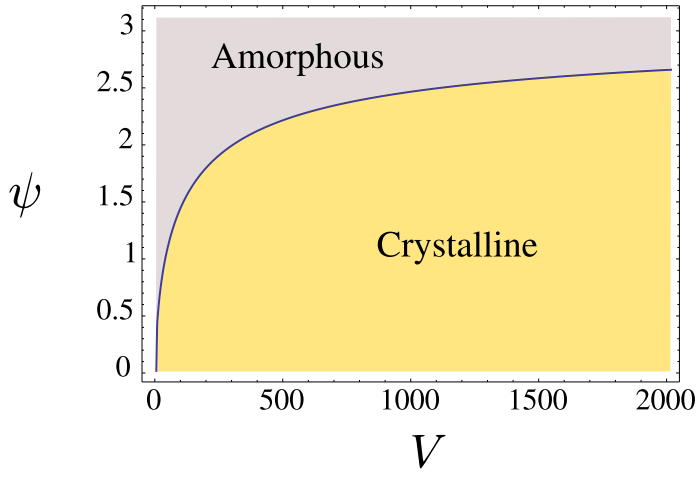

Figure 4.27: (Color online) Phase diagram for curvature driven amorphization. The inside of the torus contains an amorphous region whose angular size decreases with the number of vertices V as a consequence of the reduction of the lattice spacing.

Appendix 4.A Cluster optimization via Tapping

The Tapping Algorithm (TA) is a hybrid algorithm designed to find the optimal crystalline structure of particle systems constrained to lie on a curved surface and interacting with a long range potential of the form $U_{ij} = 1/|\boldsymbol{r}_i - \boldsymbol{r}_j|^s$. Hybrid algorithms, such as Basin-Hopping [170] and Minima-Hopping [171], have been successfully employed throughout the years to predict the crystalline structure of molecular clusters and proteins. In general they combine fast local minimizations with global moves whose goal is to release the system from the local minimum it is confined at the end of a local minimization step.

A typical hybrid optimization routine can be summarized in the following two steps: *1*) after all the independent variables have been randomly initialized, a local optimization is performed and a local minimum x is determined; *2*) from x a new configuration y is constructed by applying a global (generally stochastic) move. The new configuration y is then used as starting point for a new local optimization step. The two steps are iterated until a stopping criterion is satisfied. The goal is thus

to explore the largest possible number of local minima and avoid visiting the same minimum too often.

The crucial point in designing an effective hybrid algorithm is clearly the choice of the global move. There is no general rule to identify a successful global transformation $x \to y$ and physical intuition and prior experience are typically the only guidelines. In the case of Basin-Hopping, for instance, the global transformation consists in a Monte Carlo move in which all the particles of the system are randomly displaced in order to construct a new initial configuration from which a new trial minimum is obtained. The step is accepted with probability $\exp(-\beta\Delta V)$, where ΔV is the energy difference between the new and previous minimum and β is an inverse temperature adjusted to obtain a 50% acceptance ratio. In the case of Minima-Hopping the escape step is performed by a short Molecular Dynamics simulation by assigning the particles a fixed kinetic energy.

The global move adopted in TA is inspired by the process of close packing of spherical objects by tapping and is motivated by the well established role of topological defects in determining the order of two-dimensional non-Euclidean crystals as well as the picture of the potential energy surface (PES) of such systems as a multi-funnel landscape. Consider a system of say spherical objects confined in a two-dimensional box with an initial disordered configuration. A common way to bias the system toward a close-packed configuration is to provide it kinetic energy by gently tapping the box. If the system is populated by locally ordered regions (i.e. grains) separated by clusters of defects, the primary effect of tapping is to produce a glide of defects inside the crystals with a subsequent rearrangement of grains. This mechanism can be reproduced numerically in the following way. The algorithm starts with a random distribution of particles and rapidly quenches the system by performing a fast local minimization. Once particles are trapped in a local minimum, defects are identified by a Delaunay triangulation of the lattice. Then the system is tapped by adding to the defect positions a random displacement. The magnitude of the displacement is

given by the typical spacing associated with the particles number times a factor λ which represents the tapping strength. This factor is initially set to 10^{-3}. After defects have been moved a new local minimization is performed in order to construct the trial configuration y. The energy of this configuration is compared with the energy of the previous minimum and the move is accepted if their difference is larger than some tolerance factor ϵ_E. If, on the other hand, the energy difference is smaller than ϵ_E, the system has relaxed again to the same minimum. In this case the tapping strength is increased of a factor 10 and the process is repeated until the system successfully hops to a new minimum. The tapping strength λ is then set to its initial value. The process is iterated until the rate of discovery of new global minima drops below some threshold value or a maximum number of iterations is reached.

In the current implementation of the algorithm, the local minimization step is performed using the Fletcher-Reeves conjugate gradient algorithm [172]. Analytic expressions for the energy gradient and the Hessian matrix are coded in the program in order to reduce the number of evaluations of the objective function during the relaxation step to one single event. The Delaunay triangulation is calculated via the Dwyer's divide and conquer algorithm with alternate cuts [173], which runs in $O(N \log \log N)$ time, making the identification of the defects particularly fast.

The main difference between TA and other hybrid algorithms (including Basin-Hopping) is that the escape move consists of adaptive displacements of defects only, rather than of the entire system. In the case of non-Euclidean crystals, where the conformation of the energy landscape is subtly related to the arrangement of topological defects, this mechanism is believed to explore the PES more accurately. In systems as Lennard-Jones clusters or spin-glasses, the PES is characterized by an exponential number of local minima separated by energy barriers. For this reason the majority of the algorithms are specifically designed to allow the system to overcome a barrier by providing it a significant amount of energy. If the energy landscape, however, is characterized by the presence of multiple narrow funnels, as believed in this case, the

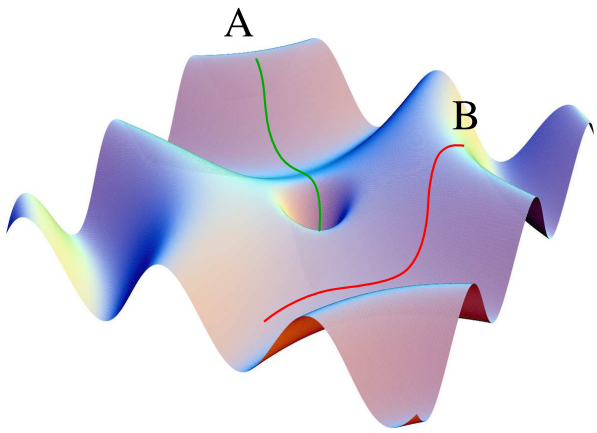

Figure 4.28: Possible pathways is a funneled landscape.

previous methods become ineffective. A funnel represents the basin of attraction of a given local minimum. If the global minimum is also located at the bottom of a funnel, an algorithm that is attempting to locate it via a sequence of local minimization steps has a chance to find it exclusively by starting from a configuration already at the muzzle of the funnel. Such possibility, however, is ruled out if all the particles are displaced simultaneously during the escape move and the system is abruptly moved to a completely different place in the energy landscape. On the other hand, by adaptively tapping the defects it is possible to achieve a much finer inspection of the PES and possibly locate the funnel associated with the global minimum.

Appendix 4.B The doubly periodic Green function

In this Appendix I provide a step-by-step proof of Eq. (4.19). Starting from Eq. (4.18) we can notice that all sinusoidal terms cancel when the summation is carried

out. Eq. (4.18) becomes then:

$$G_0(\boldsymbol{x},\boldsymbol{y}) = -\frac{1}{p_1 p_2}\sum_{(n,m)\neq(0,0)}\frac{\cos\lambda_n(x-\xi)\cos\mu_m(y-\eta)}{\lambda_n^2+\mu_m^2}$$

$$= -\frac{2}{p_1 p_2}\left[\sum_{m=1}^{\infty}\frac{\cos\frac{2\pi m}{p_2}(y-\eta)}{\left(\frac{2\pi m}{p_2}\right)^2} + \sum_{n=1}^{\infty}\sum_{m=-\infty}^{\infty}\frac{\cos\frac{2\pi n}{p_1}(x-\xi)\cos\frac{2\pi m}{p_2}(y-\eta)}{\left(\frac{2\pi n}{p_1}\right)^2+\left(\frac{2\pi m}{p_2}\right)^2}\right]. \quad (4.76)$$

An equivalent expression can be obtained by isolating the $m=0$ contribution in the sum rather then the $n=0$ one. The first sum in Eq. (4.76) can be evaluated easily by using:

$$\sum_{k=1}^{\infty}\frac{\cos kx}{k^2} = \frac{\pi^2}{6} - \frac{\pi|x|}{2} + \frac{x^2}{4} \quad (4.77)$$

Thus we have:

$$H(y-\eta) = -\frac{2}{p_1 p_2}\sum_{m=1}^{\infty}\frac{\cos\frac{2\pi m}{p_2}(y-\eta)}{(\frac{2\pi m}{p_2})^2} = -\frac{1}{2\,p_1 p_2}\left(\frac{p_2^2}{6} - p_2|y-\eta| + |y-\eta|^2\right) \quad (4.78)$$

The second sum in Eq. (4.76) can be evaluated with the help of the Poisson summation formula in the form:

$$\sum_{m=-\infty}^{\infty} f(m)\cos pm = \sum_{k=-\infty}^{\infty}\int_{-\infty}^{\infty} dt\, f(t)\cos(2k\pi+p)\,t \quad (4.79)$$

In particular if we choose:

$$f(m) = \frac{1}{\left(\frac{2\pi n}{p_1}\right)^2+\left(\frac{2\pi m}{p_2}\right)^2} \qquad p = \frac{2\pi}{p_2}(y-\eta)$$

we can write the second sum in the (4.76) as:

$$K(x-\xi,y-\eta) = -\frac{2}{p_1 p_2}\sum_{n=1}^{\infty}\cos\frac{2\pi n}{p_1}(x-\xi)\sum_{m=-\infty}^{\infty}\frac{\cos\frac{2\pi m}{p_2}(y-\eta)}{\left(\frac{2\pi n}{p_1}\right)^2+\left(\frac{2\pi m}{p_2}\right)^2}$$

$$= -\frac{2}{p_1 p_2}\sum_{n=1}^{\infty}\cos\frac{2\pi n}{p_1}(x-\xi)\sum_{k=-\infty}^{\infty}\int_{-\infty}^{\infty} dt\,\frac{\cos(2\pi k+p)\,t}{\left(\frac{2\pi n}{p_1}\right)^2+\left(\frac{2\pi t}{p_2}\right)^2} \quad (4.80)$$

The integral can be easily done by remembering:

$$\int_0^\infty dx\,\frac{\cos\omega x}{a^2+x^2}=\frac{\pi}{2a}\,e^{-\omega a}$$

and then:

$$\int_{-\infty}^{\infty}dt\,\frac{\cos(2\pi k+p)\,t}{\left(\frac{2\pi n}{p_1}\right)^2+\left(\frac{2\pi t}{p_2}\right)^2}=\frac{p_1p_2}{4\pi n}\exp\left[-\left(\frac{2\pi n}{p_1}\right)|p_2k+y-\eta|\right]$$

Therefore, Eq. (4.80) becomes:

$$K(x-\xi,y-\eta)=-\frac{1}{2\pi}\sum_{k=-\infty}^{\infty}\sum_{n=1}^{\infty}\frac{e^{-\frac{2\pi n}{p_1}|p_2k+y-\eta|}}{n}\,\cos\frac{2\pi n}{p_1}(x-\xi) \tag{4.81}$$

The sum in n can be calculated by taking into account:

$$\sum_{n=1}^{\infty}\frac{e^{-2\pi nx}}{n}\,\cos(2\pi ny)=-\log|1-e^{-z}| \tag{4.82}$$

where z is the complex number:

$$z=2\pi(x\pm iy)$$

with $x>0$ and an arbitrary choice of the sign. To use Eq. (4.82) is convenient to separate positive and negative k in Eq. (4.81):

$$\begin{aligned}-2\pi K(x-\xi,y-\eta)=&\sum_{n=1}^{\infty}\frac{e^{-\frac{2\pi n}{p_1}|y-\eta|}}{n}\,\cos\frac{2\pi n}{p_1}(x-\xi)\\&+\sum_{k=1}^{\infty}\sum_{n=1}^{\infty}\frac{e^{-\frac{2\pi n}{p_1}|p_2k+y-\eta|}}{n}\,\cos\frac{2\pi n}{p_1}(x-\xi)\\&+\sum_{k=1}^{\infty}\sum_{n=1}^{\infty}\frac{e^{-\frac{2\pi n}{p_1}|-p_2k+y-\eta|}}{n}\,\cos\frac{2\pi n}{p_1}(x-\xi)\end{aligned} \tag{4.83}$$

Now, because $y,\eta\in[0,p_2]$ we have $y-\eta\in[-p_2,p_2]$ which allow us the write the modulus in the following way:

$$\left.\begin{aligned}|p_2k+(y-\eta)| &= p_2k+(y-\eta)\\ |-p_2k+(y-\eta)| &= p_2k-(y-\eta)\end{aligned}\right\}\quad\forall k\geq 1$$

Introducing the complex variable:

$$\sigma_k^{\pm} = 2\pi(a_k^{\pm} \mp i b_k)$$

with:

$$a_k^{\pm} = \frac{p_2 k \pm (y-\eta)}{p_1} \qquad\qquad b_k = \frac{x-\xi}{p_1}$$

and using Eq. (4.82), we can rewrite Eq. (4.83) as:

$$2\pi K(x-\xi, y-\eta) = \log\left|1 - e^{-\sigma_0}\right| + \sum_{k=1}^{\infty} \log\left|1 - e^{-\sigma_k^+} - e^{-\sigma_k^-} + e^{-(\sigma_k^+ + \sigma_k^-)}\right|$$

$$= \log\left|1 - e^{\frac{2\pi i}{p_1}(z-\zeta)}\right| + \sum_{k=1}^{\infty} \log\left|1 - 2q^{2k}\cos\frac{2\pi}{p_1}(z-\zeta) + q^{4k}\right| \tag{4.84}$$

having called:

$$\begin{cases} z = x + iy \\ \zeta = \xi + i\eta \end{cases} \qquad \text{and} \qquad q = e^{-\frac{\pi p_2}{p_1}}$$

The second term in Eq. (4.83) can be expressed in terms of the Jacobi theta function $\vartheta_1(u,q)$ defined as:

$$\vartheta_1(u,q) = 2q^{\frac{1}{4}} \sin u \prod_{n=1}^{\infty} \left(1 - 2q^{2n}\cos 2u + q^{4n}\right)\left(1 - q^{2n}\right)$$

Another useful relation can be obtain by taking the derivative of $\vartheta_1(u,q)$ with respect to u:

$$\lim_{u\to 0} \frac{\vartheta_1(u,q)}{\sin u} = \lim_{u\to 0} \frac{\vartheta_1'(u,q)}{\cos u} = \vartheta_1'(0,q)$$

So it is easy to evaluate:

$$\vartheta_1'(0,q) = \lim_{u\to 0} \frac{\vartheta(u,q)}{\sin u} = 2q^{\frac{1}{4}} \prod_{k=1}^{\infty} \left(1 - 2q^{2k} + q^{4k}\right)\left(1 - q^{2k}\right) = 2q^{\frac{1}{4}} \prod_{k=1}^{\infty} \left(1 - q^{2k}\right)^3 \tag{4.85}$$

In this way we can express:

$$\prod_{k=1}^{\infty}(1 - 2q^{2k}\cos 2u + q^{4k}) = \frac{1}{(2q^{\frac{1}{4}})^{\frac{2}{3}} \sin u}\left[\frac{\vartheta_1(u,q)}{\vartheta_1'^{\frac{1}{3}}(0,q)}\right]$$

Taking:

$$u = \frac{\pi}{p_1}(z - \zeta)$$

and replacing in Eq. (4.84) we obtain:

$$\begin{aligned} 2\pi K(x-\xi, y-\eta) &= \log|1 - e^{2iu}| + \log\left|\frac{\vartheta_1(u,q)}{\vartheta_1'^{\frac{1}{3}}(0,q)}\right| - \log\left|(2q^{\frac{1}{4}})^{\frac{2}{3}}\sin u\right| \\ &= \frac{\log 2}{3} + \frac{\pi}{6}\frac{p_2}{p_1} - \frac{\pi}{p_1}|y-\eta| + \log\left|\frac{\vartheta_1(u,q)}{\vartheta_1'^{\frac{1}{3}}(0,q)}\right| \end{aligned} \tag{4.86}$$

having used the fact that:

$$\log\left|1 - e^{2iu}\right| = \log|e^{iu}| + \log|2i\sin u|$$

$$\log\left|(2q^{\frac{1}{4}})^{\frac{2}{3}}\sin u\right| = \frac{2}{3}\log 2 - \frac{\pi}{6}\frac{p_2}{p_1} + \log|\sin u|$$

Combining Eq. (4.86) with Eq. (4.78) we finally obtain:

$$\begin{aligned} G_0(\boldsymbol{x}, \boldsymbol{y}) &= H(y-\eta) + K(x-\xi, y-\eta) \\ &= \frac{\log 2}{6\pi} - \frac{1}{2\,p_1 p_2}|y-\eta|^2 + \frac{1}{2\pi}\log\left|\frac{\vartheta_1(u,q)}{\vartheta_1'^{\frac{1}{3}}(0,q)}\right| \end{aligned} \tag{4.87}$$

An alternative notation frequently used for the Jacobi theta function is:

$$\vartheta_1(u|\tau) = \vartheta(u,q) \qquad\qquad q = e^{i\pi\tau}$$

adopting this choice we can write the Green function in the final form:

$$G_0(\boldsymbol{x}, \boldsymbol{y}) = \frac{\log 2}{6\pi} - \frac{1}{2\,p_1 p_2}|y-\eta|^2 + \frac{1}{2\pi}\log\left|\frac{\vartheta_1(\frac{z-\zeta}{p_1/\pi}|\frac{ip_2}{p_1})}{\vartheta_1'^{\frac{1}{3}}(0|\frac{ip_2}{p_1})}\right| \tag{4.88}$$

Appendix 4.C The stress function $\Gamma_s(\boldsymbol{x})$

To calculate the stress function $\Gamma_s(\boldsymbol{x})$, it is convenient to start from:

$$\Gamma_s(\boldsymbol{x}) = \int d^2y\, K(\boldsymbol{y})[G_0(\boldsymbol{x}, \boldsymbol{y}) - \langle G_0(\cdot\,, \boldsymbol{y})\rangle] = \Gamma_{s,1}(\boldsymbol{x}) - \Gamma_{s,2}$$

where we called:

$$\Gamma_{s,1}(\boldsymbol{x}) = \int d^2y\, K(\boldsymbol{y})\, G_0(\boldsymbol{x},\boldsymbol{y}) \qquad \Gamma_{s,2} = \int d^2y\, K(\boldsymbol{y})\, \langle G_0(\cdot\,,\boldsymbol{y})\rangle$$

The calculation of these integrals can be made more straightforward by keeping the Green function in the form (4.76). We have then:

$$\Gamma_{s,1} = -\frac{1}{p_1 p_2} \sum_{(n,m)\neq(0,0)} \frac{1}{\lambda_n^2+\mu_m^2} \int_{-\pi}^{\pi} d\psi'\, \cos\psi' \cos\lambda_n(\xi-\xi') \int_{-\pi}^{\pi} d\phi'\, \cos\mu_m(\phi-\phi')$$

The integral in ϕ' is non-zero only for $m=0$:

$$\int_{-\pi}^{\pi} d\phi'\, \cos\mu_m(\phi-\phi') = \int_{-\pi}^{\pi} d\phi'\, \cos m(\phi-\phi') = 2\pi\delta_{m,0} \qquad m = 0,\, \pm1,\, \pm2\,\ldots$$

Then we have:

$$\Gamma_{s,1}(\boldsymbol{x}) = -\frac{2\pi}{p_1 p_2} \sum_{n\neq0} \lambda_n^{-2} \int_{-\pi}^{\pi} d\psi'\, \cos\psi' \cos\lambda_n(\xi-\xi')$$

$$= -\frac{2}{p_1}\left(\frac{p_1}{2\pi}\right)^2 \int_{-\pi}^{\pi} d\psi'\, \cos\psi' \sum_{n=1}^{\infty} \frac{\cos\frac{2\pi n}{p_1}(\xi-\xi')}{n^2}$$

Using Eq. (4.77) we can rewrite:

$$\Gamma_{s,1}(\boldsymbol{x}) = -\frac{p_1}{12}\int_{-\pi}^{\pi} d\psi'\, \cos\psi' + \frac{1}{2}\int_{-\pi}^{\pi} d\psi'\, \cos\psi'\, |\xi-\xi'| - \frac{1}{2p_1}\int_{-\pi}^{\pi} d\psi'\, \cos\psi'\, |\xi-\xi|^2 \quad (4.89)$$

The first integral is zero. Two calculate the second integral we can take

$$|\xi-\xi'| = \begin{cases} \xi-\xi' & \text{if} \quad \xi'<\xi \quad\rightarrow\quad \psi'<\psi \\ \xi'-\xi & \text{if} \quad \xi'>\xi \quad\rightarrow\quad \psi'>\psi \end{cases}$$

Thus:

$$\Gamma_{s,11} = \int_{-\pi}^{\pi} d\psi'\, \cos\psi'\, |\xi-\xi'| = \xi\int_{-\psi}^{\psi} d\psi'\, \cos\psi' + 2\int_{\psi}^{\pi} d\psi' \cos\psi'\xi'$$

$$= \xi(\psi)\Big[\sin\psi'\Big]_{-\psi}^{\psi} + 2\Big[\xi(\psi')\sin\psi' + \log(r+\cos\psi')\Big]_{\psi}^{\pi}$$

$$= 2\log\left(\frac{r-1}{r+\cos\psi}\right)$$

where the second line has been obtained by a simple integration by parts:

$$\int d\psi\, \cos\psi\, \xi = \xi\, \sin\psi - \int d\psi\, \frac{\sin\psi}{r+\cos\psi} = \xi\, \sin\psi + \log(r+\cos\psi)$$

To calculate the third integral in Eq. (4.89) we can expand the square and use the fact that the function ξ is odd in ψ. Then:

$$\int_{-\pi}^{\pi} d\psi'\, \cos\psi'\, |\xi - \xi'|^2 = \int_{-\pi}^{\pi} d\psi'\, \cos\psi' \xi'^2$$

The integral on the right hand side can be now calculated by parts:

$$\Gamma_{s,12} = \int_{-\pi}^{\pi} d\psi'\, \cos\psi'\, \xi'^2$$

$$= \Big[\sin\psi'\, \xi^2\Big]_{-\pi}^{\pi} - 2\int_{-\pi}^{\pi} d\psi'\, \sin\psi'\, \xi' \frac{d\xi'}{d\psi'}$$

$$= -2\int_{-\frac{1}{2}\pi\kappa}^{\frac{1}{2}\pi\kappa} d\xi'\, \sin\psi'\, \xi'$$

having considered:

$$\xi(\pi) = -\xi(-\pi) = \int_0^{\pi} \frac{d\psi}{r+\cos\psi} = \frac{1}{2}\pi\kappa$$

We need now to express the quantity $\sin\phi$ figuring in the integral as a function of ξ. Inverting Eq. (4.9) we obtain:

$$\tan\frac{\psi}{2} = \frac{1}{\omega}\tan\frac{\xi}{\kappa}$$

Then:

$$\sin\psi = \frac{2\tan\frac{\psi}{2}}{1+\tan^2\frac{\psi}{2}} = \frac{2\omega\tan\frac{\xi}{\kappa}}{\omega^2+\tan^2\frac{\xi}{\kappa}}$$

Replacing, the integral will become:

$$\Gamma_{s,12} = -2\int_{-\frac{1}{2}\pi\kappa}^{\frac{1}{2}\pi\kappa} d\xi'\, \frac{2\omega\xi'\tan\frac{\xi'}{\kappa}}{\omega^2+\tan^2\frac{\xi'}{\kappa}} = -4\omega\kappa^2\int_{-\frac{\pi}{2}}^{\frac{\pi}{2}} dy\, \frac{y\tan y}{\omega^2+\tan^2 y}$$

having called $y = \xi/\kappa \in [-\pi/2, \pi/2]$. The integrand can be simplified furtherly by considering:

$$\frac{\tan y}{\omega^2+\tan^2 y} = \frac{\sin y\cos y}{\sin^2 y + \omega^2\cos^2 y} = \frac{\sin y\cos y}{1+(\omega^2-1)\cos^2 y}$$

which taking:

$$\sin y \cos y = \frac{1}{2}\sin 2y \qquad\qquad \cos^2 y = \frac{1}{2}(1+\cos 2y)$$

allows us to write:

$$\Gamma_{s,12} = -4\omega\kappa^2 \int_{-\frac{\pi}{2}}^{\frac{\pi}{2}} dy\, \frac{y \sin 2y}{(\omega^2+1)+(\omega^2-1)\cos 2y} = -\omega\kappa^2 \int_{-\pi}^{\pi} dx\, \frac{x \sin x}{\alpha + \beta \cos x}$$

where we called $x = 2\pi \in [-\pi, \pi]$, $\alpha = \omega^2 + 1$ and $\beta = \omega^2 - 1$. The right hand side can be now easily integrated by parts:

$$\Gamma_{s,12} = -\frac{\omega\kappa^2}{\beta}\left[-x \log\left(1+\frac{\beta}{\alpha}\cos x\right)\right]_{-\pi}^{\pi} - \frac{\omega\kappa^2}{\beta}\int_{-\pi}^{\pi} dx\, \log\left(1+\frac{\beta}{\alpha}\cos x\right)$$

$$= \frac{2\pi\omega\kappa^2}{\beta}\log\left(1-\frac{\beta}{\alpha}\right) - \frac{2\pi\omega\kappa^2}{\beta}\log\left(\frac{1+\sqrt{1-\frac{\beta^2}{\alpha^2}}}{2}\right)$$

$$= \frac{2\pi\omega\kappa^2}{\beta}\log\left[\frac{2(1-\frac{\beta}{\alpha})}{1+\sqrt{1-\frac{\beta^2}{\alpha^2}}}\right]$$

which expressing all the parameters in term of the aspect ratio r gives finally:

$$\Gamma_{s,12} = -2\pi\kappa \log\left[\frac{2(r+1)}{r+\sqrt{r^2-1}}\right]$$

Combining $\Gamma_{s,11}$ and $\Gamma_{s,12}$ we obtain:

$$\Gamma_{s,1} = \frac{1}{2}\Gamma_{s,11} - \frac{1}{2p_1}\Gamma_{s,12} = \log\left[\frac{2(r^2-1)}{(r+\cos\psi)(r+\sqrt{r^2-1})}\right]$$

To complete the calculation of Γ_s we need now to calculate:

$$\Gamma_{s,2} = \int d^2y\, \langle G(\cdot\,, \boldsymbol{y})\rangle K(\boldsymbol{y}) \tag{4.90}$$

Rather then calculate the function $\langle G(\cdot\,, \boldsymbol{y})\rangle$ and integrate it, it is more convenient to invert the order of the two integrals and using the result we just obtained for the $\Gamma_{s,1}$. Explicitly:

$$A\,\Gamma_{s,2} = \int d^2x\, K(\boldsymbol{x}) \int d^2y\, G_0(\boldsymbol{x}, \boldsymbol{y})$$

$$= \int d^2y \int d^2x\, K(\boldsymbol{x})\, G_0(\boldsymbol{x}, \boldsymbol{y}) = \int d^2y\, \Gamma_{s,1}(\boldsymbol{y})$$

Now, calling:

$$f(r) = \frac{2(r^2-1)}{r+\sqrt{r^2-1}}$$

the $\Gamma_{s,2}$ integral becomes:

$$\begin{aligned} A\,\Gamma_{s,2} &= \log f(r) \int d^2y - \int d\psi'\, d\phi'\, \sqrt{g'}\, \log(r+\cos\phi') \\ &= A \log f(r) - 2\pi R_1 R_2 \int_{-\pi}^{\pi} d\psi'\, \log(r+\cos\phi') \\ &\quad -2\pi R_2^2 \int_{-\pi}^{\pi} d\psi'\, \cos\psi' \log(r+\cos\psi') \end{aligned}$$

The first integral is of the form:

$$\int_{-\pi}^{\pi} dx\, \log(1+a\cos x) = 2\pi \log\left(\frac{1+\sqrt{1-a^2}}{2}\right) \qquad |a|^2 < 1$$

and can thus immediately calculated by choosing $a = r^{-1}$:

$$\Gamma_{s,21} = \int_{-\pi}^{\pi} d\psi' \log(r+\cos\psi') = 2\pi \log\left(\frac{r+\sqrt{r^2-1}}{2}\right)$$

The second integral can be related to an integral of the form:

$$\int_0^{\pi} dx\, \cos nx\, \log(1-2a\cos x+a^2) = -\frac{\pi a^n}{n} \qquad |a|^2 < 1$$

by choosing $n = 1$ and $a = -r+\sqrt{r^2-1}$. Thus we have:

$$\Gamma_{s,22} = 2\pi\left(r-\sqrt{r^2-1}\right)$$

Combining $\Gamma_{s,21}$ and $\Gamma_{s,22}$ we find:

$$\begin{aligned} \Gamma_{s,2} &= \log f(r) - \frac{2\pi}{A}\left(R_1 R_2 \Gamma_{s,21} + R_2^2 \Gamma_{s,22}\right) \\ &= \log\left[\frac{4(r^2-1)}{(r+\sqrt{r^2-1})^2}\right] - \frac{r-\sqrt{r^2-1}}{r} \end{aligned}$$

Merging the two main contributions $\Gamma_{s,1}$ and $\Gamma_{s,2}$ we can finally write the screening function Γ_s in the form:

$$\Gamma_s(\psi) = \log\left[\frac{r+\sqrt{r^2-1}}{2(r+\cos\psi)}\right] + \frac{r-\sqrt{r^2-1}}{r} \tag{4.91}$$

Appendix 4.D The function $\langle G_0(\boldsymbol{x},\cdot)\rangle$

We proceed now to the calculation of the function $\langle G_0(\boldsymbol{x},\cdot)\rangle$ figuring in the expression of the elastic free energy.Again it is convenient to express the Green function G_0 in the form of a series rather than in the more compact form (4.88):

$$A\,\langle G_0(\boldsymbol{x},\cdot)\rangle = -\frac{1}{p_1 p_2}\sum_{(n,m)\neq(0,0)}\frac{1}{\lambda_n^2+\lambda_m^2}$$
$$\int_{-\pi}^{\pi} d\psi'\,\sqrt{g'}\,\cos\lambda_m(\xi-\xi')\int_{-\pi}^{\pi} d\phi'\,\cos\mu_m(\phi-\phi')$$

As in the previous section, the only non-zero contribution from the sum in m is given by $m=0$. Summing over n we have then:

$$A\,\langle G_0(\boldsymbol{x},\cdot)\rangle = -\frac{\pi}{6}R_1R_2+\frac{1}{2}\int_{-\pi}^{\pi} d\psi'\,\sqrt{g'}\,|\xi-\xi'| - \frac{1}{2p_1}\int_{-\pi}^{\pi} d\psi'\,\sqrt{g'}\,|\xi-\xi'|^2$$

The expanding the absolute value as in the previous section, we can write the first integral in the form:

$$I_1 = \int_{-\pi}^{\pi} d\psi'\,\sqrt{g'}\,|\xi-\xi'|$$
$$= \xi\int_{-\psi}^{\psi} d\psi'\,\sqrt{g'} + 2\int_{\psi}^{\pi} d\psi'\,\sqrt{g'}\,\xi'$$
$$= 2R_1R_2\psi\xi + 2R_2^2\xi\sin\psi + 2\int_{\psi}^{\pi} d\psi'\,\sqrt{g'}\,\xi' \tag{4.92}$$

The integral last integral can be simplified integrating by parts:

$$I_{11} = \int_{\psi}^{\pi} d\psi'\,\sqrt{g'}\,\xi'$$
$$= R_1R_2\int_{\psi}^{\pi} d\psi'\,\xi' + R_2^2\int_{\psi}^{\pi} d\psi'\,\cos\psi'\xi'$$
$$= R_2^2\log\left(\frac{r-1}{r+\cos\psi}\right) - R_2^2\xi\sin\psi + R_1R_2\int_{\psi}^{\pi} d\psi'\,\xi'$$

The last integral can be easily calculated by expanding the ξ function in Fourier harmonics. The conformal angle ξ is an odd function of ξ of period 2π, thus admit a

Fourier series in the canonical form:

$$\xi(\psi) = \sum_{n=1}^{\infty} b_n \sin(n\psi) \tag{4.93}$$

The Fourier coefficient b_n is given by:

$$\pi b_n = \int_{-\pi}^{\pi} d\psi\, \sin n\psi\, \xi(\psi) = -\left[\frac{\xi(\psi)}{n}\cos n\psi\right]_{-\pi}^{\pi} + \frac{1}{n}\int_{-\pi}^{\pi} d\psi\, \frac{\cos n\psi}{r+\cos\psi}$$

$$= -\frac{\kappa}{n}\cos n\pi + \frac{1}{n}\int_{-\pi}^{\pi} d\psi\, \frac{\cos n\psi}{r+\cos\psi}$$

The last integral can be reconducted to the form:

$$\int_0^{\psi} dx\, \frac{\cos nx}{1+a\cos x} = \frac{\pi}{\sqrt{1-a^2}}\left(\frac{\sqrt{1-a^2}-1}{a}\right)^n \qquad |a|^2 < 1$$

by taking $a = r^{-1}$. Then:

$$\int_{-\pi}^{\pi} d\psi\, \frac{\cos n\psi}{r+\cos\psi} = \frac{2}{\sqrt{r^2-1}}\left(\sqrt{r^2-1}-r\right)^n$$

having called $\alpha = \sqrt{r^2-1} - r$. The Fourier coefficient b_n is then given by:

$$b_n = \frac{\kappa}{n}\left(\alpha^n - \cos n\pi\right) = \frac{\kappa}{n}\left[\alpha^n - (-1)^n\right] \tag{4.94}$$

Integrating the Fourier harmonics term by term we have:

$$I_{12} = \int_{\psi}^{\pi} d\psi'\, \xi(\psi') = \sum_{n=1}^{\infty} b_n \int_{\psi}^{\pi} d\psi'\, \sin n\psi' = \sum_{n=1}^{\infty} \frac{b_n}{n}(\cos n\psi - \cos n\pi)$$

$$= \kappa\sum_{n=1}^{\infty}\frac{\alpha^n}{n^2}\cos n\psi - \kappa\sum_{n=1}^{\infty}\frac{(-1)^n}{n^2}\alpha^n - \kappa\sum_{n=1}^{\infty}\frac{(-1)^n}{n^2}\cos n\psi + \kappa\sum_{n=1}^{\infty}\frac{1}{n^2}$$

$$= \frac{1}{4}\kappa(\pi^2-\psi^2) - \kappa\,\mathrm{Li}_2(-\alpha) + \kappa\,\mathrm{Re}\{\mathrm{Li}_2(\alpha e^{i\psi})\}$$

where $\mathrm{Re}\{\,\cdot\,\}$ stands for the real part. For the last step, we used:

$$\sum_{n=1}^{\infty}\frac{(-1)^n}{n^2}\cos nx = \sum_{n=1}^{\infty}\frac{\cos n\pi\cos nx}{n^2}$$

$$= \frac{1}{2}\sum_{n=1}^{\infty}\frac{\cos n|\pi+x|}{n^2} + \frac{1}{2}\sum_{n=1}^{\infty}\frac{\cos n|\pi-x|}{n^2} = \frac{1}{4}x^2 - \frac{1}{12}\pi^2$$

together with the notorious Euler identity:

$$\zeta(2)=\sum_{n=1}^{\infty}\frac{1}{n^2}=\frac{\pi^2}{6}$$

and the definition of dilogarithm:

$$\mathrm{Li}_2(z)=\sum_{n=1}^{\infty}\frac{z^n}{n^2}$$

Replacing I_{11} and I_{12} in (4.92) we can write:

$$I_1=2R_1R_2\psi\xi+2R_2^2\log\left(\frac{r-1}{r+\cos\psi}\right)+\frac{1}{2}\kappa R_1R_2(\pi^2-\psi^2)$$
$$-2\kappa R_1R_2\,\mathrm{Li}_2(-\alpha)+2\kappa R_1R_2\,\mathrm{Re}\{\mathrm{Li}_2(\alpha e^{i\psi})\}\quad(4.95)$$

To accomplish the calculation of the $\langle G_0(\cdot\,,\boldsymbol{x})\rangle$ we are left with the integral:

$$I_2=\int_{-\pi}^{\pi}d\psi'\,\sqrt{g'}\,|\xi-\xi'|^2$$
$$=R_1R_2\int_{-\pi}^{\pi}d\psi'\,|\xi-\xi'|^2+R_2^2\int_{-\pi}^{\pi}d\psi'\,\cos\psi'\,|\xi-\xi'|^2$$

The second integral in I_2 has already been calculated in the previous section and is:

$$I_{22}=\Gamma_{s,12}=-2\pi\kappa\log\left[\frac{2(r^2+1)}{r+\sqrt{r^2-1}}\right]$$

To calculate the first integral we can write:

$$I_{21}=\int_{-\pi}^{\pi}d\psi'\,|\xi-\xi'|^2=2\pi\xi^2+\int_{-\pi}^{\pi}d\psi'\,\xi'^2$$

To calculate the integral of ξ^2 we can recall that, letting $f(x)$ being a square-integrable function with Fourier series:

$$f(x)=\frac{a_0}{2}+\sum_{n=1}^{\infty}(a_n\cos nx+b_n\sin nx)$$

the Parseval's identity requires:

$$\frac{1}{\pi}\int_{-\pi}^{\pi}dx\,f^2(x)=\frac{a_0^2}{2}+\sum_{n=1}^{\infty}(a_n^2+b_n^2)$$

which in our case reads:

$$\int_{-\pi}^{\pi} d\psi'\, \xi'^2 = \pi \sum_{n=1}^{\infty} b_n^2 = \pi\kappa^2 \left[\sum_{n=1}^{\infty} \frac{\alpha^{2n}}{n^2} + \sum_{n=1}^{\infty} \frac{1}{n^2} - 2\sum_{n=1}^{\infty} \frac{(-1)^n}{n^2}\, \alpha^n \right]$$
$$= \pi\kappa^2 \left[\mathrm{Li}_2(\alpha^2) + \frac{\pi^2}{6} - 2\,\mathrm{Li}_2(-\alpha) \right] = \pi\kappa^2 \left[2\,\mathrm{Li}_2(\alpha^2) + \frac{\pi^2}{6} \right]$$

where for the last step we used the Euler dilogarithmic ladder:

$$\mathrm{Li}_2(z) + \mathrm{Li}_2(-z) = \frac{1}{2}\, \mathrm{Li}_2(z^2) \tag{4.96}$$

Recombining the integrals I_1 and I_2 and we obtain finally:

$$\langle G_0(\boldsymbol{x}, \cdot\,) \rangle = -\frac{\kappa}{16\pi^2} \left(\psi - \frac{2}{\kappa}\, \xi \right)^2 - \frac{\kappa}{8\pi^2}\, \mathrm{Li}_2(\alpha^2)$$
$$+ \frac{\kappa}{4\pi^2}\, \mathrm{Re}\{\mathrm{Li}_2(\alpha e^{i\psi})\} + \frac{1}{4\pi^2 r}\, \log \left[\frac{2(r^2-1)}{(r+\cos\psi)(r+\sqrt{r^2-1})} \right] \tag{4.97}$$

Appendix 4.E The stress function $\Gamma(\boldsymbol{x})$

We are finally ready to combine the results of the previous two sections and write the complete expression of the energy density Γ. Using (4.88), (4.97) in (4.47) we have:

$$\frac{\Gamma(\boldsymbol{x})}{Y} = \frac{\pi}{3} \sum_{k=1}^{N} q_k \Gamma_d(\boldsymbol{x}, \boldsymbol{x}_k) - \Gamma_s(\boldsymbol{x}) \tag{4.98}$$

Calling $z = \xi + i\phi$ the defects contribution Γ_d to the energy is given by:

$$\Gamma_d(\boldsymbol{x}, \boldsymbol{x}_k) = \frac{\kappa}{16\pi^2} \left(\psi_k - \frac{2}{\kappa}\, \xi_k \right)^2 - \frac{1}{4\pi^2\kappa}\, (\phi - \phi_k)^2$$
$$+ \frac{1}{4\pi^2 r}\, \log\left(r + \cos\psi_k\right) - \frac{\kappa}{4\pi^2}\, \mathrm{Re}\{\mathrm{Li}_2(\alpha e^{i\psi_k})\}$$
$$+ \frac{1}{2\pi} \log \left| \vartheta_1 \left(\frac{z - z_k}{\kappa} \middle| \frac{2i}{\kappa} \right) \right| \tag{4.99}$$

where all the constants figuring in (4.97) and (4.88) are canceled in virtue of the charge neutrality condition.

Chapter 5

Conclusion and discussion

In this article we reviewed some of the most recent progresses toward understanding the ground state properties of two-dimensional ordered phases on substrate of non-zero Gaussian curvature. The latter represents a broad class of systems comprising materials as different as viral capsids and carbon nanotori. The geometry of the substrate give arise to novel defective structures that would be energetically prohibitive in the ground state of conventional flat systems. Defects might appear in curved space either because required by the topology of the underlying substrate (as in the case of spherical crystals and nematics) or because favored by the curvature itself. The latter has indeed the property of coupling with the topological charge of the defects leading to an overall reduction of the elastic stress.

On the material science side, non-Euclidean systems provides a promising route to constructing arrays of nanoparticles is via the chemical functionalization of topological defects created on the surface of the particles by coating them with an ordered monolayer. Candidates for such coatings include triblock coplymers, gemini lipids, metallic or semiconducting nanorods and conventional liquid crystal compounds. If the induced order is vector-like or striped then there must necessarily be two defective regions corresponding to the bald spots exhibited by a combed sphere or the source and sink of fluid flow confined to a sphere. Not only are the defects physically

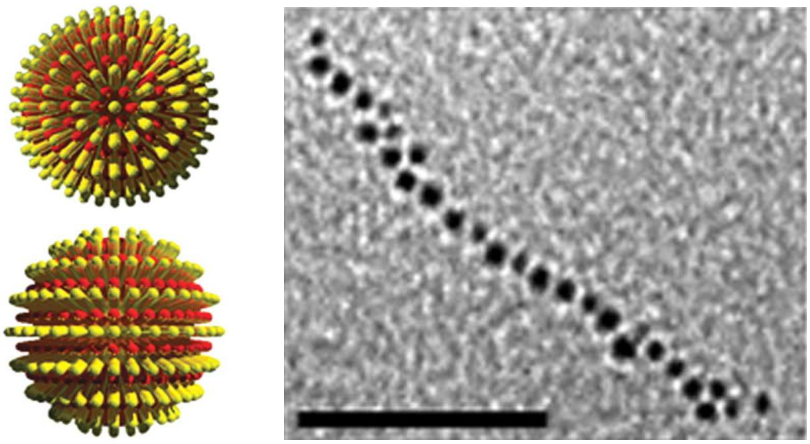

Figure 5.1: (Color online) (Left) Idealized drawing of a side and top view and of a rippled gold nanoparticle showing the two polar defects that must exist to allow the alternation of concentric rings. (Right) TEM images of a chain obtained when 11-mercaptoundecanoic acid functionalized nanoparticles are reacted with a water phase containing divalent 1,6-diaminohexane in a two-phase reaction. Scale bar 50 nm. From [174].

and mathematically distinguished, since the condensed matter order vanishes there, but it also turns out that chemical processes can detect the defects and insert linker molecules at the precise defect locations. This creates the possibility of efficiently making functionalized nanoparticles with a precise valence and corresponding directional bonding. The nanoparticles themselves can then be linked into well-defined two and three dimensional arrays. Control over the valence and the geometry of the directional bonding can be achieved by varying the nature of the ordered monolayer.

This scheme has been demonstrated recently in the work of DeVries *et al.* [174] in which gold nanoparticles are coated with two species of naturally phase separating ligands (see Fig. 5.1). Phase separation on the spherical gold surface translates to a striped arrangement of alternating ligands. Such a spherical smectic has topological defects at the north and south pole of the nanopartcle. These may be functionalized by attaching thiol-based linker molecules at the defects via place-exchange reactions. This creates a divalent gold nanoparticle with directional bonds 180 degrees apart. These in turn can be linked to create polymers and free-standing films.

Bibliography

[1] J. D'Alembert, *Essai d'une nouvelle théorie de la résistance des fluides* (1752).

[2] J. D. Bernal, Nature **185**, 68 (1960).

[3] J. D. Bernal, Proc. R. Soc. A **280**, 299 (1964).

[4] J. D. Bernal and J. L. Finney, Discuss. Faraday Soc. **43**, 62 (1967).

[5] J. L. Finney and J. D. Bernal, Nature **213**, 1079 (1967).

[6] J. L. Finney, Proc. R. Soc. A **319**, 479 (1970).

[7] S. Torquato, T. M. Truskett, and P. G. Debenedetti, Phys. Rev. Lett. **84**, 2064 (2000).

[8] D. Shechtman, I. Blech, D. Gratias, and J. W. Cahn, Phys. Rev. Lett. **53**, 1951 (1984).

[9] D. Levine and P. J. Steinhardt, Phys. Rev. Lett. **53**, 2477 (1984).

[10] J. Farges, M. F. de Féraudy, B. Raoult, and G. Torchet, J. Phys. (Paris) **36**, C2 (1975).

[11] J. Farges, M. F. de Féraudy, B. Raoult, and G. Torchet, J. Phys. (Paris) **38**, C2 (1977).

[12] J. Farges, M. F. de Féraudy, B. Raoult, and G. Torchet, Surf. Sci. **106**, 95 (1981).

[13] M. Kléman and J. F. Sadoc, J. Phys. Lett. (Paris) **40**, 569 (1979).

[14] J. F. Sadoc and R. Mosseri, Philos. Mag. B **45**, 467 (1982).

[15] P. J. Steinhardt, D. R. Nelson, and M. Ronchetti, Phys. Rev. Lett. **47**, 1297 (1981).

[16] D. R. Nelson, Phys. Rev. Lett. **50**, 982 (1983).

[17] M. Kléman, Adv. Phys. **38**, 605 (1989).

[18] D. R. Nelson, T. Piran, and S. Weinberg, eds., *Statistical Mechanics of Membranes and Surfaces* (World Scientific, Singapore, 2004), 2nd ed.

[19] D. R. Nelson and L. Peliti, J. Phys. France **48**, 1085 (1987).

[20] V. Berezinskii, Zh. Eksp. Teor. Fiz. **59**, 907 (1970), [Sov. Phys., JETP 32 (1971), p. 493].

[21] J. M. Kosterlitz and D. J. Thouless, J. Phys. C **5**, L124 (1972).

[22] J. M. Kosterlitz and D. J. Thouless, J. Phys. C **6**, 1181 (1973).

[23] J. M. Kosterlitz, J. Phys. C **7**, 1046 (1974).

[24] G. S. Smith, E. B. Sirota, C. R. Safinya, and N. A. Clark, Phys. Rev. Lett. **60**, 813 (1988).

[25] J. Meunier, D. Langevin, and N. Boccara, *Physics of amphiphilic layers* (Springer, Berlin, 1987).

[26] A. D. Dinsmore, M. F. Hsu, M. G. Nikolaides, M. Marquez, A. R. Bausch, and D. A. Weitz, Science **298**, 1006 (2002).

[27] O. D. Velev, K. Furusawa, and K. Nagayama, Langmuir **12**, 2374 (1996).

[28] O. D. Velev, K. Furusawa, and K. Nagayama, Langmuir **12**, 2385 (1996).

[29] O. D. Velev and K. Nagayama, Langmuir **13**, 1856 (1997).

[30] G. R. Yi, V. N. Manoharan, S. Klein, K. R. Brzezinska, D. J. Pine, F. F. Lange, and S. M. Yang, Adv. Mater. **14**, 1137 (2002).

[31] D. Y. Wang and F. Caruso, Chem. Mater. **14**, 1909 (2002).

[32] G. Kumaraswamy, A. M. Dibaj, and F. Caruso, Langmuir **18**, 4150 (2002).

[33] M. Fang, P. Grant, M. McShane, G. Sukhorukov, V. Golub, and Y. Lvov, Langmuir **18**, 6338 (2002).

[34] A. Loxley and B. Vincent, J. Colloid Interface Sci. **208**, 49 (1998).

[35] P. Pieranski, Phys. Rev. Lett. **45**, 569 (1980).

[36] W. Irvine and P. M. Chaikin, In preparation (2009).

[37] M. E. Leunissen, A. van Blaaderen, A. D. Hollingsworth, M. T. Sullivan, and P. M. Chaikin, Proc. Natl. Acad. Sci. USA **104**, 2582 (2007).

[38] D. L. D. Caspar and A. Klug, Cold Spring Harbor Symp. Quant. Bio. **27**, 1 (1962).

[39] J. Lindmar, L. Minry, and D. R. Nelson, Phys. Rev. E **68**, 051910 (2003).

[40] N. A. Kiselev and A. Klug, J. Mol. Biol. **40**, 155 (1969).

[41] X. F. Dong, P. Natarajan, M. Tihova, J. E. Johnson, and A. Schneemann, J. Virol. **72**, 6024 (1998).

[42] D. M. Salunke, D. L. D. Caspar, and R. L. Garcea, Biophys. J. **56**, 887 (1989).

[43] J. B. Bancroft, Adv. Virus Res. **16**, 99 (1970).

[44] T. T. Nguyen, R. F. Bruinsma, and W. M. Gelbart, Phys. Rev. E **72**, 051923 (2005).

[45] M. Carrillo-Tripp, C. M. Shepherd, I. A. Borelli, S. Venkataraman, G. Lander, P. Natarajan, J. E. Johnson, C. L. B. III, and V. S. Reddy, *Viperdb2: an enhanced and web api enabled relational database for structural virology* (2008), URL `http://viperdb.scripps.edu/`.

[46] S. Iijima, Nature **354**, 56 (1991).

[47] S. Amelinckx, X. B. Zhang, D. Bernaerts, X. Zhang, V. Ivanov, and J. Nagy, Science **265**, 635 (1994).

[48] J. Liu, H. Dai, J. H. Hafner, D. T. Colbert, R. E. Smalley, S. J. Tans, and C. Dekker, Nature **385**, 780 (1997).

[49] A. Krishnan, E. Dujardin, M. M. J. Treacy, J. Hugdahl, S. Lynum, and T. Ebbesen, Nature **388**, 451 (1997).

[50] J. Du, Z. Liu, Z. Li, B. Han, Z. Sun, and Y. Huang, Materials Lett. **59**, 456 (2005).

[51] R. Saito, G. Dresselhaus, and M. S. Dresselhaus, *Physical properties of carbon nanotubes* (Imperial College Press, London, 1998).

[52] A. J. Stone and D. J. Wales, Chem. Phys. Lett. **128**, 501 (1986).

[53] M. B. Nardelli, B. I. Yakobson, and J. Bernholc, Phys. Rev. B **57**, R4277 (1998).

[54] N. Mingo, D. A. Stewart, D. A. Broido, and D. Srivasta, Phys. Rev. B **77**, 033418 (2008).

[55] F. OuYang, B. Huang, Z. Li, J. Xiao, H. Wang, and H. Xu, J. Phys. Chem. C **112**, 12003 (2008).

[56] J. F. Sadoc and R. Mosseri, *Geometrical Frustration* (Cambridge Univ. Press, Cambridge, 1999).

[57] G. Toulouse, Commun. Phys. **2**, 115 (1977).

[58] T. C. Lubensky and J. Prost, J. Phys. II France **2**, 371 (1992).

[59] V. Vitelli and D. R. Nelson, Phys. Rev. E **74**, 021711 (2006).

[60] D. R. Nelson and R. A. Pelcovits, Phys. Rev. B **16**, 2191 (1977).

[61] M. W. Deem, Phys. Rev. E **54**, 6441 (1996).

[62] P. M. Chaikin and T. C. Lubensky, *Principle of Condensed Matter Physics* (Cambridge Univ. Press, Cambridge, 1995).

[63] A. M. Turner, V. Vitelli, and D. R. Nelson (2008), `arXiv:0807.0413`.

[64] F. R. N. Nabarro, *Theory of Crystal Dislocations* (Oxford University Press, Oxford, 1967).

[65] J. P. Hirth and J. Lothe, *Theory of Dislocations* (McGraw-Hill, New York, 1968).

[66] D. R. Nelson and B. I. Halperin, Phys. Rev. B **19**, 2457 (1979).

[67] A. E. Green and W. Zerna, *Theoretical Elasticity* (Oxford University Press, Oxford, 1954).

[68] H. S. Seung and D. R. Nelson, Phys. Rev. A **38**, 1005 (1988).

[69] J. Lidmar, L. Mirny, and D. R. Nelson, Phys. Rev. E **68**, 051910 (2003), `cond-mat/0306741`.

[70] M. J. W. Dodgson, J. Phys. A **29**, 2499 (1996).

[71] M. J. W. Dodgson and M. A. Moore, Phys. Rev. B **55**, 3816 (1997).

[72] M. J. Bowick, D. R. Nelson, and A. Travesset, Phys. Rev. B **62**, 8738 (2000), `cond-mat/9911379`.

[73] M. J. Bowick and A. Travesset, J. Phys. A **34**, 1535 (2001), `cond-mat/0005356`.

[74] F. C. MacKinotsh and T. C. Lubensky, Phys. Rev. Lett. **67**, 1169 (1991).

[75] D. R. Nelson, Nano Lett. **2**, 1125 (2002).

[76] A. Fernandez-Nieves, D. Link, D. Rudhardt, and D. Weitz, Phys. Rev. Lett. **92**, 105503 (2004).

[77] A. Fernandez-Nieves, V. Vitelli, A. S. Utada, D. R. Link, M. Marquez, D. R. Nelson, and D. A. Weitz, Phys. Rev. Lett. **99**, 157801 (2007).

[78] J. J. Thomson, Philos. Mag. **7**, 237 (1904).

[79] E. B. Saff and A. B. J. Kuijlaars, Math. Intelligencer **19**, 5 (1997).

[80] D. P. Hardin and E. B. Saff, Notices of the Am. Math. Soc. **51**, 1186 (2005).

[81] U. Albrecht and P. Leiderer, J. Low Temp. Phys. **86**, 131 (1992).

[82] P. Leiderer, Z. Phys. B **98**, 303 (1995).

[83] C. Grimes and G. Adams, Phys. Rev. Lett. **42**, 795 (1979).

[84] D. C. Glattli, E. Y. Andrei, and F. I. B. Williams, Phys. Rev. Lett. **60**, 420 (1998).

[85] P. Lenz and D. R. Nelson, Phys. Rev. Lett. **87**, 125703 (2001).

[86] P. Lenz and D. R. Nelson, Phys. Rev. E **67**, 031502 (2003).

[87] E. J. Davis, Aerosol Sci. Techn. **26**, 212 (1997).

[88] E. L. Altschuler, T. J. Williams, E. R. Ratner, F. Dowla, and F. Wooten, Phys. Rev. Lett. **72**, 2671 (1994).

[89] E. L. Altschuler, T. J. Williams, E. R. Ratner, R. Tipton, R. Stong, F. Dowla, and F. Woote, Phys. Rev. Lett. **78**, 2681 (1997).

[90] T. Erber and M. G. Hockney, Phys. Rev. Lett. **74**, 1482 (1995).

[91] J. R. Morris, D. M. Deaven, and K. M. Ho, Phys. Rev. B **54**, R1740 (1996).

[92] E. L. Altschuler and A. P. Garrido, Phys. Rev. E **71**, 047703 (2005).

[93] A. Siber (2007), `arXiv:0711.3527`.

[94] M. J. Bowick, A. Cacciuto, D. R. Nelson, and A. Travesset, Phys. Rev. Lett. **89**, 185502 (2002), `cond-mat/0206144`.

[95] A. R. Bausch, M. J. Bowick, A. Cacciuto, A. D. Dinsmore, M. F. Hsu, D. R. Nelson, M. G. Nikolaides, A. Travesset, and D. A. Weitz, Science **299**, 1716 (2003), `cond-mat/0303289`.

[96] P. Lipowsky, M. J. Bowick, J. H. Meinke, D. R. Nelson, and A. B. Bausch, Nature Materials **4**, 407 (2005).

[97] M. J. Bowick, A. Cacciuto, D. R. Nelson, and A. Travesset, Phys. Rev. B **73**, 024115 (2006), `cond-mat/0509777`.

[98] M. J. Bowick and L. Giomi, Adv. Phys. (in press) (2009), `arXiv:0812.3064`.

[99] V. A. Raghunathan and J. Katsaras, Phys. Rev. E **54**, 4446 (1996).

[100] M. J. Bowick, L. Giomi, C. K. Thomas, and H. Shin, Phys. Rev. E **77**, 021602 (2008).

[101] E. Kreyszig, *Differential Geometry* (University of Toronto Press, Toronto, 1959).

[102] S. Shimorin, J. Math. Sci. **92**, 4404 (1998).

[103] V. Vitelli, J. B. Lucks, and D. R. Nelson, Proc. Natl. Acad. Sci. USA **103**, 12323 (2006).

[104] V. Vitelli and D. R. Nelson, Phys. Rev. E **70**, 051105 (2004).

[105] A. Hexemer, V. Vitelli, E. J. Kramer, and G. H. Fredrickson, Phys. Rev. E **76**, 051604 (2007).

[106] L. Giomi and M. J. Bowick, Phys. Rev. B **76**, 054106 (2007).

[107] L. Giomi and M. J. Bowick, Chaos **17**, 041104 (2007).

[108] M. D. Carmo, *Differential geometry of curves and surfaces* (Prentice-Hall, 1976).

[109] D. J. Wales and S. Ulker, Phys. Rev. B **74**, 212101 (2006).

[110] R. Storn and K. Price, J. Glob. Opt. **11**, 341 (1997).

[111] T. Einert, P. Lipowsky, J. Schilling, M. J. Bowick, and A. Bausch, Langmuir **21**, 12076 (2005), `cond-mat/0506741`.

[112] L. Bragg and J. F. Nye, 1947 **A190**, 474 (Proc. Roy. Soc.).

[113] R. P. Feynamn, R. B. Leighton, and M. Sands, *Feynman Lectures on Physics*, vol. 2 (Addison-Wesley, Reading, MA, 1963).

[114] A. W. Simpson and P. H. Hodkinson, Nature **237**, 320 (1972).

[115] A. Gouldstone, K. J. V. Vliet, and S. Suresh, Nature **411**, 656 (2001).

[116] Y. Wang, K. Krishan, and M. Denin, Phys. Rev. E **73**, 031401 (2006).

[117] M. P. Spiegel, *Applied Differential Equations* (Prentice-Hall, Englewood Cliffs, NJ, 1958).

[118] J. C. Crocker and D. G. Grier, J. Colloid Interface Sci. **179**, 298 (1996).

[119] D. R. Nelson, *Defects and Geometry in Condensed Matter Physics* (Cambridge Univ. Press, Cambridge, 2000).

[120] G. C. Onwubolu and B. Babu, *New Optimization Techniques in Engineering (Studies in Fuzziness and Soft Computing)* (Springer, 2004).

[121] M. Mutz and D. Bensimon, Phys. Rev. A **43**, 4525 (1991).

[122] L. Zhang and A. Eisenberg, Science **268**, 1728 (1995).

[123] K. Yu, L. Zhang, and A. Eisenberg, Langmuir **12**, 5980 (1996).

[124] S. Burke and A. Eisenberg, High Perform. Polym. **12**, 535 (2000).

[125] S. Jain and F. S. Bates, Science **300**, 460 (2003).

[126] D. J. Pochan, Z. Y. Chen, H. G. Cui, K. Hales, K. Qi, and K. L. Wooley, Science **306**, 94 (2004).

[127] J. K. Kim, E. Lee, Z. Huang, and M. Lee, J. Am. Chem. Soc. **128**, 14022 (2006).

[128] X. He and F. Schmid, Phys. Rev. Lett. **100**, 137802 (2008).

[129] R. M. L. Evans, J. Phys. II France **5**, 507 (1995).

[130] M. J. Bowick, D. R. Nelson, and A. Travesset, Phys. Rev. E **69**, 041102 (2004).

[131] L. Giomi and M. J. Bowick, Phys. Rev. E **78**, 010601(R) (2008).

[132] L. Giomi and M. J. Bowick, Eur. Phys. J. E **27**, 275 (2008).

[133] U. Seifert, Phys. Rev. Lett. **66**, 2404 (1991).

[134] D. Mumford, *Tata Lectures on Theta I* (Birkhauser, Boston, MA, 1983).

[135] J. Polchinski, *String Theory* (Cambridge University Press, Cambridge, 1998).

[136] W. Helfrich, Z. Naturforsch. **28c**, 693 (1973).

[137] J. Park, T. C. Lubensky, and F. C. MacKinotsh, Europhys. Lett. **20**, 279 (1992).

[138] R. M. L. Evans, Phys. Rev. E **53**, 935 (1996).

[139] E. J. Snijder and M. C. Horzinek, *The Coronaviridae* (Plenum Press, New York, 1995), chap. 11, p. 219.

[140] V. Meunier, P. Lambin, and A. A. Lucas, Phys. Rev. B **57**, 14886 (1998).

[141] C. P. Liu, H. B. Chen, and J. W. Ding, J. Phys.: Condens. Matter **20**, 015206 (2008).

[142] M. Sano, A. Kamino, J. Okamura, and S. Shinkai, Science **293**, 1299 (2001).

[143] S. A. Lavrenchenko, J. Math. Sci **51**, 2537 (1990).

[144] B. I. Dunlap, Phys. Rev. B **46**, 1933 (1992).

[145] S. Itoh, S. Ihara, and J. Kitakami, Phys. Rev. B **47**, 1703 (1993).

[146] E. C. Kirby, Fullerene Sci. Tech. **2**, 395 (1994).

[147] I. László and A. Rassat, Int. J. Quantum Chem. **84**, 136 (2001).

[148] M. V. Diudea, A. Graovac, and A. Kerber, Commun. Math. Comput. Chem. **93**, 102 (2001).

[149] B. I. Dunlap, Phys. Rev. B **49**, 5643 (1994).

[150] B. I. Dunlap, Phys. Rev. B **50**, 8134 (1994).

[151] S. Itoh, S. Ihara, and J. Kitakami, Phys. Rev. B **47**, 12908 (1993).

[152] S. Itoh and S. Ihara, Phys. Rev. B **48**, 8323 (1993).

[153] I. László, A. Rassat, P. W. Fowler, and A. Graovac, Chem. Phys. Lett. **342**, 369 (2001).

[154] W. T. Webber, Geometriae Dedicata **67**, 31 (1997).

[155] P. Lambin, A. Fonseca, J. P. Vigneron, J. B. Nagy, and A. A. Lucas, Chem. Phys. Lett. **245**, 85 (1995).

[156] J. Berger and J. E. Avron, Phys. Rev. A **51**, 1146 (1995).

[157] J. Berger and J. E. Avron, J. Chem. Soc. Faraday. Trans. **91**, 4037 (1995).

[158] M. Goldberg, Tohoku Math. J. **43**, 104 (1937).

[159] H. S. M. Coxeter, *A Spectrum of Mathematics (essay presented to H. G. Forder)* (Aukland University Press, Aukland, 1971), p. 98.

[160] I. László and A. Rassat, J. Chem. Inf. Comput. Sci. **43**, 519 (2003).

[161] M. V. Diudea, Phys. Chem. Chem. Phys. **4**, 4740 (2002).

[162] M. Kleman and O. D. Lavrentovich, *Soft Matter Physics, an Introduction* (Springer, New York, NY, 2003).

[163] J. Han, Tech. Rep., NAS (1997).

[164] J. Han, Chem. Phys. Lett. **282**, 187 (1998).

[165] L. Giomi and D. Giuliani, *Toroidal lattices database*, http://physics.syr.edu/∼lgiomi/torus/database/.

[166] F. C. Frank, Proc. R. Soc. London Ser. A **215**, 43 (1952).

[167] J. Kierfeld and V. Vinokur, Phys. Rev. B **61**, R14928 (2000).

[168] M. Abramowitz and I. A. Stegun, *Handbook of Mathematical Functions with Formulas, Graphs, and Mathematical Tables* (Dover, New York, NY, 1964), URL `http://www.math.sfu.ca/∼cbm/aands/`.

[169] L. Burakovsky, D. L. Preston, and R. S. Silbar, Phys. Rev. B **61**, 15011 (2000).

[170] D. J. Wales and J. P. K. Doye, J. Phys. Chem. A **101**, 5111 (1997).

[171] S. Goedecker, J. Chem. Phys. **120**, 9911 (2004).

[172] W. H. Press, S. A. Teukolsky, W. T. Vetterling, and B. P. Flannery, *Numerical Recipes in C* (Cambridge University Press, Cambridge, 1992), 2nd ed.

[173] R. A. Dwyer, Algorithmica **2**, 137 (1987).

[174] G. A. DeVries, M. Brunnbauer, Y. Hu, A. M. Jackson, B. Long, B. T. Neltner, O. Uzun, B. H. Wunsch, and F. Stellacci, Science **315**, 358 (2007).